



Programa de Doctorado en Clima, Energía y Riesgo Ambiental

**Detection, classification and postclassification of urban
features from multispectral images and mobile LIDAR
point clouds**

TESIS DOCTORAL

para la obtención del grado de doctor

Autor

Borja Rodríguez Cuenca

Dirigida por

Dra. María Concepción Alonso Rodríguez

Dr. Silverio García Cortés

Alcalá de Henares, 2016

TESIS DOCTORAL

Programa de Doctorado en Clima, Energía y Riesgo Ambiental

Departamento de Física y Matemáticas

Universidad de Alcalá

Título:

Detection, classification and postclassification of urban features from multispectral images and mobile LIDAR point clouds

Autor:

Borja Rodríguez Cuenca

Dirigida por

Dra. María Concepción Alonso Rodríguez

Dr. Silverio García Cortés

Alcalá de Henares, 2016

A José Antonio Malpica Velasco

Table of contents

Abstract.....	I
Resumen	III
List of Terms and Acronyms.....	VII
<i>CHAPTER 1 Introduction</i>	<i>1</i>
<i>1.1. Motivation.....</i>	<i>2</i>
<i>1.2. Research Objectives.....</i>	<i>3</i>
<i>1.3. Thesis Structure.....</i>	<i>5</i>
<i>1.4. Introduction to Remote Sensing Data, Remote Sensing Products and Pattern Recognition Techniques.....</i>	<i>6</i>
<i>1.4.1. Cartographic Science.....</i>	<i>6</i>
<i>1.4.2 Remote Sensing</i>	<i>8</i>
<i>1.4.3 Remote Sensing Data</i>	<i>8</i>
<i>1.4.3.1 Digital Image Data</i>	<i>9</i>
<i>1.4.3.2. Laser Scanner Sensors</i>	<i>12</i>
<i>1.4.4. Remote Sensing Products</i>	<i>16</i>
<i>1.4.4.1. Digital Elevation Models.....</i>	<i>16</i>
<i>1.4.4.2. Orthoimages.....</i>	<i>17</i>
<i>1.4.4.3. Geographic Information Systems.....</i>	<i>18</i>
<i>1.4.5. Big Data problem: automation of geospatial data treatment and analysis</i>	<i>19</i>

1.4.6. Pattern Recognition Techniques.....	20
1.4.6.1. Supervised Classification	22
1.4.6.2. Unsupervised Classification	22
1.4.6.3. Fuzzy Logic.....	23
1.4.6.4. Anomaly and Target Detection	24
 CHAPTER 2 Land Use Land Cover (LULC) database updating: automatic land covers	
detection and classification.....	27
2.1. Land Use Land Cover Databases	28
2.1.1. Corine Land Cover	29
2.1.2. SIOSE.....	30
2.2. Paper N°1: Semi-automatic detection of swimming pools from aerial high- resolution images and LIDAR data.....	31
2.2.1. Summary	31
2.2.2. Quality Indicators.....	32
 CHAPTER 3 Urban furniture inventory: urban features extraction and classification	
from geospatial data.....	55
3.1. Paper N°2: Automatic detection and classification of pole-like objects in urban point cloud data using an anomaly detection algorithm.....	56
3.1.1. Summary	56
3.1.2. Quality Indicators.....	57
3.2. Paper N°3: An approach to detect and delineate street curbs from MLS 3D point cloud data.....	83
3.2.1. Summary	83
3.2.2. Quality Indicators.....	83

<i>CHAPTER 4 Post-classification processes</i>	95
4.1. <i>Paper N°4: A spatial contextual post-classification method for preserving linear objects in multispectral imagery</i>	96
4.1.1. <i>Summary</i>	96
4.1.2. <i>Quality Indicators</i>	97
<i>CHAPTER 5 Conclusions and future work</i>	109
Bibliography	121
Acknowledgments.....	129
Personal acknowledgments	131
Curriculum.....	135

Abstract

The scientific and technological development that happened in the second half of the twentieth century led to new tools, techniques, and technologies that forced many scientific disciplines to renovate, introducing and adapting these advances to the classical techniques to meet the new needs of society. The development of optics and sensors capable of taking information from various regions of the electromagnetic spectrum, the launching of satellites, and advances such as laser systems are contributions that have gradually been included in remote sensing works. Recent times have highlighted the importance of pattern recognition techniques in classification procedures and information extraction tasks in engineering, computer science, or mathematics issues. To certain sciences, such as remote sensing, these techniques are particularly important because they allow automatic cartographic entities detection and classification processes. Carrying out these procedures manually would be too expensive and time-consuming because of the high volume of remotely sensed information currently available.

The research works presented in this thesis are the result of the integration of data recorded by remote sensing measurement sensors and pattern recognition techniques. The final goal of the current research is to develop automatic and

semi-automatic methodologies to accomplish the cartographic entities extraction processes. These studies are of greatly complexity due to the varied casuistry of cartographic entities and heterogeneity of the input data. It is a challenge to develop functional, robust, and automatic algorithms. It seems logical that proper geographic features detection will be useful for urban planning, regional planning and decision-making in geography. This thesis aims to make contributions to the automatic creation and updating of databases land covers and street furniture inventories. Among the major contributions of this work are included the development of a series of methodologies capable of detecting entities such as artificial water surfaces, roadsides, trees, and street furniture from multispectral aerial images and LIDAR, both aerial and mobile.

These contributions have resulted in the publication of four articles in scientific impact journals. This thesis, presented in an article compendium format, includes the four published articles. Each paper describes the investigations carried out and includes a state of the subject's current art, an explanation of the implementation and operation of the developed algorithms, an evaluation and discussion about the achieved results, and an analysis of the reached conclusions.

Keywords: remote sensing, pattern recognition, LIDAR, aerial/satellite images, land cover database, urban furniture inventory

Resumen

El desarrollo científico y tecnológico acontecido en la segunda mitad del siglo XX dio lugar a nuevas herramientas, técnicas y tecnologías que obligaron a muchas disciplinas científicas a renovarse, introduciendo y adaptando estos avances a las técnicas clásicas con el objeto de satisfacer las nuevas necesidades de la sociedad. El desarrollo de ópticas y sensores capaces de tomar información en varias regiones del espectro electromagnético, la puesta en órbita de satélites o avances como los sistemas de medida láser han sido algunas de las aportaciones que paulatinamente se han ido incluyendo en los trabajos de teledetección. En los últimos tiempos se ha puesto de manifiesto la importancia de las técnicas de reconocimiento de patrones en labores de extracción y clasificación de información en procesos de ingeniería, ciencias de la computación o matemáticas. En algunas ciencias como la teledetección estas técnicas son de especial importancia ya que permiten automatizar procesos de detección y clasificación de entidades cartográficas que, de realizarse manualmente, tendrían un coste inasumible en términos económicos y temporales dado el elevado volumen de información geoespacial actualmente disponible.

Los trabajos de investigación que se presentan en esta tesis son el fruto de la

integración de datos registrados por sensores remotos y técnicas de reconocimiento de patrones. El objetivo último es el desarrollo de metodologías lo más automáticas o semiautomáticas posible que permitan automatizar los procesos de extracción de entidades cartográficas. Por lo general estos trabajos presentan gran complejidad dada la variada casuística de las entidades cartográficas y la heterogeneidad de los datos de partida, lo que supone un reto a la hora de elaborar algoritmos funcionales, robustos y automáticos. Parece lógico que la adecuada detección de entidades cartográficas será de utilidad en aplicaciones como la planificación urbanística, la ordenación del territorio o la toma de decisiones en el ámbito de la geografía. Esta tesis pretende realizar una serie de contribuciones a la automatización en la creación y actualización de bases de datos de coberturas del terreno e inventarios de mobiliario urbano. Entre las principales aportaciones de este trabajo se encuentran el desarrollo de una serie de metodologías capaces de detectar entidades tales como láminas de agua artificiales, bordes de carretera, arbolado y mobiliario urbano a partir de imágenes aéreas multiespectrales y datos LIDAR, registrados tanto por sensores aéreos como móviles terrestres. Dichas aportaciones han culminado con la publicación de cuatro artículos en revistas científicas de impacto. En esta tesis, a la que se ha dado el formato de compendio de artículo, se incluyen los artículos tal como han sido publicados. En ellos se detallan cada una de las investigaciones realizadas. Cada artículo incluye un estado del arte actual de la materia de estudio, se explica la implementación y funcionamiento de los

algoritmos desarrollados, se evalúan y discuten los resultados obtenidos y se analizan las conclusiones alcanzadas.

Palabras clave: teledetección, reconocimiento de patrones, LIDAR, imágenes aéreas / satélite, coberturas del terreno, mobiliario urbano

List of Terms and Acronyms

2D Two-dimensional
3D Three-dimensional
ALS Aerial Laser Scanner
BCN Base Cartográfica Numérica
BD Bhattacharyya distance
CLC Corine Land Cover
CNIG Centro Nacional de Información Geográfica
CORINE Coordination of Information of the Environment
DEM Digital Elevation Model
DL Digital Level
DSM Digital Surface Model
DTM Digital Terrain Model
FN False Negative
FOV Field of View
FP False Positive
GI Geometric Index
GIS Geographic Information System
GLONASS Global'naya Navigatsionnaya Sputnikovaya Sistema
GMES Global Monitoring for Environment and Security
GNSS Global Navigation Satellite System
GPS Global Positioning System
ICA Independent Component Analysis
IGN Instituto Geográfico Nacional (National Geographic Institute)
IMU Inertial measurement unit
JCR Journal Citation Report
JM Jeffries – Matusita distance
LIDAR Light Detection And Ranging
LULC Land Use Land Cover

MINP Minimum Number of Points
MIR Middle Infrared
ML Gaussian Maximum Likelihood
MLS Mobile Laser Scanner
MDNWI Modification of Normalized Difference Water Index
MRF Markov Random Fields
NIR Near Infrared
NDSM Normalize Digital Surface Model
NDVI Normalized Difference Vegetation Index
NDWI Normalized Difference Water Index
NDSPI Normalized Difference Swimming Pool Index
OL Octree Level
PCA Principal Component Analysis
PLR Probabilistic Label Relaxation
PLR2 Second order Probabilistic Label Relaxation
PLR3 Third order Probabilistic Label Relaxation
PNOA Plan Nacional de Ortofotografía Aérea
PNOT Plan Nacional de Observación del Territorio
PNT Plan Nacional de Teledetección
RADAR Radio Detection And Ranging
RAG Region of Adjacency Graph
RANSAC Random Sample Consensus
RGB Red, Green, Blue
ROI Region Of Interest
RX Reed and Xiaoli algorithm
SAM Spectral Angle Mapper
SAR Synthetic Aperture Radar
SIOSE Sistema de Información sobre Ocupación del Suelo
SPOT Satellite Pour l'Observation de la Terre
SVM Support Vector Machine
TLS Terrestrial Laser Scanner
TM Thematic Mapper
TP True Positive

UAH	Universidad de Alcalá
UPV	Universitat Politècnica de València
UTM	Universal Transverse Mercator

CHAPTER 1

Introduction

*How many roads must a man walk down
before you call him a man?
How many seas must a white dove sail
before she sleeps in the sand?
Yes, how many times must the cannon balls fly
before they're forever banned?
The answer my friend is blowin' in the wind
The answer is blowin' in the wind.*

Bob Dylan

This first chapter introduces the reasons that have led to the development of the research showed in the following chapters and the objectives of the current investigation. Additionally, it highlights the general thesis structure and briefly summarizes the state of the art to provide a general idea of the thesis's work content.

1.1. Motivation

Recently, remote sensing data have become common and accessible for users. Also, the information they provide has a high level of detail and precision, thanks to sophisticated sensors and airborne platforms. Aerial images and orthophotos recorded by satellites or aerial platforms enable geospatial information professionals to perform geological, environmental, or cartographic studies without costly and laborious fieldwork. The use of this data is widespread, and its use has been driven by advances in different fields, such as optics and electronics. These advances allow the creation of sensors capable of taking information with very high spatial and spectral resolutions. The use of active remote sensing systems based on laser scanner technology (LIDAR, Light Detection and Ranging) and radio measurements (RADAR, Radio Detection and Ranging) has been successfully accepted as a complement to classical remote sensing 2D data. Laser scanner sensors are capable of measuring altimetric information by providing 3D point clouds, which is an information piece that aerial imagery do not include, at least in an immediately way.

Laser scanner sensors can be installed both in aerial (Aerial Laser Scanner, ALS) or terrestrial platforms (Terrestrial and Mobile Laser Scanner, TLS and MLS respectively). In any case, the final product is a dense point cloud that provides 3D information (x , y , z coordinates) of all those points of the terrain where the laser pulse emitted from the scanner is reflected. Continuous developments and advances in laser scanner sensors in terms of speed capture, spatial accuracy, and point density incrementally increased the use of 3D point clouds in topographic and photogrammetric applications. Remote sensing data, both in image or point cloud format, have significant advantages, including not having to be in direct contact with the studied objects, the high speed of data acquisition in large regions, and the possibility of repeating the measurement at different times, thereby obtaining multi temporal information of the studied scene.

However, a huge amount of multi-temporal information with high spatial and spectral resolution can hinder the treatment and supervised processing of the registered information. This is the remote sensing's big data problem: large amounts of available geospatial data are difficult to process by man-made techniques. For this reason, it is necessary to develop methodologies that automate the treatment and processing of remote sensing big data and allow cartographic entities detection and classification as automatically as possible. Thus, the developed procedures included in this thesis work provide a robust and accurate solution for the extraction and classification of land covers and urban furniture from multispectral imagery and 3D ALS and MLS point clouds.

1.2. Research Objectives

The main purpose of the research showed in this thesis work is the development of methods and algorithms for the segmentation, extraction, and automatic classification of cartographic entities from both aerial and satellite multispectral images and 3D point clouds registered by ALS and MLS. The development of post-classification methods to improve the accuracy of classification algorithms is another goal of the current research.

The accuracy and effectiveness of the developed methods for land cover extraction, classification, and post-classification have been tested with satisfactory results in synthetic, aerial, and satellite images with different spatial and spectral resolutions. The methods developed for urban street furniture extraction have been tested in datasets representing different urban settings and registered by various measuring equipment. This testing has been done to verify the effectiveness and robustness of the developed methods in datasets recorded by sensors with different characteristics and in urban areas with different configurations and types of street furniture. This variety and heterogeneity of the input data and studied areas allow accurate testing of the performance of the developed methodologies in measurements with different casuistry. An effort has been made to automate the operation of every developed algorithm in order

to minimize the user intervention. Thus, the main contribution of this research is the development of methods to automatically detect and classify urban features from remotely sensed data. From aerial geospatial information (both images and ALS), two pipelines are proposed. One is focused on the detection and classification of man-made water surfaces, and the other consists of an algorithm aimed at improving classification procedures through a post-classification method based on contextual information. Regarding MLS 3D point clouds, a pipeline has been developed for road boundaries detection and estimation and another method for vertical urban furniture and trees extraction and classification. The following chapters explain the developed methods in detail.

1.3. Thesis Structure

The research presented in this thesis work is a compendium of four articles that have been published in different peer-reviewed scientific journal contained in the Journal Citation Report (JCR). These journals are included in disciplines such as Remote Sensing, Construction and Building Technology and Photographic Imaging Science & Technology. These articles detail the methodologies developed to extract and classify cartographic entities (such as land covers and urban furniture) from geospatial information, mainly aerial and satellite images and 3D point clouds recorded by ALS and TLS.

This thesis work is divided into five chapters: the first one is an introduction to the research subject: remote sensing science, geoscience data and products, pattern recognition, and image classification algorithms. In the following chapters 2, 3 and 4 the methods developed during the realization of this thesis work that have resulted in the publication of four articles in scientific journals are detailed. Every chapter includes a brief summary of the conducted research as well as its quality indicators, besides the full paper as it has been published in a scientific JCR journal. Finally, in the 5th chapter both general and particular conclusions and dissertations reached during the course of this thesis work are collected. Besides, it is detailed the lines of work that further research will follow.

1.4. Introduction to Remote Sensing Data, Remote Sensing Products and Pattern Recognition Techniques

This chapter introduces the main research topics presented in this thesis and briefly describes both remote sensing data and products as well as pattern recognition techniques. Through a better understanding of the science that underlies both fields (remote sensing and pattern recognition), a series of methods aimed at cartographic entity extraction and classification from remote sensing data have been developed.

1.4.1. Cartographic Science

The human need to graphically depict the surrounding world has made mapping and cartography, from their origin, closely linked to social, economic, and military activities. Cartography was first used in surveying applications to control river floods in rainy seasons. Nowadays, it is used in such diverse applications as the study of population flows [1], meteorology [2], or urban planning [3]. According to the International Cartographic Association (ICA, 1996), mapping could be defined as the set of studies and scientific, artistic, and technical operations, involved in the preparation, analysis, and use of letters, drawings, maps, relief models, and other means of expression which represent the earth, part of it, or any part of the Universe. The concept of mapping has been used throughout history in different ways depending on the training and knowledge of different map users. Mapping aims at the conception, preparation, drafting, and implementation of cartographic documents. It includes all necessary operations from the topographic survey carried out on the ground or collecting written information until the final cartographic document [4].

Although cartography is linked to human history, it is difficult to pinpoint its exact moment of origin. According to certain studies, it is believed that cartography originated in Asia Minor and Mediterranean cultures. Since its origin, the main objective of cartography has been to represent the “ecumene,”

that is, the world known by the different cultures that have occupied our planet throughout history. The birth of cartography as an applied science arises from man's need to represent the world around him. The technique for making the first maps consisted of simple, direct territorial observation and exploration. Rudimentary and limited availability of measurement tools, along with primitive graphics supports, meant early maps had low geometric and graphic quality. Distances were measured by the length of travel, and maps were produced manually on stone, parchment, or vellum, which made these early maps a mere approximation of reality. Additionally, their distribution was very limited. Scientific and technological advancements throughout history facilitated cartographers' work and represented an improvement in metrics and graphical maps' quality. The revolutionary ideas (introduced by Greek geographers such as Thales of Miletus and Aristotle) of the Earth's sphericity and the concepts of an equator, tropics, and poles were gradually adopted by cartographers on maps of that time. During the fifteenth century, the development of instruments to measure angles and accurately calculate the altitude of the sun (and consequently, latitude), such as the astrolabe, the quadrant, and the compass, gradually gave mapping the metric rigor it hitherto lacked. Other developments, such as the creation of printing and map projection systems [5], drove the creation and distribution of cartographic material. More recently, technological developments during the twentieth century in fields such as electronics, mechanics, physics, and optics revolutionized both cartographic production and map reading, enabling mass-produced maps that were easy to store, manipulate, and interpret. Advances in electronic technology made monitors, printers, and scanners available that facilitated access to mapping and simplified map generation and distribution.

The evolution of these technologies increased user access to cartography and provided cartographers with new tools to produce maps. However, one of the main impetuses of cartographic production comes from aeronautics. The development of aerial and satellite platforms capable of recording information

on the Earth's surface from the air, along with the production of optical sensors capable of taking in information from multiple bands of the electromagnetic spectrum, has provided an unprecedented amount of information, previously unthinkable. Most cartographic information is currently produced through software that utilizes computer-aided geographical information systems (GIS) design. Spatial information can be stored in databases. These tools have led to increasingly dynamic and interactive maps that can be digitally manipulated.

Since its origin, cartographic production has been carried out from field observation and inspection. The availability of geospatial information taken from an aerial perspective facilitated the final leap toward generating detailed mapping with high precision, both in terms of measurement and graphics. Processing and analyzing remote aerial information led to the science of remote sensing. Currently, this discipline is closely linked with cartographic production.

1.4.2 Remote Sensing

Remote sensing is the art and science of obtaining information about an object, area, or phenomenon by analyzing the data captured by a device that is not in contact with the studied element [6]. Remotely sensed information can be recorded by optical, acoustic, or microwave signals [7]. Remote sensing makes the measurement and study of dangerous and inaccessible areas possible. There are many fields of study that utilize remote sensing, including meteorology, agriculture, environmental analysis, or exploration of natural resources [8-10]. The research presented in this thesis focused on producing and updating maps of the Earth's surface from optical signals recorded by different remote sensing sensors.

1.4.3 Remote Sensing Data

Despite early attempts to capture aerial images from diverse aerial platforms such as balloons, kites, or even birds, it is generally accepted that modern remote sensing emerged in the early twentieth century. The developing of

airplanes and small satellites equipped with rudimentary cameras contributed to remote sensing development. Aerial photography was advanced rapidly during the First World War. It came up with the objective of monitoring and recognizing territories and terrestrial targets. The development and evolution of aerial and satellite platforms have allowed remote sensing information measurement to be applied on a global scale. Nowadays, there are a large number of remote sensing devices available. Depending on the manner in which information is measured, remote sensing sensors are classified as active or passive. Passive sensors measure electromagnetic solar radiation that is reflected in land cover. On the other hand, active sensors emit artificial radiation and measure the returning signal once it has interacted with the atmosphere and land surface. Multi- and hyperspectral satellite and aerial imagery are in the passive first group. RADAR and LIDAR sensors are classified as active. Both aerial, satellite, and synthetic images and aerial and mobile LIDAR have been used as input for the methodologies presented in this thesis. They have been also used as a ground truth for checking the validity of the developed methods and evaluating their accuracy.

1.4.3.1 Digital Image Data

An image is a visual representation that shows the visual appearance of a real or imaginary object. Photography is the process of capturing images by exposing them on light-sensitive material. A digital image is a numeric representation of a 2D image. Raster images have a finite set of digital values, called picture elements or pixels. The digital image contains a fixed number of rows and columns of pixels. Pixels are the smallest individual elements in an image, holding quantized values that represent the brightness of a given color at any specific point. Typically, pixels are stored in computer memory as a raster image or raster map, that is, a 2D array of digital values. These values are often transmitted or stored in a compressed form. Digital images can be created by a variety of input devices and techniques. Digital image processing is the study

and use of computer algorithms to perform image processing on digital images. It allows a range of algorithms to be applied to the input data to avoid typical analog image problems [11, 12].

1.4.3.1.1. Aerial and Satellite Images

Most of the aerial and satellite imagery data acquired by sensors on aircraft or spacecraft platforms are readily available in digital format. One of the main advantages of digital data is that it can be processed by computer either for machine-assisted information extraction or enhancement of its visual qualities to make it more interpretable by a human analyst. Digital image properties used in remote sensing are defined by measuring remote sensors characteristics, essentially by spatial, spectral, and radiometric resolution [13]. Spatial resolution is defined as the smallest angular or linear distance that a sensor can measure. Because digital images store information in pixels (generally square shaped), spatial resolution could be defined as the length of one side of a pixel measured in the terrain. This resolution is determined by several factors, such as the distance between the sensor and the measured object, the angle of vision, or the instantaneous field of view (IFOV). Spatial resolution is usually expressed in meters per pixel. Radiometric resolution can be defined as the minimum amount of energy required to increase the digital level (DL) by one. Radiometric range is the number of DLs that a sensor can discriminate between and is usually expressed in bits per pixel. Radiometric resolution is comparable to the gray tones in a black-and-white photograph as both are directly related to the contrast [14, 15].

One of the most significant characteristics of image data in a remote sensing system is the wavelength or range of wavelengths used in the image acquisition process. That is, those wavelengths to which the sensor is sensitive. Every surface has a characteristic response to electromagnetic radiation, allowing different types of land cover to be identified through their spectral signatures. Achieving this identification requires electromagnetic spectral information with

sufficient detail in terms of length intervals and spectral range. Each spectral range in which a sensor collects information is known as a spectral band or channel. The spectral resolution of a sensor is expressed as the number of bands in which it records information. Remote sensing sensors are classified into multispectral and hyperspectral depending on the number of electromagnetic spectrum-sensitive bands. Multispectral sensors are composed of a relatively low number of bands (no more than 20), and these are not necessarily adjacent to each other. These sensors register information from the electromagnetic spectrum in a discreet manner. Meanwhile, hyperspectral sensors are formed by a greater number of bands (several hundred), measuring a continuous spectral signature.

Temporal resolution should also be taken into account in satellite sensors. Temporal resolution is defined as the repetition cycle or the time between two successive acquisitions of the same area. This resolution is important in those works in which the evolution of certain phenomena is analyzed. It makes no sense to speak of temporal resolution in airborne sensors as repeatability in airborne remote sensing data depends on the flight planning.

Once the image is taken, either from an aerial or satellite platform, a series of pre-processing procedures should be carried out to remove geometric and radiometric distortion arising during the image's capture. Radiometric distortions affect the DL of each pixel and may be due to distortions, sensor failure, or atmospheric effects. These effects are corrected with a number of adjustments that modify the DL of the original image to approximate the values that would have been obtained in ideal conditions. A detailed description of the most common radiometric corrections can be found at [16]. Regarding geometric corrections, these consist of a series of transformations aimed at moving from image coordinates to coordinates in a global reference system. This transformation is the process of georeferencing of the image [17]. Once these corrections are carried out, aerial/satellite images are ready to be used in remote sensing applications.

1.4.3.1.2. Synthetic Images

Image processing software, like all software, needs to be both verified and validated. A synthetic image is an artificial picture whose radiometric, spectral, and geometric properties are perfectly known and defined by the user. This knowledge enables users to generate images with specific characteristics, which is useful during software development, to verify that the produced algorithms are working properly. They can be used to test individual discrete functions as well as complex chains of functions to verify that code segments are working properly.

Regarding the validation methods, real images (both aerial and satellite) with manually-labeled ground truth can provide a quantitative evaluation, but it must be taken into account that the procedure of creating a ground truth is costly in terms of time and money. Furthermore, man-made ground truth has an inherent uncertainty level and sometimes different experts might label an image slightly differently. This uncertainty is rarely quantified because it is very labor intensive. With synthetic images it is possible to have an objective ground truth that can be used for quantitative evaluation of a developed algorithm and quantitative comparison against other methods.

1.4.3.2. Laser Scanner Sensors

In the last decades, advances in electronics, photonics and computer vision made possible to construct reliable laser scanner sensors, providing the possibility of measuring and processing dense point clouds in an efficient and cost-effective way. Laser scanners measurement sensors use a laser ranging instrument in order to capture and record geometry and textural information of visible surfaces, acquiring dense range data to a high degree of accuracy. [18]. What a laser scanner does is basically measures the (x,y,z) coordinates of millions of points, providing an accurate reconstruction of a real surface. There are two main basic measurement methods for optically measuring a 3D surface: time-of-flight measurement and triangulation. The measurement of the time

delay caused by light waves, created by the scanner sensor and travelling with a known velocity, moving from the source to a reflective target surface and back to the light detector offers an efficient method of evaluating distance. This kind of measurement is known as time-of flight or LIDAR (light detection and ranging) systems. This measurement may also be achieved indirectly through the phase measurement in continuous wave lasers. In this case, the range value is derived by comparing the transmitted and received versions of the sinusoidal wave pattern of this emitted beam and measuring the phase difference between them [19]. The triangulation method is based on the cosine law by constructing a triangle using a direction of illumination aimed at a reflective surface and a direction of observation at a known distance, commonly referred as baseline, from the illumination source. In both methods the acquisition of a 3D point cloud with a single laser beam requires a mechanism to move the laser beam over the surface of the measured object. There are a large number of different scan mechanisms that have been used in laser scanning. Some of them are the oscillating mirror, in which a swiveling mirror directs the laser pulse across the swath, the rotating polygonal mirror, in which a rotating polygon mirror is used for beam deflection or the glass fiber scanner, a type of mechanical scan made with a number of glass fibers arranged in a linear array directed down at ground. Depending on the platform in which the laser scanner is mounted, these measurement sensors can be classified into two types: aerial and terrestrial laser scanner.

1.4.3.2.1. Aerial Laser Scanner

Laser altimetry systems did not come into widespread use for precise topographical mapping until the development of differential GPS, which allows the scanner position to be known by horizontal and vertical coordinates with a high level of accuracy. Until the end of the 1980s, range measurements were done by laser profilers, but since the '90s profilers have been replaced by scanning devices. Nowadays, airborne laser scanning is a powerful and common

technique for generating high-quality 3D presentations of the landscape. The measurement principle of airborne laser scanning is based on the combination of two systems. One is the laser scanner sensor, which allows the measurement of distances from the airplane to the field through a laser scanning terrain illumination system. It is mounted on the fuselage of the airplane and continuously measures the surface while the aircraft is in the air. The other system consists of a GPS combined with an inertial measurement unit (IMU). Differential GPS measures the position and flying height of the aircraft by means of a GPS antenna mounted on the aircraft and at least one other GPS antenna seated on a ground control station with known coordinates. The IMU is responsible for measuring acceleration data (used to support the interpolation of the platform position on the GPS trajectory) and rotation rates (used to determine platform orientation). The combination of the laser scanner and GPS+IMU provides 3D point clouds with densities between 0.2 and 50 points/m². In addition to 3D coordinates, a LIDAR system also records the intensity of the reflected laser pulses previously emitted and, for each of them, can capture two or more echoes. Airborne laser scanners are sometimes complemented by a digital camera taking images simultaneously with the laser scanner, which provides spectral information to the point cloud. After a survey mission there are three types of available datasets: IMU and airborne global navigation satellite systems (GNSS) data, ground station GPS coordinates, and ranging data. In processing the data, first the GPS and IMU data are integrated with the ground station GPS to obtain the restitution of the flight path and its altitude. Then, these datasets are processed with range measurements to obtain the final 3D point cloud in a global coordinate frame. Some advantages of aerial laser scanning systems are their ability to provide high measurement density and high data accuracy regardless of the visibility conditions, with fast data acquisition and minimum amount of ground support due to terrestrial work is minimized. The main drawbacks are laser pulses' limited ability to penetrate

clouds, fog, and dense vegetation and to measure water and wet surfaces in angles away from the nadir direction.

1.4.3.2.2. Terrestrial and Mobile Laser Scanner

Laser scanning sensors not only can be placed on aerial platforms, but also in terrestrial stations. With regards to terrestrial laser scanning, two procedures can be distinguished: the static mode, known as Terrestrial Laser Scanning (TLS) and the kinematic mode, more commonly known as Mobile Laser Scanning (MLS). In both cases a 3D point cloud is measured and parameterized by 3D Cartesian coordinates. In the TLS mode the data collection is carried out from a base station: the sensor is fixed to the base station from which the point cloud is sensed. In this mode the point clouds refer to the respective station coordinate systems; to merge different measurements into one unique point cloud, they have to be properly registered and georeferenced. The main advantage of this scanning mode is the high accuracy and spatial resolution point clouds it can measure, whereas the principal drawback is the time-consuming measurement of large areas. The MLS mode is carried out from a sensor installed on a moving platform, typically a motor vehicle, train, or trolley, which allows faster measurements over more extended regions than the static mode. In MLS each observed scan point refers to an individual 3D coordinate frame; to mathematically link all the systems in a unique spatial reference system, the respective positions and orientations have to be observed using adequate equipment based on GNSS and IMU devices. A mobile mapping system is composed of a data capture unit consisting of laser scanners and digital cameras, a positioning and navigation unit for spatial referencing, and a time referencing unit. There are two main observation modes implemented in MLS: the stop-and-go mode and the on-the-fly mode. In the stop-and-go method, the scanner is mounted on a platform; the scans are taken in static mode where the scanner position and orientation do not change. After each scan, the vehicle changes its position and the next scan is taken. Thus, extended

objects are scanned in consecutive steps. In the on-the-fly mode, the vehicle in which the sensor is fixed is following a trajectory without stopping and the sensor is scanning continuously. One of the main advantages of MLS sensors is the efficiency, and hence the fast data capture, of extended objects.

1.4.4. Remote Sensing Products

Remote sensing measurement sensors register a large amount of geospatial information, both in 2D and 3D format. This measured information is not generally used in the same way in which it is recorded. It is subjected to various treatments and processes to produce the final remote sensing products, with applications in several fields of study. In the following subsections some of the main mapping products generated from remote sensing data are detailed.

1.4.4.1. Digital Elevation Models

Throughout cartographic history there has been several approaches utilized to represent the z -coordinate in maps. Contour lines or surface shading have been some of the most used techniques to represent altimetry. Nowadays, Digital Elevation Models (DEMs) are the most common tool to render the z -coordinate in cartographic documents. DEM is often used as a generic term for both Digital Surface and Terrain Models (DSMs and DTMs respectively), only representing height information without any further definition about the surface. A DTM is just a topographic model of the bare earth, containing the spatial elevation data of the terrain in a digital format. A DSM not only represents the terrain surface like a DTM, but also contains buildings and other objects which are higher and above their surrounding soil [20]. The difference between DEM and DSM gives a canopy height model (CHM). It is also called a normalized Digital Surface Model (nDSM), describing the height of the vegetation and other non-ground objects [21, 22].

A DEM can be represented as a raster grid or as a vector-based (TIN). DEMs can be built from land surveying (based on topographic works with a total

station or GPS) or from topographic maps. Nevertheless, they are commonly built using data collected through remote sensing techniques. Aerial and satellite images, taken by metric cameras mounted on aerial platforms, are a valuable data source for large-scale DTM production from photogrammetric techniques [23]. In addition to aerial imagery, laser scanner sensors have proven to be useful in extracting digital models. Thus, Airborne Laser Scanning technology (ALS) has demonstrated that laser altimetry is a reliable technology for determining accurate DSMs [24]. Although remote sensing measurement sensors are capable of detecting DSMs, several methods have been developed for the generation of DTMs from remotely sensed data [25, 26].

DEMs are often used in geographic information systems and are the most common basis for digitally-produced relief maps. Additionally, they are used in other applications such as, slopes calculation [27], viewshed analysis [28], or flood modeling [29].

1.4.4.2. Orthoimages

Orthophotographs are photographic images constructed from vertical or near-vertical aerial photographs. Any aerial photograph shows a characteristic known as relief displacement. Relief displacement is the geometric distortion that occurs due to elevation differences in the terrain being photographed [30]. An orthophoto, orthophotograph, or orthoimage is an aerial photograph that is geometrically corrected (that is, orthorectified) such that the scale is uniform and consistent: the photo has the same lack of distortion as a map. Unlike an uncorrected aerial photograph, an orthophotograph can be used to measure true distances [31] because the processes used to generate orthophotos remove the effects of terrain relief displacement such as tilt of the aircraft camera, relief, and lens distortion [32]. Thus, an orthophoto is an image in which the relief displacements caused by perspective projection are removed by taking the DTM into account during the rectification process. As a result of the rectification process, the resulting orthophoto is shown in parallel

(orthogonal) projection and at a constant scale. However, the buildings and any other objects above the terrain are not correctly placed in the resulting orthophoto due to these objects are not modeled in the DTM. Thus, these objects are distorted from their true location in the final orthophoto in the form of leaning buildings and warped bridges [33]. True orthophoto production overcomes such deficiencies. A true orthophoto is an orthophoto in which surface elements that are not included in the DTM are also rectified to their orthogonal projection [34]. True orthophotos are generated by taking the DSM into account instead of DTM during the rectification process. In a true orthophoto, objects like buildings and bridges are moved back into their true location and “blind spots” that are left behind are replaced with real imagery. From a mapping point of view, this leads to a more realistic presentation of the Earth’s surface since man-made structures are repositioned correctly and occluded areas are filled with real image information. True orthophotos are also used in terrestrial applications for a complete geometric and radiometric representation of architectural objects [35].

In Spain, there is a national program to produce orthoimages of all national territory, the National Aerial Orthophoto Program (PNOA, Plan Nacional de Ortofotografía Aérea). PNOA’s main objectives are conducting photogrammetric flights, processing and producing high-accuracy aerial orthoimages with 25 and 50cm spatial resolution, and a DEM, with an update period of 2-3 years, depending on the area [36].

1.4.4.3. Geographic Information Systems

A geographic information system (GIS) is a system designed to visualize, capture, store, manipulate, analyze, and interpret data aiming to understand relationships, patterns, and trends. GISs use geographic information and spatial databases as input. Concerning geographic data, it may utilize any previously described data, orthophotos, DEMs, or basic and derived cartography. In contrast, spatial databases (also called geodatabases) are databases optimized to

store and query data that represent objects defined in a geometric space. The combination of cartographic information and databases allow users to create interactive queries (user-created searches), analyze spatial information, edit data in maps and present the results of all these operations [37]. A GIS project can be distinguished into three main stages [38]:

- Data preparation. This is the early stage in which data about the study phenomenon is collected and prepared to be entered into the system.
- Data analysis. Collected data is carefully reviewed and analyzed: attempts are made to discover patterns and consultations are made on geodatabases.
- Data presentation. Results of earlier analysis are presented in an appropriate way, based on the input geographic information.

Since its origins, GISs have been well received in several disciplines. This acceptance is proven by their use in such diverse disciplines as agriculture [39], tourism [40], policy decision [41], or public health [42].

1.4.5. Big Data problem: automation of geospatial data treatment and analysis

At the beginning of remote sensing, geospatial data acquisition was expensive and inaccurate. This was due to the low optic and photographic technological development and the rudimentary existing airborne platforms. Thus, the major drawback in remote sensing's early years was the shortage of geospatial data and the difficulty of its distribution. Over time, advances in telecommunications, computer science, and electronics revolutionized remote sensing work, facilitating the making, distribution, and storage of geospatial information. Technological progress has been so rapid that the obstacles facing remote sensing have reversed. Thus, remote sensing's data scarcity has changed to data overabundance. In many cases, it is difficult to store and manage this large amount of information. Geospatial data, daily recorded from satellites and airborne platforms, represent such a large amount of memory that manual

processing, analysis, and interpretation are economically and temporally unworkable. This is the problem with big data: an enormous amount of information that is exponentially multiplied every second and must be processed quickly [43]. Remote sensing big data does not merely refer to the volume and velocity of data that outstrip the storage and computing capacity, but also the variety and complexity of the remote sensing data [44]. This information should be conveniently analyzed. That is why in several disciplines the current trend is the development of tools and algorithms to automate those tasks traditionally carried out by human operators. In the case of remote sensing, several procedures have been automated, such as the radiometric and geometric correction [45] or image mosaicking [46]. Pattern recognition techniques have been used to automate scanning, extraction, and classification processes of geographic features and cartographic entities.

1.4.6. Pattern Recognition Techniques

The development of computational machines and computers was a breakthrough in disciplines like engineering, mathematics, or physics because they faced the possibility of automating processes that would be unthinkable to be done manually. Artificial intelligence, taking advantage of computers' processing power, goes a step further and tries to provide intelligence to computers to help decision-making processes. Similarly, machine learning is a branch of artificial intelligence that aims to develop techniques where computers can perform a learning procedure, i.e. a process of knowledge induction. Machine learning can be defined as the study of computer algorithms capable of learning to improve their performance of a task by their own previous experience [47]. It can develop programs aimed at generalizing behaviors from unstructured information. Machine learning can be considered as an attempt to automate some parts of the scientific method by mathematical approaches [48].

Pattern recognition is a machine-learning discipline. This science deals with engineering, computer science, and mathematics processes related to the

information extraction from physical or abstract objects, with the purpose of determining patterns and establishing properties between sets of objects. Patterns are obtained from segmentation, feature extraction, and description processes in which every object is represented by a collection of descriptors. System recognition must assign a category or class to each object. A category is a set of entities that share some features that differentiate them from the rest. A basic pattern recognition system includes:

Sensor: the device responsible for data acquisition. In remote sensing works, active and passive aerial/satellite and terrestrial sensors are the most frequently used.

Feature extraction: features generation that allows data classification.

Decision indices selection: selection of those features more suitable to describe objects. In pattern classification, every considered object is classified into one of the considered categories using features that properly separate classes. Initially, the best set of features for the given classification problem is unknown. Thus, first the appropriate set of features must be determined. It is relatively easy to delete redundant features but difficult to add necessary features. Variable selection can be used either either in the qualifying or representation step. Variables used in the classification step must be representative of the classes to be extracted and must have good separability from each other, i.e., they must have a characteristic behavior in each of the considered classes.

Classification: classification is the last step of a pattern recognition procedure and involves labeling every considered element as belonging to a particular class using the available input data and computed decision indices. In the field of statistics, it is more properly referred to as allocation rather than classification. However, in this work the concepts of classification, labeling, categorization, and allocation are used as synonyms [49]. Depending on how the classifier algorithm works, there are two broad classes of classification procedures found in most applications that analyze remote sensing data: supervised and unsupervised

classifications. These are not, however, the only developed classification techniques, as fuzzy logic and anomaly detection algorithms have been also applied in detection and classification issues.

1.4.6.1. Supervised Classification

Supervised classification is a type of semiautomatic learning that requires *a priori* knowledge about the number and characteristics of the categories in which the input data will be classified. The implementation of these classification methods is composed of two phases. The first step consists of training fields designed for every considered class. These training fields provide information about the number of classes and their behavior in the considered decision indices. In the second stage, a classification algorithm labels those inputs to be categorized. The final quality of the classification procedure depends on the descriptors and training field's quality. The automation of supervised classifiers is complex due to the different characteristics and calibration of remote sensing sensors. Besides, certain phenomena presents a temporary or seasonal nature, as crop fields chlorophyll content or surface water bodies in swamps and lagoons, what difficult the generation of valid training fields in any situation. This variability implies that training fields should be available in each season for every land cover, which is a challenge for automating classification procedures. There are numerous supervised classification algorithms [50]. Some of the classifiers most widely used in remote sensing applications are maximum likelihood, nearest neighbor, neural networks, or support vector machine [51, 52].

1.4.6.2. Unsupervised Classification

Unsupervised classification, also known as clustering, is a classification without learning, which means that no *a priori* knowledge of considered categories is required to classify. Although one might think that these classifiers are less practical and accurate than supervised classifiers, there are many reasons why unsupervised procedures are valuable. In some cases, collecting and labeling a

large set of sample patterns can be surprisingly costly. In many applications, the characteristics of the patterns can change slowly over time (e.g. in automated food classification as the seasons change). If these changes can be tracked by a classifier running in an unsupervised mode, improved performance can be achieved. In other works, unsupervised methods can be used to find features that will be useful for categorization; there are unsupervised methods that provide a form of data-dependent smart preprocessing or smart feature extraction. In the early stages of an investigation, it may be valuable to perform exploratory data analysis and thereby gain some insight into the nature and the structure of the data. The discovery of distinct subclasses or major departures from expected characteristics may suggest significant alterations in the approach to designing the classifier [50]. Some of the unsupervised classifiers whose use is most widely used in remote sensing works are ISODATA and K-means [53, 54].

1.4.6.3. Fuzzy Logic

Even though supervised and unsupervised classification algorithms are the most widespread methods to extract and classify remote sensing data, other procedures exist to extract patterns in images. One of these procedures is the mathematical fuzzy logic. Developed in the 1960s by Prof. Lotfi Zadeh, fuzzy-set mathematics is a superset of conventional (Boolean) logic that has been extended to handle the concept of partial truth, i.e. truth values between "completely true" and "completely false." It was introduced as a means to model the uncertainty of natural language [55]. In artificial intelligence, fuzzy logic is used to solve problems related to industrial process control and decision systems in general. Fuzzy logic systems make an effort to simulate the way in which humans make decisions, with the advantage of being much faster. These systems are generally robust and tolerant of inaccuracies and noise in the input data. Conventional logic processors can manipulate strictly dual values, as true/false or yes/no. In fuzzy logic, mathematical models are used to represent subjective notions, such as hot/warm/cold, for specific values that can be

manipulated by computers. More information about fuzzy logic methods and applications can be found in [56, 57]. Fuzzy logic inference methods have been applied in this thesis as a method for pattern recognition in a land cover extraction.

1.4.6.4. Anomaly and Target Detection

Land covers and artificial and natural elements located on the ground have characteristics and properties at different electromagnetic spectrum wavelengths. In general, these properties are used to classify and discern from one another. Sometimes, certain entities have very different spectral properties than other elements of the set. In these cases, detection could be reduced to the extraction of those elements with a particular behavior, different from other elements of the package. Anomaly detection (or outlier detection) is the identification of items, events, or observations that do not conform to an expected pattern or other items in a dataset [58].

Anomalies are features of special interest to image analysts. In multi- and hyperspectral imaging, anomalies should be understood as those elements (objects or materials, whether artificial or natural) whose spectral signature differs from the surrounding ground. In the current literature, there are some methodologies and algorithms for the detection of abnormalities of the land, such as RX algorithm (Reed Xiaoli) [59], Spectral Angle Mapper (SAM) [60], or genetic algorithms. Once the anomaly detection algorithm is applied, it is the operator who decides whether to classify the detected anomalies as items of interest or consider them as image noise. Although the term "anomaly" is commonly used in the remote sensing domain and "outlier" in statistics, in this work anomaly detection will be considered equivalent to outlier detection in the object space.

In contrast to anomaly detection, target detection algorithms require some *a priori* information about the properties of the elements to be extracted. It could be said that anomaly detection methods are related to the unsupervised

extraction of unique elements in an image, and target detection corresponds with supervised classification, according to the terminology of pattern recognition.

CHAPTER 2

Land Use Land Cover (LULC) database updating: automatic land covers detection and classification

-Do you pray to the gods?

- The Old and the New.

- There is only one god, and His name is Death.

And there is only one thing we say to Death: "not today"

Syrio Forel and Arya Stark

Pattern recognition techniques have many applications. This utility is demonstrated by their use in several scientific disciplines such as medicine [61] or chemistry [62]. Pattern recognition has also been successfully used in remote sensing works for the extraction and classification of cartographic entities from

geospatial data. In recent times, the continuous evolution of cities, urban development, and the need to monitor land cover changes have led to the development of programs at different scales for generating and updating LULC databases. Thus, on a continental scale, Corine Landcover (Coordination of Information on the Environment) is the most relevant land use project in Europe, while SIOSE (Sistema de Información de Ocupación del Suelo en España) is the main land use program in Spain. In a more detailed approach, cities such as Melbourne [63] and Toronto [64] have created urban vegetation and street furniture inventories to keep control of their distribution and conservation status. LULC databases and urban furniture inventories are commonly generated using remote sensing data, such as aerial/satellite imagery and 3D point clouds. There have been attempts to automate the creation and updating of these databases with pattern recognition and image classification techniques. Despite these efforts, automating these tasks is a complex process whose performance is not always the intended outcome. Often, due to the lack of spatial and radiometric resolution or capture characteristics in remote sensing information, this information is no longer enough to achieve an accurate classification. In these cases, remotely-sensed data is complemented by field visits and visual inspection of the studied areas. Thus, photo interpreters and operators generate thematic maps from visual inspection of remote sensing information and field visits. These practices are very costly in terms of time and money. Besides, the final quality depends on the photo interpreter's experience. For these reasons, the current trend in remote sensing and thematic cartographic production is the development of automatic methods, allowing extracting cartographic entities with the most accurate possible precision and the less human operator intervention.

2.1. Land Use Land Cover Databases

LULC databases store information about the type of land cover that occupies a certain area and its socio-economic activities. Before proceeding in more detail,

it is appropriate to clarify what is meant by land use and land cover. These two terms, although sometimes used interchangeably, have different meanings and should be correctly differentiated.

- Land cover is related to the type of surface or those elements located on Earth's surface. It could be defined as "that continuous region with a set of specific attributes and specific values that characterize it." Asphalt, vegetation, bare soil, olives, or vineyards are land cover examples.
- Land use is a concept related to the socio-economic activities carried out on that ground and may overlap with the type of land cover. The land use must be understood as the type of socio-economic activity and legal peculiarities (in the same socio-economic sense) that occur in a region. Land use allows for contemplating various aspects of the activities located in a territory. For instance, within "conifer" coverage can be found very different uses, such as forestry coverage and the recreational use of it. Sometimes, land uses are not directly deducible through photo interpretation.

Land covers are observable and detectable from remotely sensed data; however, the detection of land use usually requires field visits and ancillary information, which complicate automation in the generation of land use databases. Since the late twentieth century, several programs for the development of LULC databases have been launched at different scales, from global (GlobCover), to continental (Corine), and national (SIOSE). Although an effort has been made to automate the generation of these databases, the majority of them are made by direct interpretation of remote sensing information and specific field visits.

2.1.1. Corine Land Cover

Corine is a European Commission program whose main objectives are i) the collection of information on the state of the environment in relation to certain priority issues for all Community Member States, ii) the coordination of data collection and the organization of information within Member States of the international community, and iii) ensure that information and data are both

consistent and compatible. Corine Land Cover (CLC) is developed within the Corine program. It is included in the Land Monitoring Core System of GMES (Global Monitoring for Environment and Security) [65]. CLC aims to produce and update a European LULC database at a scale of 1:100,000, which is useful for territorial analysis and European policy management. Corine divides land into three hierarchical levels and 44 land uses and covers. The program has three versions, updated in 1990, 2000, and 2006. The classification of the territory is made by photo interpretation of Landsat TM, Landsat 7, and SPOT4 in each update. More specifications of the project and its updates are described in [66, 67].

2.1.2. SIOSE

SIOSE (Sistema de Información de la Ocupación del Suelo en España), together with PNT (Plan Nacional de Teledetección) and PNOA (Plan Nacional de Ortofotografía Aérea), is part of PNOT (Plan Nacional de Observación del Territorio). This national program is directed and led by Consejo Superior Geográfico and Dirección General del Instituto Geográfico Nacional through the Subdirección General de Geodesia y Cartografía. The main objectives of this program [68] are:

- The application of the INSPIRE guidelines in measurement, maintenance, and distribution of geographic information obtained in Spain.
- Obtaining a GIS integrated and consistent throughout Spanish territory to enable different administrations to coordinate their decision-making processes.

Within PNOT, SIOSE's main objective is the generation of an LULC database throughout Spain with a reference scale of 1:25,000. SIOSE production is carried out through photo interpretation using SPOT 5 satellite images, PNOA orthophotos, Landsat 5 TM satellite images, and digital base map with a scale of 1: 25,000 (BCN25), as geometry and temporal reference information. Photo

interpretation works are reinforced by field work to settle questions concerning land cover allocation from aerial and satellite imagery. Spanish territory is divided into polygons and for each one a percentage of classes and attributes are assigned, in accordance with the SIOSE data model. SIOSE is currently produced at the national level at reference date 2005 (SIOSE 2005), with subsequent updates at reference date 2009 (SIOSE 2009) and 2011 (SIOSE 2011). A fourth update at reference date 2014 (SIOSE 2014) is currently being conducted. Technical information on production and updates to the SIOSE program are detailed in [69].

2.2. Paper N°1: Semi-automatic detection of swimming pools from aerial high-resolution images and LIDAR data

2.2.1. Summary

With the purpose of automating LULC database creation and updating, this article developed a semi-automatic methodology to detect artificial water surfaces in urban environments. This method inputs multispectral aerial images, with information in visible and near-infrared wavelengths, and an ALS point cloud. The process begins with image segmentation, grouping pixels that have common characteristics, then moving from a pixel level to a regional level. A graph adjacency region (RAG) is created in the segmented image to analyze every region and its neighboring segments in the segmented image. For each created region, a series of decision indices are computed. These are the descriptors needed to accomplish the classification process. Depending on the values of these decision indices, a mass of evidence belonging to each category is assigned to every region. This evidence is combined through the Dempster-Shafer evidence theory. For every segment, the probability of belonging to every considered category is computed. Finally, each region is assigned to the class with the greatest likelihood of belonging. The effectiveness of this method has been tested in a 0.5m spatial resolution aerial image and in LIDAR data with 0.5 points/m² density, collected from the city of Alcala de Henares in June 2012.

The proposed method for artificial water body extraction achieved an overall accuracy of 99.86% and kappa index of 0.788 in the studied area. These results are very close to those obtained with the Support Vector Machine (SVM) supervised classification algorithm, but with the advantage of not requiring prior classifier training.

2.2.2. Quality Indicators

This work has been published in Remote Sensing Journal, with an impact factor of 3.180 according to a 2014 Journal Citation Reports (JCR) evaluation and has been included in the top quartile in the Remote Sensing category. To date, this paper has been cited by others research works and has four references according to WOS (Web of Science) and SG. Following this work, some method details, partial results, and results in other datasets have been presented in different conferences such as the IGARSS 2012 (IEEE International Geoscience and Remote Sensing Symposium) [70] (this contribution has been cited by 4 other researchers, according to SG), the SPIE 2014 [71], the 16th World Congress of the International Fuzzy Systems Association, and the 9th Conference of the European Society for Fuzzy Logic and Technology (IFSA - EUSFLAT 2015) [72].

This publication is the result of work in cartographic feature extraction from geo-referenced spatial information conducted by the University of Alcalá, in collaboration with the Spanish Centro Nacional de Información Geográfica (CNIG), along with the National Geographic Institute (Instituto Geográfico Nacional, IGN). Specifically, this article is part of the European project "HLANDATA: Creation of value-added services based on Harmonized Land Use and Land Cover Datasets." The objective of this program is to provide harmonized geospatial data in according to European needs and work on the development of algorithms for automatic change detection. These algorithms are incorporated into the production process to reduce the processing time needed for LULC updating and to ensure useful, reliable, and quality results. During

2011, the CNIG, along with the IGN, performed all phases of the project in collaboration with the Polytechnic University of Valencia (Universitat Politècnica de València, UPV) and the University of Alcalá (Universidad de Alcalá, UAH) under cooperative agreements signed under the collaborative framework agreements between these universities. Specifically, the UAH research group analyzed and developed automatic methodologies for automatic LULC detection and impervious surface determination [71].

Article

Semi-Automatic Detection of Swimming Pools from Aerial High-Resolution Images and LIDAR Data

Borja Rodríguez-Cuenca * and Maria C. Alonso

Department of Physics and Mathematics, Alcalá University, Campus Universitario, Alcalá de Henares, E-28871 Madrid, Spain; E-Mail: mconcepcion.alonso@uah.es

* Author to whom correspondence should be addressed; E-Mail: borja.rodriguezc@edu.uah.es; Tel. +34-918-85-6748.

Received: 19 December 2013; in revised form: 19 February 2014 / Accepted: 24 February 2014 / Published: 25 March 2014

Abstract: Bodies of water, particularly swimming pools, are land covers of high interest. Their maintenance involves energy costs that authorities must take into consideration. In addition, swimming pools are important water sources for firefighting. However, they also provide a habitat for mosquitoes to breed, potentially posing a serious health threat of mosquito-borne disease. This paper presents a novel semi-automatic method of detecting swimming pools in urban environments from aerial images and LIDAR data. A new index for detecting swimming pools is presented (Normalized Difference Swimming Pools Index) that is combined with three other decision indices using the Dempster–Shafer theory to determine the locations of swimming pools. The proposed method was tested in an urban area of the city of Alcalá de Henares in Madrid, Spain. The method detected all existing swimming pools in the studied area with an overall accuracy of 99.86%, similar to the results obtained by support vector machines (SVM) supervised classification.

Keywords: feature extraction; land cover database; mapping updating; Dempster–Shafer; RAG; NDSPI

1. Introduction

Cartographic feature detection using aerial and satellite images began several decades ago. Detection has changed from being based on visual interpretation [1] to automated or semi-automated detection, in which human knowledge plays a complementary role to classification and decision/detection

algorithms [2]. As time passes, classification algorithms improve, and their accuracy and complexity increases. Several classification algorithms exist and range from very simple, such as minimum distances or Mahalanobis classifiers [3], to more complex, such as maximum likelihood classifiers [3], support vector machines (SVM) [4,5] or neural networks [6]. The latter methods are supervised algorithms; unsupervised algorithms, such as fuzzy clustering [7] or K-means, are useful when no training field is available. Supervised and unsupervised classification algorithms are not fully automatic methods. The current research trend in remote sensing is detecting land cover as automatically as possible [8,9]. Airborne laser sensors and LIDAR have proven to be great advances in land cover detection, complementing aerial and satellite image information. Since the appearance of this data, several works now use LIDAR to detect land covers in terrain. In [10], Song *et al.* presented a land cover classification using intensity and height data provided by a LIDAR flight; Antonarakis *et al.* performed forest and soil-type classification without multispectral images [11]. Both works are based only on LIDAR data. Other works combined aerial/satellite images and LIDAR information to detect different land uses and land covers (LULC). Charaniya *et al.* [12] classified roads, buildings, trees and soil from aerial images, digital elevation models and LIDAR data using a parametric supervised classification algorithm. Building reconstruction fusing aerial images and LIDAR was carried out in [13] by Rottensteiner and Briese. These authors detected buildings using a curvature-based classification.

The method presented in this paper is focused on water body detection, specifically swimming pools located in urban environments. They are land covers of high interest for several reasons, and authorities should have a database with the location of every swimming pool in a region for three purposes. The first reason is to maintain control of taxes and to have knowledge about the energy expenditures involved in maintaining these facilities. Second, the main use of swimming pools is for leisure, but they are an important water source that could be used for firefighting. Wildfires can cause important damages to people and the environment. Rapid detection and suppression of wildfires is key to reducing their destructive effects. Firefighting requires every available resource, and an adequate water supply is critical in a firefighter's arsenal. By utilizing a home's swimming pool, firefighters could have access to strategically placed water supplies. The problem is accurately and quickly identifying which residences have filled swimming pools at the time of the emergency [14]. Producing a database with the location of every swimming pool in a region could be helpful for firefighting [15]. Third, mosquito-borne diseases affect many people throughout the world. Water in swimming pools at unoccupied homes might not be filtered properly, and accumulated rainwater and decomposing leaves likely will not be removed from the pool, providing an ideal habitat for mosquitoes to live and reproduce [16]. The detection of swimming pools, which can provide a habitat for mosquitoes to breed, therefore, is a useful tool in mosquito abatement.

Several works are related to water body detection in open spaces from satellite images. Bo-Cai Gao proposed the Normalized Difference Water Index (NDWI), which provides good results in the detection of open water, such as lakes or rivers [17]. Hanqiu Xu [18] used another index, the Modification of Normalized Difference Water Index (MNDWI), which modifies the latter and provides better results. Zhang *et al.* proposed a method to extract water bodies from satellite images based on entropy, but the results were not satisfactory in small water areas [19]. Frazier and Page [20] detected water bodies on riverine floodplains from Landsat 5 images. Other works carried out flood extent mapping and coastline detection using Synthetic Aperture Radar (SAR) [21–24]. These works

are focused on large water body detection, and they provide good results for this type of land cover. These methods do not provide good results for small-surface bodies of water, such as swimming pools, due to the small size of these bodies and their different spectral response compared with other natural water surfaces [20]. Other works in the current literature present methods oriented toward swimming pool detection. Tien *et al.* [15] carried out swimming pool detection based on a supervised SVM classification applied to an aerial RGB image. The researchers obtained good results in the studied area, but as with every supervised classification method, a previous training field was needed. Galindo *et al.* [25] presented an algorithm to determine the location of swimming pools from a QuickBird image. In this two-step method, swimming pools are first localized in a color analysis phase. Then, the contours of each region identified as a pool are refined using the adjusted object's contour algorithm. This method correctly detected more than 93% of the filled swimming pools in the studied area, failing to identify mostly pools that exhibited occlusion and shadows. Myint *et al.* [26] compared swimming pools and other land cover extraction at the pixel and object levels. To detect swimming pools and water surfaces, they used a segmented QuickBird image and set two thresholds in the second and third component of principal component analysis (PCA). They correctly identified 99% of the swimming pools in the studied area. However, this method is not robust or repeatable, because PCA values change in every image, and the thresholds are not applicable to other images. In [14], Fitzsimmons and Buck presented a method to detect swimming pools from multi-spectral satellite images using the Spectral Angle Mapper (SAM) algorithm. This method provided good results, but requires an accurate training site to work properly, which is not always possible. To identify swimming pools that could serve as mosquito habitats, McFeeters [16] used the NDWI combined with high-resolution multi-spectral imagery and a geographic information system (GIS). This method detected almost 80% of parcels known to have swimming pools. Parcels not identified as containing swimming pools lacked a sufficient amount of surface water to be detected by the NDWI.

This paper presents a semi-automatic methodology to determine the locations of existing swimming pools in an urban environment using aerial images and LIDAR data. The proposed method is based on PCA, image segmentation, a region adjacency graph and the calculation of four decision indices. These indices are combined with the Dempster–Shafer theory to determine the locations of the pools. The results obtained are discussed along with three other methods in order to evaluate the outcomes of the proposed method. This paper is organized as follows. The materials used in the procedure are described in Section 2, and the methodology is discussed in Section 3. The results and the four studied methods are presented in Section 4, and our conclusions are presented in Section 5.

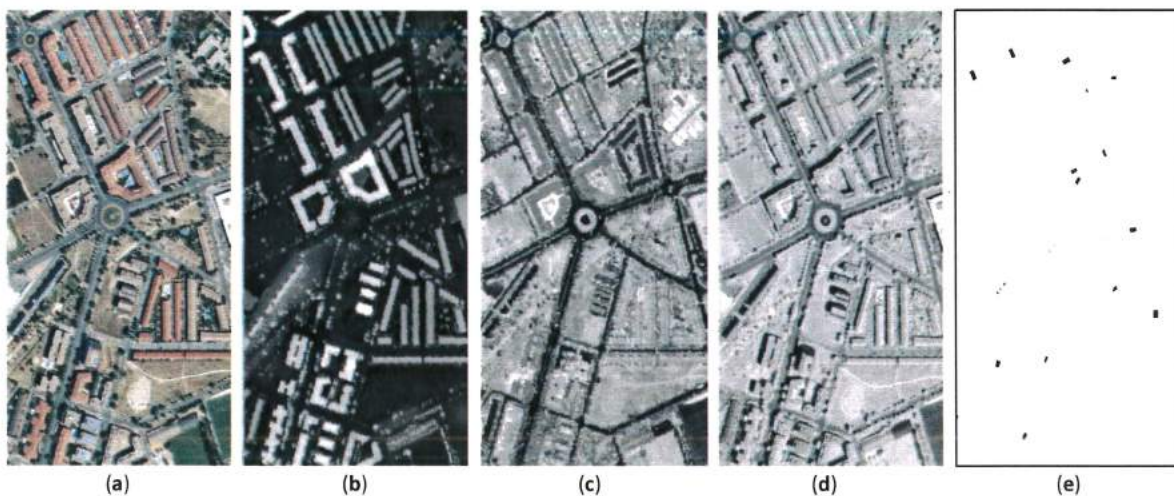
2. Materials

In this document, an aerial image and LIDAR data have been used as input datasets. The aerial image (Figure 1a) was taken by an UltraCam-Xp sensor. Its spatial resolution is 1 meter/pixel, and it is formed by four spectral bands: blue (B), green (G), red (R) and near-infrared (NIR). The image was taken in summer, 2010, in the Spanish city of Alcalá de Henares. The scene used in this paper has a dimension of 400×750 pixels.

LIDAR technology allows the calculation of the digital surface model (DSM) with a precision of the order of 20 cm in planimetry and 30 cm in height [27]. The combination of a sweeping beam laser

with inertial navigation systems and a GPS guarantees high geometric precision in the data. In this study, the LEICA ALS50-II (Leica Geosystems AG, Heerbrugg, Switzerland) sensor to capture the LIDAR data was used. The main features of this sensor are that it works at flight altitudes between 200 and 6000 m, and it has a frequency of 150,000 Hz, a field of view (FOV) between 10 and 75 degrees, a point density up to 150,000 Hz, an altimetry precision of 11 cm, a footprint between 0.3 and 5 m and a point density up to 12 points per square meter. Although a DSM could also be obtained by classical digital photogrammetry, this would be more expensive and slower to produce. The LIDAR data used in the present work correspond to a flight conducted in the summer of 2010. The flight was conducted at an altitude of approximately 1800 m above the ground; the scan angle was ± 20 degrees, and the scan frequency 1,000,000 Hz. The resulting point density was 0.5 points per square meter. The coordinate system is WGS84 with orthometric heights.

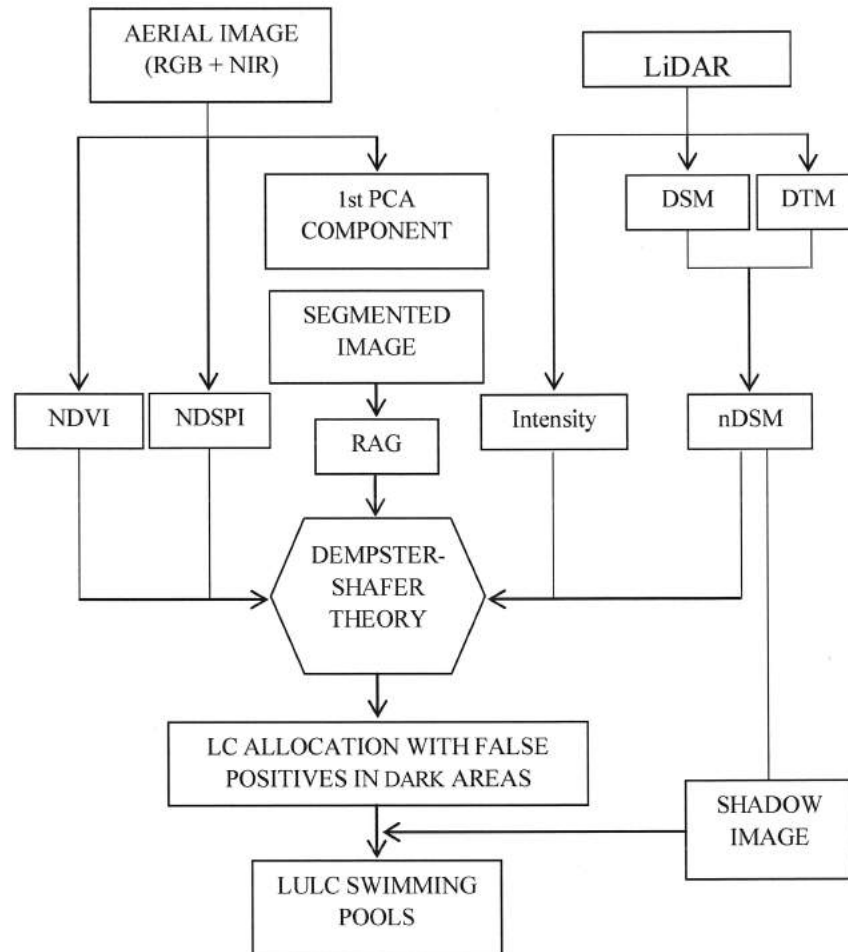
Figure 1. (a) Aerial RGB image; (b) digital surface model (DSM); (c) intensity LIDAR data; (d) near-infrared band from the aerial image; and (e) the ground truth made by the authors to determine the accuracy of each studied method.



3. Method

In this paper, a method for the semi-automatic detection of swimming pools in urban areas is shown. Identification and extraction begin with the lecture of the aerial image and the rasterization of LIDAR data. Next, segmentation of the aerial image into regions is carried out. The segmented image is used to create a region adjacency graph (RAG), which is useful to manage the image at the region level. Dempster–Shafer evidence theory is applied to determine which category corresponds to each region of the segmented image depending on the value of each studied decision index. The procedure ends with the reassignment of shadowed areas due to a bad behavior of the proposed index to determine the location of swimming pools in these dark regions. Figure 2 shows a flow chart of the method proposed in this paper.

Figure 2. Flow chart of the proposed method for the detection of swimming pools. NIR, near-infrared; PCA, principal component analysis; DSM, digital surface model; DTM, digital terrain model; NDVI, Normalized Difference Vegetation Index; NDSPI, Normalized Difference Swimming Pool Index; RAG, region adjacency graph; nDSM, normalized digital surface model; LULC, land uses and land covers.



3.1. Aerial Image Loading, LIDAR Data Rasterization and nDSM Generation

The first step in the procedure is reading the different bands involved in the process. Three optical bands (red (R), green (G) and blue (B)) are used from the aerial image, as well as the near-infrared band (NIR).

Height and intensity information was obtained from LIDAR data. The DSM was obtained from the first echo of each pulse after filtering the noise that was generated in the data capture process. The 3D clouds of the LAS file was rasterized using the method proposed by [28], who divided the data into regular cells, with each cell containing a determinate number of individual LIDAR points depending on the local density of each cell. The final elevation for each cell was calculated as the average of several LIDAR points contained within that cell; if a cell was without points, then nearest neighbor interpolation was applied. The cell size was 1 m. The DSM contained information regarding construction, vegetation and uncultivated ground, as seen in Figure 1b. The digital terrain model

(DTM) was generated as a product derived from the DSM after employing a semi-automatic method developed by [29]. This method consists of applying several filters to the DSM with the intention of removing the non-ground points. Next, minimal manual editing of the points that had not been properly classified was necessary. Finally, the normalized digital surface model (nDSM) was generated by calculating the difference between the DSM and DTM. LIDAR data come in a binary format according to the ASPRS norm. The LAS format includes information, such as GPS time and intensity, in addition to echoes of the pulses. In addition to height, intensity data was rasterized to add information to the process. The final intensity value of each pixel was calculated as the average of all intensity values of the LIDAR points contained in each cell, as in the rasterization of height data. The rasterization of DSM and intensity data are shown in Figure 1b,c, respectively. The near-infrared band of the aerial image is shown in Figure 1d.

3.2. Segmentation of First Component Image from PCA

Segmenting an image involves moving from the pixel-level to the segment-level in order to reduce its dimensionality. Segmentation involves group pixels that have similar properties; these pixels are treated as a set. Several methods for segmenting exist, such as clustering [30], thresholding [31] or region-growing [32]. A recent review of existing segmentation methods can be seen in [33]. In the work presented in this paper, region-growing segmentation was carried out [34].

A region-growing method is applied to a single band. Images used in this work are composed of several bands. To consider a single band, a principal component analysis (PCA) was applied to the four bands of the aerial image. Only the first component of PCA, which is the one with the most information, was considered. The first PCA component and the seeds from which the regions grow are the inputs of the region-growing method. Several ways to consider the seeds are present (randomly, consecutively, *etc.*). The present work considers as seeds every pixel that in a pass from left to right and from top to bottom of the first PCA component does not yet belong to any region. The process begins by taking as the first seed the pixel in the top left corner of the image. In the first step, the region is composed of the seed, and this region grows iteratively by comparing the seed with each neighboring pixel. The neighborhood for the studied pixel (i,j) is considered those pixels that share at least one edge. A predetermined threshold (α in Equation (1)) discriminates between the membership and non-membership of a pixel in a region. In a region of n pixels, the studied pixel (i,j) is assigned to this region if the difference between the digital value (DV) of the pixel and the mean DV of the studied region is lower than the threshold (α). Otherwise, the studied pixel is not assigned to the region, and it is considered a seed in the next step of the procedure. Subsequently, the next pixel that does not belong to any region is considered a seed. If a pixel is assigned to a region, it is not considered a seed in this procedure. The region-growing method ends when all pixels in the image are assigned to a region [35–37].

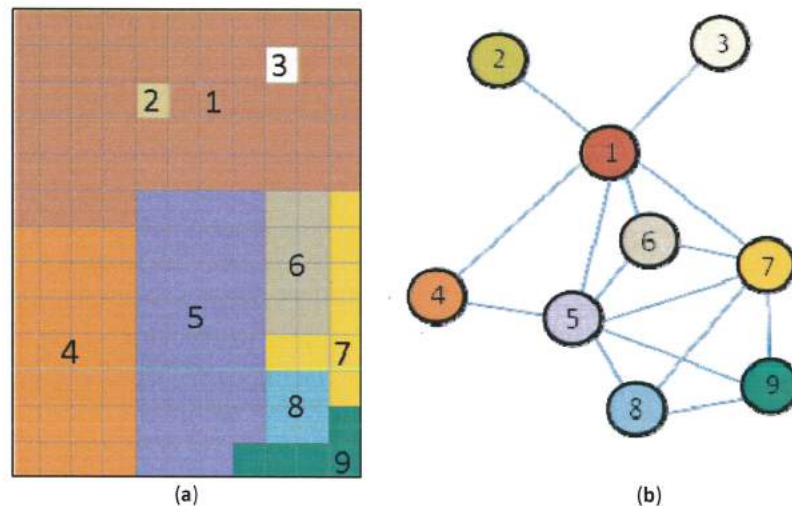
$$\frac{\sum_{k=1}^n DV_k}{n} - \alpha < \text{First PCA component}[i,j] < \frac{\sum_{k=1}^n DV_k}{n} + \alpha \quad (1)$$

3.3. Creation of a Region Adjacency Graph (RAG)

A region adjacency graph (RAG) is a type of data structure that facilitates merging and splitting operations. In this work, the RAG was used to represent regions contained in an image and the

relationship between them. Every node of the graph represents a region of the segmented image and contains its information. The edges are used to represent the connection between regions; edges link nodes that represent neighbor regions (see Figure 3). RAG is useful for emphasizing region adjacency and plays an important role in index calculation and assigning coverage.

Figure 3. (a) Synthetic image formed by nine regions and fifteen edges; and (b) corresponding region adjacency graph (RAG).



3.4. Decision Indices Computing

Even though the final result is a binary image that only represents swimming pools and background, five types of land covers were considered in the beginning of the procedure: vegetation, buildings, roads, bare soil and water bodies. Better results were obtained by increasing the number of classes. If only two classes are considered, there would be a class that includes elements of a very different nature. This would produce errors in the detection of land covers. Four decision indexes were used for the detection of the five land covers: the Normalized Difference Vegetation Index (NDVI), LIDAR intensity the nDSM and the index created by the authors of this work, aimed at detecting pools, the Normalized Difference Swimming Pool Index (NDSPI).

3.4.1. NDVI

The NDVI index was used to detect the location of vegetation land cover. The use of this index is very common in remote sensing applications to estimate the quality, quantity and development of vegetation from aerial or satellite images. The NDVI index has been used to, among other applications, monitor global vegetation [38] and crop growth [39] or to conduct deforestation studies [40]. The spectral response of vegetation has a characteristic shape with radiance in the near-infrared wavelength (NIR), much higher than in the bands of the visible spectrum, where it takes the lowest values in the blue (B) and red bands (R). No other categories considered have a spectral signature of these features. The NDVI index combines the information from the red and NIR bands to determine the location of vegetation (2) (see Figure 4a).

$$NDVI = \frac{NIR - RED}{NIR + RED} \quad (2)$$

3.4.2. LIDAR Intensity

LIDAR data not only provides a surface digital model, but offers other data, such as the image of the point density or the intensity of the reflected laser pulse at the surface. Asphalted surfaces provide small LIDAR intensity values [41]. This characteristic of the laser pulse intensity LIDAR has been used to detect roads in the image (see Figure 4b). Since a building may have a similar spectral response to an asphalted region, LIDAR intensity has been combined with nDSM to avoid false positives. Thus, only regions with low intensity values and low heights will be considered as roads.

3.4.3. nDSM

In order to detect high elements, an nDSM has been used. The nDSM was obtained from a DSM provided by LIDAR data and a DTM generated as a product derived from the DSM. The nDSM was generated by the research group to which the authors of this work belong [29] (see Figure 4c). The aerial images and the nDSM are geo-referenced properly and have the same spatial resolution, making it possible to combine and work with them at the same time.

3.4.4. NDSPI

Open water surfaces (oceans, rivers, lakes, *etc.*) have a characteristic spectral signature. The highest reflectance of these covers in the electromagnetic spectrum occurs in the blue wavelengths (0.45 to 0.47 μm) and the greatest absorption in the infrared wavelengths (0.7 to 300 μm). Figure 5 shows the spectral response of three sheets of open water. This dataset has been obtained from aerial images from different parts of Spain. The highest reflectance is obtained in the wavelengths corresponding to blue, except for Lake 2, in which the highest reflectivity occurs in the green wavelengths, but is close to the blue band. The lower reflectance occurs at the wavelengths corresponding to the NIR wavelengths. It has been observed that the spectral response of swimming pools is quite different to other sheets of open water. These differences may be due to the properties of pool water and the background color of these elements. It was observed that higher reflectance is retained in wavelengths corresponding to blue. However, the lowest reflectance takes place in the red band, instead of in the NIR wavelengths, as happened in the open water surfaces (see Figure 6)

Taking advantage of this characteristic of the spectral signature of swimming pools, the authors of this paper have developed an index to detect this land cover. This index is derived from the red (R) and blue band (B) (3) of the visible spectrum:

$$NDSPI = \frac{BLUE - RED}{BLUE + RED} \quad (3)$$

The latter index provides the highest values in swimming pools and shadowed regions. These false positives in the dark areas are corrected by generating an image of the shadows, as explained below (see Figure 4d).

Figure 4. (a) NDVI index image; (b) LIDAR intensity; (c) nDSM; and (d) the NDSPI index created by the authors.

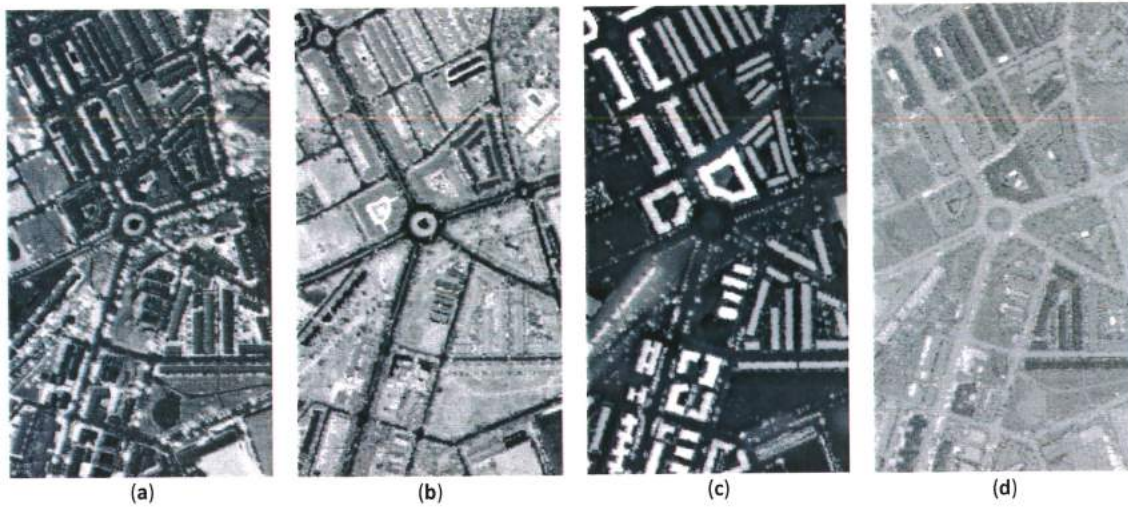


Figure 5. Spectral signatures of a river and two lakes in an aerial RGB-NIR image.

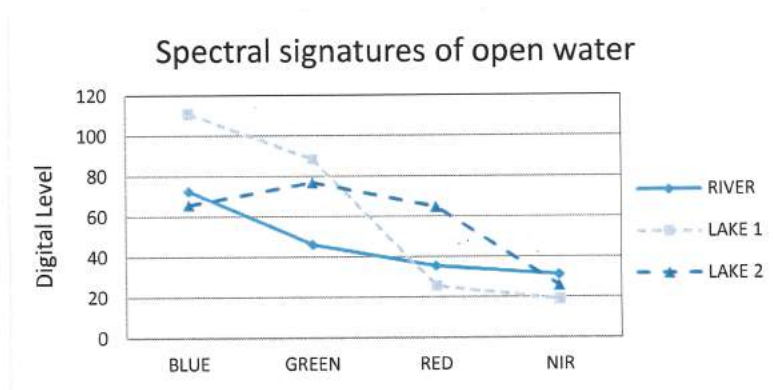
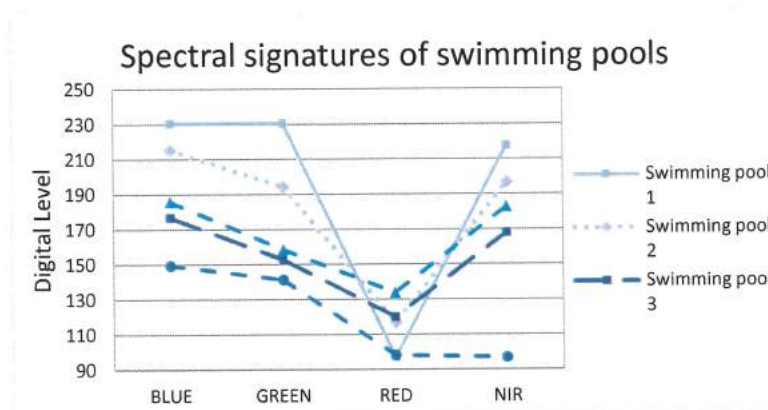


Figure 6. Spectral signatures of five swimming pools in an aerial RGB-NIR image.



3.4.5. NDWI

To test the efficiency of the proposed NDSPI and to determine which index has the highest accuracy, the NDWI (4) used in other works to determine the location of water bodies [42] was included in the procedure. For water extraction, NDWI was adopted and defined as:

$$NDWI = \frac{GREEN - NIR}{GREEN + NIR} \quad (4)$$

in which *GREEN* and *NIR* represent the green band and the near-infrared band, respectively. This index was designed to maximize reflectance of water by using green wavelengths, to minimize the low reflectance of NIR by water features and to take advantage of the high reflectance of NIR by vegetation and soil features. Thus, water features have positive values, while vegetation and soil have negative values.

3.5. Dempster–Shafer Theory

Evidence theory was developed by Dempster [43] and was later extended by Shafer [44]. For this reason, it is commonly referred to as the Dempster–Shafer theory. The objective of this theory is to model the way in which humans assign evidence to different propositions [45]. Evidence theory can be considered as a special case of fuzzy theory [46]. It is motivated by the difficulties found in the theory of probability, representing uncertainty. With the advent of the computational capacity of computers in the 1960s, it became necessary to create theories to model human thought. Classical logic and mathematics had very rigid models for this new phenomenon of scientific interest: the uncertainty that develops every human activity. Zadeh [47] was the first to propose and develop the theory of fuzzy sets.

The mathematical theory of evidence is a field in which data sources are treated separately, and their contributions are combined to provide a joint inference on the correct label for every pixel. Although evidence theory involves the numerical manipulation of quantitative measures of the test, the link between these measures and the original dataset is left to the user. This theory does not require a full probability model against the requirements of other approaches. It attempts to benefit from the use of sets of assumption hypotheses rather than separate hypotheses, as other approaches do. It aims to facilitate the reallocation of belief in hypotheses when evidence changes. It attempts to model the decrease of a working set of hypotheses from evidence accumulation [3].

3.5.1. Dempster–Shafer Theory in Land Cover Detection

The objective of the work presented in this paper is to generate a map with the location of five land covers in the studied area. The ultimate result is to detect only swimming pools, but five categories are taken into account: buildings, vegetation, roads, bare soil and pools. In the Dempster–Shafer theory, the building class is noted with *X* and vegetation with *Y*; *Z* corresponds to roads, *T* bare soil and *W* swimming pools. Also considered is θ as the inherent uncertainty in the theory of evidence. The frame of discernment, Ω , is formed by *X*, *Y*, *Z*, *T*, *W* and θ :

$$\Omega = \{X, Y, Z, T, W, \theta\}$$

For each decision index, the mass of evidence is noted by μ_i ($i = 1 \dots 4$, the number of decision indices considered): ($\mu_i(X)$, $\mu_i(Y)$, $\mu_i(Z)$, $\mu_i(T)$, $\mu_i(W)$, $\mu_i(\theta)$), with the assumption that $\mu_i(X) + \mu_i(Y) + \mu_i(Z) + \mu_i(T) + \mu_i(W) + \mu_i(\theta) = 1$, $\forall i = 1 \dots 4$ [48]. The probability of belonging to each category ($\mu_i(X)$, $\mu_i(Y)$, $\mu_i(Z)$, $\mu_i(T)$, $\mu_i(W)$, $\mu_i(\theta)$) is determined from the values taken by each index on every region according to some functions developed by the authors. Thus, a high NDVI value corresponds to a high probability of belonging to vegetation land cover and a low probability of belonging to the remaining land cover.

With the values, $\mu_i(X)$, $\mu_i(Y)$, $\mu_i(Z)$, $\mu_i(T)$, $\mu_i(W)$, $\mu_i(\theta)$, for the four decision indices ($i = 1 \dots 4$), the evidence combination rule of Dempster–Shafer is applied for every region in the image [43]. This combination (μ_{ij}) is an iterative process in which the knowledge acquired with a certain rate (μ_i) is combined with the following index (μ_j) Equation (5):

$$\mu_{ij} = (\mu_i \otimes \mu_j)(A) = \frac{\sum_{B \cap C = A} \mu_i(B) \mu_j(C)}{\sum_{B \cap C \neq \emptyset} \mu_i(B) \mu_j(C)} \quad (5)$$

The result of this process is, for every region, the probability of belonging to each of the considered categories.

3.5.2. Land Cover Allocation

Once the RAG was generated and the Dempster–Shafer evidence theory was applied, land cover allocation was carried out. As discussed in the previous section, the result of applying Dempster–Shafer to each region in the segmented image was the probability of belonging to each of the five categories. According to the Dempster–Shafer results, each region was assigned to the category to which it had the highest probability of belonging. Until this point, five categories have been taken into account, but at this point, they are reduced to two: swimming pools and background. Background land cover includes vegetation, buildings, bare soil and roads. The results of land cover assignment provide false positives in shadowed regions; some dark regions are labeled as water bodies. Figure 7 shows the regions detected as swimming pools after the land cover allocation based on probabilities obtained with the Dempster–Shafer theory.

3.6. Shadow Detection and Correction of Dark Regions Labeled As Water Surfaces

As seen in Figure 7, after the land cover allocation based on probabilities obtained with the Dempster–Shafer theory, several regions are labeled as pools that belong to other land covers.

This is because the spectral response of shadowed regions provides reflectance values in the red wavelengths lower than those that correspond to blue wavelengths (Figure 8). This property shows that some shadowed areas have a similar value on the NDSPI index as swimming pools. To correct this error, a reallocation of coverage in the shadowed regions that have been labeled as sheets of water is carried out. This is achieved by generating a shadow image from the flight data from which the image was taken. The shadow image is generated using an algorithm developed by our research group [49]. By combining this image and the RAG, it is possible to determine the regions that were in a shadowed area and were labeled as sheets of water. Those regions are assigned to the next category with the highest probability, different from swimming pools, according to the Dempster–Shafer results.

Furthermore, a minimum size of four square meters has been set for swimming pools, because pools under that size are not in consideration. Regions labeled as sheets of water that are less than 4 pixels have been assigned to other categories, as well (Figure 9).

Figure 7. (a) The detail of the studied area in RGB; (b) swimming pools detected in the former detail (it is possible to see two swimming pools correctly detected and two large false positive regions in dark areas); (c) another detailed imaged of the studied area in RGB; and (d) swimming pool detection (there are no pools in this area, but there are some false positives in shadowed regions).

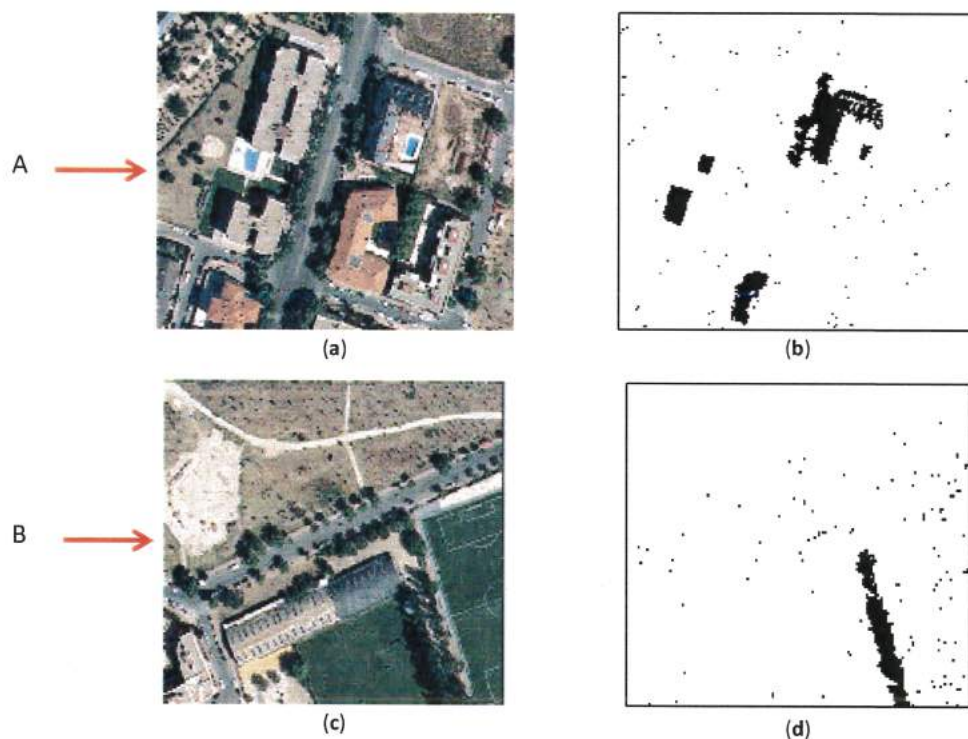


Figure 8. Spectral signatures of swimming pools and shadowed areas.

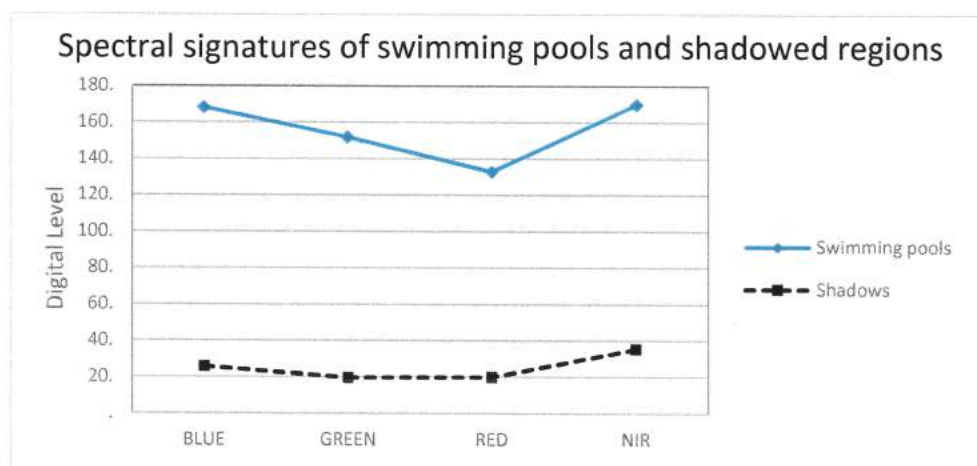
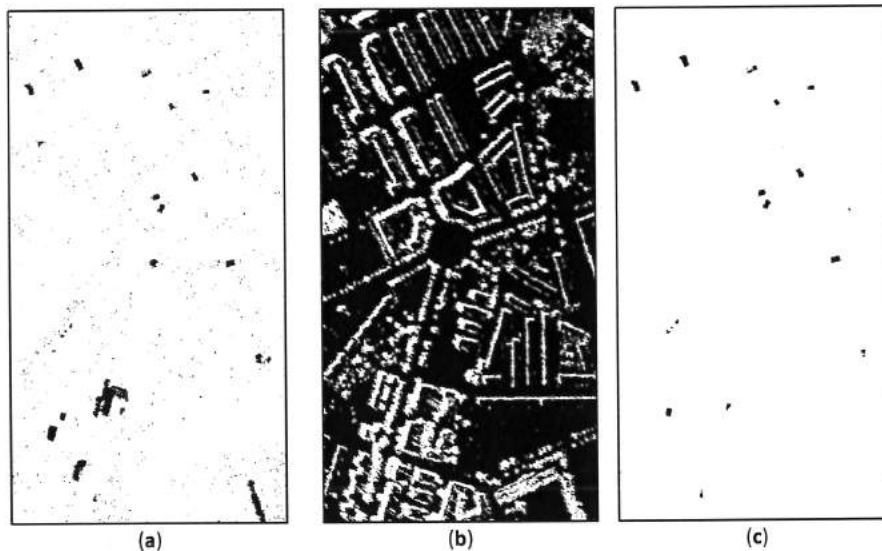


Figure 9. (a) Swimming pools detected with false positives in shadowed areas; (b) shadowed regions in the studied area (white color represents shadowed areas, black shows no dark regions); and (c) swimming pools detected after removing false positives in shadowed regions.



3.7. Reference Data and Evaluation

Two supervised classifiers, Mahalanobis and SVM, and the proposed method of replacing the NDSPI with the NDWI were carried out and compared with the proposed method to test whether the proposed semi-automatic method provides better results than a supervised classification. In order to quantify the results obtained with each method, each result was compared with a ground truth elaborated by the authors (see Figure 1e). The black regions correspond to swimming pools (SP) and the white regions correspond to the background (BG). The evaluation was carried out to determine the confusion matrix [50], kappa index and commission and omission errors, comparing the ground truth with the result of each studied method.

4. Results and Discussion

The results obtained for the image in Figure 1a, which correspond to the area studied in the city of Alcalá de Henares, are shown below. Figure 10 shows the results obtained for each classification in Details A and B. Swimming pools are represented in black, and white color is used for the background.

Figure 10a–e shows the results of each method studied for the first 200×200 detail. Figure 10b shows the Mahalanobis classification results, in which false positives in shadowed areas have occurred. Figure 10c,e correspond with SVM and NDSPI methods, and in both images, it can be observed that swimming pools are determined without false positives or noise. Figure 10d shows the details for the NDWI method. It can be observed that not every swimming pool is detected, and furthermore, false positives are found in vegetated areas. Figure 10f–j represents the results of the second 200×200 detail for every method studied. Figure 10g,i represents the results of the Mahalanobis and NDWI methods. It can be observed that both methods provide false positives for

some buildings. Both methods consider these buildings as swimming pools due to their spectral responses. Figure 10h,j shows the best results obtained with the SVM and NDSPI methods. The detection provided by both methods is good, and swimming pools are properly determined. The SVM classifier provides some noise in isolated pixels, as seen in Figure 10h. In order to quantify the results obtained with every method, each result has been compared with a ground truth elaborated by the authors (see Figure 1e). Black regions correspond to swimming pools (SP) and white regions to the background (BG).

Figure 10. Results for two 200×200 details of the studied area are represented in (a–e) and (f–j), respectively. RGB images of both details are shown in (a) and (f), (b) and (g) present the results obtained with Mahalanobis classification, SVM detection is presented in (c) and (h), NDWI results are shown in (d) and (i), and the results provided by NDSPI are (e) and (j).

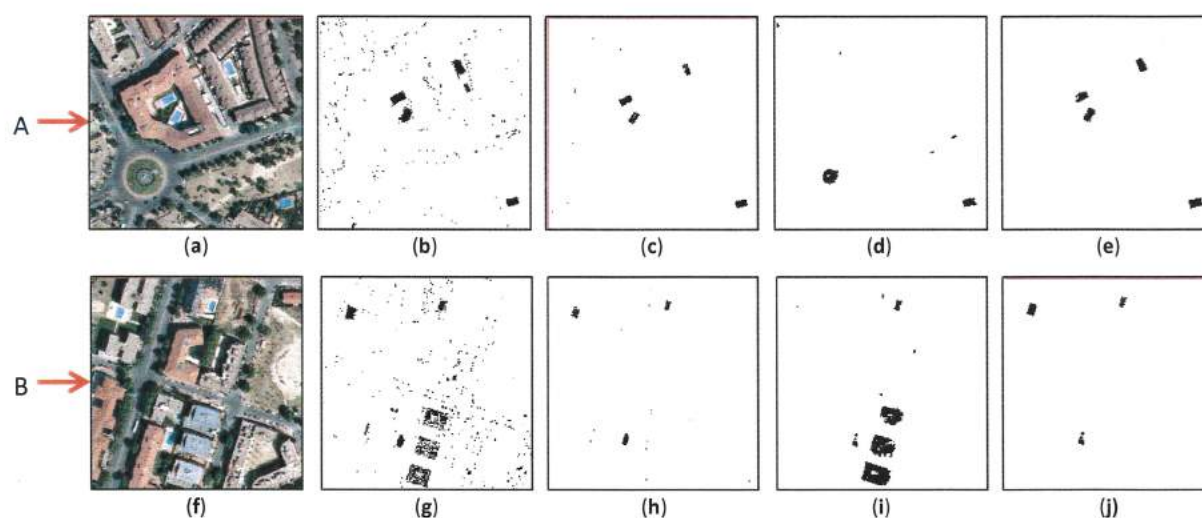


Table 1 shows the results provided by the studied methods. The Mahalanobis classifier provided lower accuracy (98.51%) than the SVM classifier (99.87%) did [51], due to labeling many of the pixels that belonged to the background as swimming pool. The kappa index of this method was also low, close to 0.3, and it produced a high commission error percentage in swimming pools and omission errors in the background, as more than 4000 background pixels were labeled as SP. However, only 90 SP pixels were incorrectly classified. This method provides a 91.53% producer's accuracy and 17.98% user's accuracy index [52]. The SVM classifier provided high accuracy, close to 99.9%, and its kappa index was 0.79. This means that the SVM supervised classification provides good results in swimming pool detection, as can be seen in the low commission/omission error rate. The highest percentage corresponded to SP omission error, as 312 SP pixels were incorrectly classified as background. The producer's and user's accuracy take values of 70.31% and 91.57%, respectively, for the SP category. The NDWI index provided high accuracy (close to 99.25%), but a low kappa index value, close to 0.19. It produced a high rate of commission and omission errors in the SP class: 781 SP pixels were labelled as BG, and 1468 BG pixels were classified as SP. In terms of producer's and user's accuracy, 25.69% and 15.54% are obtained, respectively. The results of the proposed method produced an accuracy of 99.86% and a kappa index close to 0.79. The commission and omission error

rates were similar to those obtained with the SVM classifier. The omission error in SP detection had the highest percentage, as 289 SP pixels were labeled as BG. The proposed method achieved a 72.5% producer's accuracy and 86.49% user's accuracy. According to these tables, the supervised SVM classification and the proposed method with the NDSPI index are the best methods. Both provide almost the same results, with accuracy close to 99.9% and a kappa index of 0.79.

Table 1. Confusion matrix of the studied methods, where columns are the ground truth and rows represent the classification results. SP, swimming pools; BG, background.

MAHALANOBIS				SVM			NDWI			NDSPI		
	SP	BG	Σ	SP	BG	Σ	SP	BG	Σ	SP	BG	Σ
SP	962	4387	5349	739	68	807	270	1468	1738	762	119	881
BG	89	294,387	294,476	312	298,706	299,018	781	297,306	298,087	289	298,655	298,944
Σ	1051	298,774	299,825	1051	298,774	299,825	1051	298,774	299,825	1051	298,774	299,825
(295,349/299,825) 98.51%				(299,445/299,825) 99.87%			(27,576/299,825) 99.25%			(299,417/299,825) 99.86%		
Kappa coefficient = 0.2965				Kappa coefficient = 0.7949			Kappa coefficient = 0.1901			Kappa coefficient = 0.7881		
	Commission	Omission		Commission	Omission		Commission	Omission		Commission	Omission	
SP	82.02%	8.47%		8.43%	29.69%		84.46%	74.31%		13.51%	27.50%	
BG	0.03%	1.47%		0.10%	0.02%		0.26%	0.49%		0.10%	0.04%	
	Prod. Acc.	User Acc.		Prod. Acc.	User Acc.		Prod. Acc.	User Acc.		Prod. Acc.	User Acc.	
SP	91.53%	17.98%		70.31%	91.57%		25.69%	15.54%		72.50%	86.49%	
BG	98.53%	99.97%		99.98%	99.90%		99.51%	99.74%		99.96%	99.90%	

5. Conclusions

Efficient methods to detect sheets of water automatically could be of vital importance for firefighting. In this paper, we propose a novel method for the semi-automatic detection of swimming pools in urban environments from aerial images and LIDAR data. The proposed method uses the NDSPI based on the spectral response of swimming pools, a region adjacency graph, and Dempster–Shafer theory to successfully identify the location of this cover in urban areas. The behavior of the proposed method was discussed in conjunction with three other methods to detect swimming pools: two supervised classifications (Mahalanobis and SVM) and the proposed method for detecting pools using the NDWI, which is useful in the detection of large bodies of water. The performance of the four methods was tested in a real dataset from the Spanish city of Alcalá de Henares. The creation of a ground truth of the studied region enabled numerical analysis of accuracy and determination of the kappa coefficient for the different methods.

The results show the performance of each method conducted on the studied dataset. Through a visual analysis, it can be seen that the proposed method using the NDSPI and SVM classifier produced the best results in the studied region.

The proposed method using the NDSPI achieved an accuracy of 99.86% and a kappa index of 0.79, better than the accuracy obtained with the Mahalanobis classification and proposed method with the NDWI (90.19% and 99.25%, respectively) and close to the 99.87% accuracy and 0.79 kappa index produced by the SVM supervised classification. It can be observed that almost every swimming pool was detected by the SVM classifier and proposed method. Although false positives were found with

some covers, commission errors were quite lower than in other methods, such as the Mahalanobis classifier. The main innovation of the proposed method is that it does not require prior training, as do supervised classifiers, and it only needs the correct threshold of every decision index used in the method to obtain good detection of swimming pools.

There are different types of water body land covers, such as oceans, seas and rivers, and there is no single best method or index to detect land covers in all cases, because the results vary by the spectral and spatial properties of each type of land cover. According to the results obtained, we can conclude that the method presented in this paper is useful in the semi-automatically determining of the location of swimming pools in urban areas from aerial images and LIDAR data.

Acknowledgments

We acknowledge with sincere appreciation the effort and time of the anonymous referees who have helped to improve the original manuscript with their criticism and suggestions. The authors would like to thank the Spanish Ministry of Science and Innovation for financial support, project No. CGL2010-15357/BTE.

Author Contributions

Both authors, B. Rodríguez-Cuenca and M.C. Alonso, designed the research, performed data analysis, and contributed with ideas, writing and discussion.

Conflicts of Interest

The authors declare no conflict of interest.

References

1. Holmes, W.S.; Buffalo, N.Y. Automatic photointerpretation and target location. *Proc. IEEE* **1966**, *54*, 1679–1686.
2. Voirin, Y.; Benie, G.B.; Deng-Chen, H.; Ko, F.; Goita, K. A Forest Map Updating Expert System Based on the Integration of Low Level Image Analysis and Photointerpretation Techniques. In Proceedings of 2002 IEEE International Geoscience and Remote Sensing Symposium (IGARSS), Toronto, ON, Canada, 24–28 June 2002; pp. 1618–1620.
3. Richards, J.A.; Jia, X. *Remote Sensing Digital Image Analysis*; Springer Verlag: New York, NY, USA, 2006.
4. Cristianini, N.; Shawe-Taylor, J. *An Introduction to Support Vector Machines and Other Kernel-Based Learning Methods*; Cambridge University Press: Cambridge, UK, 2000.
5. Cortes, C.; Vapnik, V. Support-vector networks. *Machine Learn.* **1995**, *20*, 273–297.
6. Bischof, H.; Schneider, W.; Pinz, A.J. Multispectral classification of Landsat-images using neural networks. *IEEE Trans. Geosci. Remote Sens.* **1992**, *30*, 482–490.
7. Gath, I.; Geva, A.B. Unsupervised optimal fuzzy clustering. *IEEE Trans. Pattern Anal. Machine Intell.* **1989**, *11*, 773–780.

8. Duda, T.; Canty, M.; Klaus, D. Unsupervised Land-Use Classification of Multispectral Satellite Images. A Comparison of Conventional and Fuzzy-Logic Based Clustering Algorithms. In Proceedings of 1999 IEEE International Geoscience and Remote Sensing Symposium (IGARSS), Hamburg, Germany, 28 June–02 July 1999; pp. 1256–1258.
9. Adams, J.B.; Sabol, D.E.; Kapos, V.; Almeida Filho, R.; Roberts, D.A.; Smith, M.O.; Gillespie, A.R. Classification of multispectral images based on fractions of endmembers: Application to land-cover change in the Brazilian Amazon. *Remote Sens. Environ.* **1995**, *52*, 137–154.
10. Song, J.H.; Han, S.H.; Yu, K.Y.; Kim, Y.I. Assessing the Possibility of Land-Cover Classification Using LIDAR Intensity Data. In Proceedings of ISPRS Commission III Symposium, Graz, Austria, 9–13 September 2002.
11. Antonarakis, A.S.; Richards, K.S.; Brasington, J. Object-based land cover classification using airborne LiDAR. *Remote Sens. Environ.* **2008**, *112*, 2988–2998.
12. Charaniya, A.P.; Manduchi, R.; Lodha, S.K. Supervised Parametric Classification of Aerial LiDAR Data. In Proceedings of 2004 Conference on Computer Vision and Pattern Recognition Workshop, Washington, DC, USA, 27 June–2 July 2004.
13. Rottensteiner, F.; Briesse, C. Automatic Generation of Building Models from LIDAR Data and the Integration of Aerial Images. In Proceedings of ISPRS Working Group III/3 Workshop on “3-D Reconstruction from Airborne Laserscanner and InSAR Data”, Dresden, Germany, 8–10 October 2003.
14. Fitzsimmons, B.; Buck, H. Automatic swimming pool identification for fire suppression. *Proc. SPIE* **2012**, *8515*, doi:10.1117/12.927774.
15. Tien, D.; Rudra, T.; Hope, A.B. Swimming Pool Identification from Digital Sensor Imagery Using SVM. In Proceedings of 9th Biennial Conference of the Australian Pattern Recognition Society on Digital Image Computing Techniques and Applications, Glenelg, Australia, 3–5 December 2007; pp. 523–527.
16. McFeeters, S. Using the Normalized Difference Water Index (NDWI) within a geographic information system to detect swimming pools for mosquito abatement: A practical approach. *Remote Sens.* **2013**, *5*, 3544–3561.
17. Gao, B. NDWI—A normalized difference water index for remote sensing of vegetation liquid water from space. *Remote Sens. Environ.* **1996**, *58*, 257–266.
18. Xu, H. Modification of Normalised Difference Water Index (NDWI) to enhance open water features in remotely sensed imagery. *Int. J. Remote Sens.* **2006**, *27*, 3025–3033.
19. Zhang, Z.; Prinet, V.; Ma, S. Water Body Extraction from Multi-Source Satellite Images. In Proceedings of 2003 IEEE International Geoscience and Remote Sensing Symposium (IGARSS), Toulouse, France, 21–25 July 2003; pp. 3970–3972.
20. Frazier, P.S.; Page, K.J. Water body detection and delineation with Landsat TM data. *Photogramm. Eng. Remote Sens.* **2000**, *66*, 1461–1467.
21. Silveira, M.; Heleno, S. Separation between water and land in SAR images using region-based level sets. *IEEE Geosci. Remote Sens. Lett.* **2009**, *6*, 471–475.
22. Henry, J.B.; Chastanet, P.; Fellah, K.; Desnos, Y.L. Envisat multi-polarized ASAR data for flood mapping. *Int. J. Remote Sens.* **2006**, *27*, 1921–1929.

23. Liu, H.; Jezek, K.C. A complete high-resolution coastline of antarctica extracted from orthorectified radarsat SAR imagery. *Photogramm. Eng. Remote Sens.* **2004**, *70*, 605–616.
24. Niedermeier, A.; Hoja, D.; Lehner, S. Topography and morphodynamics in the German Bight using SAR and optical remote sensing data. *Ocean Dyn.* **2005**, *55*, 100–109.
25. Galindo, C.; Moreno, P.; Gonzalez, J.; Arevalo, V. Swimming Pools Localization in Colour High-Resolution Satellite Images. In Proceedings of 2009 IEEE International Geoscience and Remote Sensing Symposium (IGARSS), Cape Town, South Africa, 12–17 July 2009; pp. IV-510–IV-513.
26. Myint, S.; Gober, P.; Brazel, A.; Grossman-Clarke, S.; Weng, Q. Per-pixel vs. object-based classification of urban land cover extraction using high spatial resolution imagery. *Remote Sens. Environ.* **2011**, *115*, 1145–1161.
27. Raber, G.T.; Jensen, J.R.; Schill, S.R.; Schuckman, K. Creation of digital terrain models using an adaptive lidar vegetation point removal process. *Photogramm. Eng. Remote Sens.* **2002**, *68*, 1307–1315.
28. Streutker, D.R.; Glenn, N.F. LiDAR measurement of sagebrush steppe vegetation heights. *Remote Sens. Environ.* **2006**, *102*, 135–145.
29. De Agirre, A.M.; Malpica, J.A. Constructing a Digital Terrain Model from LiDAR Data. In *Advances in Geoinformation Technologies*; Horak, J., Halounova, L., Hlasny, T., Kusendova, D., Vozenilek, V., Eds.; Institute of Geoinformatics: Ostrava, Czech Republic, 2010; pp. 47–59.
30. Wu, Z.; Leahy, R. An optimal graph theoretic approach to data clustering: Theory and its application to image segmentation. *IEEE Trans. Pattern Anal. Machine Intell.* **1993**, *15*, 1101–1113.
31. Haralick, R.M.; Shapiro, L.G. Image segmentation techniques. *Comput. Vis. Graph. Image Process.* **1985**, *29*, 100–132.
32. Bins, L.S.; Fonseca, L.M.G.; Erthal, G.J.; Li, F.M. Satellite Imagery Segmentation: A Region Growing Approach. In Proceedings of VIII Brazilian Symposium on Remote Sensing, Salvador, Brazil, 14–19 April 1996; pp. 677–680.
33. Yu Jin, Z. A Review of Recent Evaluation Methods for Image Segmentation. In Proceedings of Sixth International Symposium on Signal Processing and its Applications, Kuala Lumpur, Malaysia, 13–16 August 2001; pp. 148–151.
34. Rodriguez-Cuenca, B.; Malpica, J.A.; Alonso, M.C. Region-Growing Segmentation of Multispectral High-Resolution Space Images with Open Software. In Proceedings of 2012 IEEE International Geoscience and Remote Sensing Symposium (IGARSS), Munich, Germany, 22–27 July 2012; pp. 4311–4314.
35. Mehnert, A.; Jackway, P. An improved seeded region growing algorithm. *Pattern Recognit. Lett.* **1997**, *18*, 1065–1071.
36. Fan, J.; Zeng, G.; Body, M.; Hacid, M.-S. Seeded region growing: An extensive and comparative study. *Pattern Recognit. Lett.* **2005**, *26*, 1139–1156.
37. Sulaiman, S.N.; Isa, N.A.M. Adaptive fuzzy-K-means clustering algorithm for image segmentation. *IEEE Trans. Consum. Electron.* **2010**, *56*, 2661–2668.
38. Gutman, G. Monitoring Global Vegetation Using AVHRR. In Proceedings of 1998 IEEE International Geoscience and Remote Sensing Symposium (IGARSS), Seattle, WA, USA, 6–10 July 1998; pp. 2509–2511.

39. Schneider, S.R.; McGinnis, D.F. The NOAA AVHRR: A New Sensor for Monitoring Crop Growth. In Proceedings of the 8th International Machine Processing of Remotely Sensed Data Symposium, West Lafayette, IN, USA, 27–29 June 1982; pp. 281–290.
40. Malingreau, J.P.; Tucker, C.J. The Contribution of AVHRR Data for Measuring and Understanding Global Processes: Large Scale Deforestation in the Amazon Basin. In Proceedings of 1987 IEEE International Geoscience and Remote Sensing Symposium (IGARSS), New York, NY, USA, 18–21 May 1987; pp. 484–489.
41. Clode, S.; Kootsookos, P.J.; Rottensteiner, F. The automatic extraction of roads from LIDAR data. *Int. Arch. Photogramm. Remote Sens. Spat. Inf. Sci.* **2004**, *XXXVIII*, 231–236.
42. Qiao, C.; Luo, J.; Sheng, Y.; Shen, Z.; Zhu, Z.; Ming, D. An adaptive water extraction method from remote sensing image based on NDWI. *Indian Soc Remote Sens.* **2012**, *40*, 421–433.
43. Dempster, A.P. A generalization of Bayesian Inference. *J. Royal Stat. Soc. Series B Methodol.* **1968**, *30*, 205–247.
44. Shafer, G. *A Mathematical Theory of Evidence*; Princeton University Press: Princeton, NJ, USA, 1976.
45. Zarco, I.A.; Rodríguez, C.A.; Sendra, J.B.; Malpica, J.A.; Martín-Loeches, M.; Asensio, E.P.; Vela, J.T. Un procedimiento para elaborar mapas de riesgos naturales aplicado a Honduras. In *Anales de Geografía*; Universidad Complutense: Madrid, Spain, 2003; pp. 55–73.
46. Yen, J. Generalizing the Dempster-Schafer theory to fuzzy sets. *IEEE Trans. Syst. Man Cybern.* **1990**, *20*, 559–570.
47. Zadeh, L.A. Fuzzy sets. *Inf. Control* **1965**, *8*, 338–353.
48. Malpica, J.A.; Alonso, M.C.; Sanz, M.A. Dempster–Shafer theory in geographic information systems: A survey. *Expert Syst. Appl.* **2007**, *32*, 47–55.
49. De Agirre, A.M.; Malpica, J.A. Detecting Shadows in a Segmented Land Use Land Cover Image with LIDAR Data. In Proceedings of 2012 IEEE International Geoscience and Remote Sensing Symposium (IGARSS), Munich, Germany, 22–27 July 2012; pp. 5458–5461.
50. Jensen, J.R. *Introductory Digital Image Processing*; Prentice-Hall: New York, NY, USA, 1996.
51. Gigandet, X.; Cuadra, M.B.; Pointet, A.; Cammoun, L.; Caloz, R.; Thiran, J.P. Region-Based Satellite Image Classification: Method and Validation. In Proceedings of 2005 IEEE International Conference on Image Processing (ICIP), Genoa, Italy, 11–14 September 2005; doi:10.1109/ICIP.2005.1530521.
52. Congalton, R.G. Accuracy assessment and validation of remotely sensed and other spatial information. *Int. J. Wildland Fire* **2001**, *10*, 321–328.

© 2014 by the authors; licensee MDPI, Basel, Switzerland. This article is an open access article distributed under the terms and conditions of the Creative Commons Attribution license (<http://creativecommons.org/licenses/by/3.0/>).

CHAPTER 3

Urban furniture inventory: urban features extraction and classification from geospatial data

*Al andar se hace camino
y al volver la vista atrás
se ve la senda que nunca
se ha de volver a pisar.*

*Caminante no hay camino
sino estelas en la mar...*

Antonio Machado

Assets inventory consists of the collection and georeferencing in a database of all assets contained in an urban environment—from street furniture, such as traffic signals, to cultural heritage, trees, pavement, and sidewalks. The knowledge of the location and state of conservation of these elements guarantees and

facilitates city street furniture and urban resources management. Many cities have a street furniture inventory that must be regularly updated and aims to facilitate the control and monitoring of those infrastructures, parks, and facilities located in urban centers. Some cities, such as Melbourne [63], have developed street furniture plans to outline issues needing to be addressed regarding the provision of street furniture and recommending actions. Nowadays, cities are supposed to provide street furniture that is accessible, comfortable, heritage consistent, durable, and of high-quality design. All these specifications lead to the development and maintenance of accurate information about the city's street furniture assets in terms of condition and functionality. Collecting information for the preparation of these inventories is usually carried out through field visits and photo interpretation of remotely sensed data, mainly photographs and point clouds. This makes database creation and updating a slow and expensive process. In the investigations carried out and presented in this thesis as publications No.2 and No.3, two methodologies aimed at automating the processes of extracting and classifying street furniture from 3D MLS point clouds have been developed.

3.1. Paper N°2: Automatic detection and classification of pole-like objects in urban point cloud data using an anomaly detection algorithm

3.1.1. Summary

This research developed a method to automatically extract and classify vertical urban furniture and vegetation in an urban environment from 3D MLS point clouds. This method is developed to work with unorganized point clouds and does not require *a priori* additional information about the urban furniture typology or the MLS trajectory. Due to its simplicity, practicality, and robustness, this method could be an accurate, effective solution in economic and qualitative terms to produce and update urban furniture inventories. The pole-

like objects extraction method is based on an RX anomaly detection algorithm commonly used in hyperspectral imagery and successfully adapted to 3D point clouds organized in structure pillars limited in height. Classification procedure is carried out through a clustering algorithm, considering a series of geometric variables that have a well-differentiated behavior in the two considered categories: vertical artificial street furniture and trees. Besides, it has developed an index from geometric 3D point cloud features that allows the reconstruction of the MLS trajectory and the detection of horizontal and vertical surfaces in the studied street section. The efficiency of the extraction and classification method was tested in two point clouds that represent different street configurations and were measured by different laser scanner sensors. In both cases, satisfactory results were obtained, which shows the capacity and robustness of this method. The reported average accuracy for pole-like object detection from the two considered dataset was 95%, the classification procedure achieved an overall accuracy of around 95%, and the accuracy of both extraction and classification procedures was above 90%.

3.1.2. Quality Indicators

This contribution has been published under the title “Automatic detection and classification of pole-like objects in urban point cloud data using an anomaly detection algorithm” [73] in the Remote Sensing Journal, with an impact factor of 3.18 according to a 2014 JCR evaluation. More details of the method developed in this paper and partial results of this research have been presented in some international and national conferences, such as the IEEE International Geoscience and Remote Sensing Symposium 2015 [74] and the Spanish Remote Sensing Association XVI conference (Asociación Española de Teledetección, AET), held in Sevilla in October 2015 [75].

Following the research line in which this contribution is framed, with the development of computer algorithms for anomaly and target detection in cartographic entities, it has been carried out the COINCIDENTE project titled

"Anomaly and target detection in hyperspectral imaging", in collaboration with the Spanish Ministry of Defense. This project has made it possible to implement some algorithm and target detection algorithms in a computer application to quantify the ability of hyperspectral sensors to detect different types of anomalies and target objectives. The accuracy of the anomaly and target detectors has been tested in controlled experiments, using targets of different sizes and spectral signatures. Anomaly detection algorithms are useful for armed forces in several military applications such as the detection of masked weapons systems or the identification of contaminants in water and the atmosphere.

As a summary, the knowledge and application of algorithms and techniques for an anomaly detection algorithm in remotely sensed geospatial data allow the collaboration with multidisciplinary expert researchers and the development of useful tools for the exercise of their activities, either as part of the mapping industry or in the security field.

Article

Automatic Detection and Classification of Pole-Like Objects in Urban Point Cloud Data Using an Anomaly Detection Algorithm

Borja Rodríguez-Cuenca ^{1,*}, Silverio García-Cortés ², Celestino Ordóñez ²
and Maria C. Alonso ¹

¹ Department of Physics and Mathematics, University of Alcalá, Campus Universitario Ctra., Alcalá de Henares, 28871 Madrid, Spain; E-Mail: mconcepcion.alonso@uah.es

² Department of Mining Exploitation, University of Oviedo, Escuela Politécnica de Mieres, Gonzalo Gutiérrez Quirós, 33600 Mieres, Spain; E-Mails: sgcortes@uniovi.es (S.G.-C.); ordonezcelestino@uniovi.es (C.O.)

* Author to whom correspondence should be addressed; E-Mail: borja.rodriguezc@edu.uah.es; Tel.: +34-918-856-748.

Academic Editors: Juha Hyypä, Devrim Akca, Parth Sarathi Roy and Prasad S. Thenkabail

Received: 28 July 2015 / Accepted: 17 September 2015 / Published: 28 September 2015

Abstract: Detecting and modeling urban furniture are of particular interest for urban management and the development of autonomous driving systems. This paper presents a novel method for detecting and classifying vertical urban objects and trees from unstructured three-dimensional mobile laser scanner (MLS) or terrestrial laser scanner (TLS) point cloud data. The method includes an automatic initial segmentation to remove the parts of the original cloud that are not of interest for detecting vertical objects, by means of a geometric index based on features of the point cloud. Vertical object detection is carried out through the Reed and Xiaoli (RX) anomaly detection algorithm applied to a pillar structure in which the point cloud was previously organized. A clustering algorithm is then used to classify the detected vertical elements as man-made poles or trees. The effectiveness of the proposed method was tested in two point clouds from heterogeneous street scenarios and measured by two different sensors. The results for the two test sites achieved detection rates higher than 96%; the classification accuracy was around 95%, and the completion quality of both procedures was 90%. Non-detected poles come from occlusions in the point cloud and low-height traffic signs; most misclassifications occurred in man-made poles adjacent to trees.

Keywords: pole-like objects; feature extraction; pattern recognition; clustering; 3D point cloud; MLS; anomaly detection

1. Introduction

Creating and updating accurate maps and spatial databases has been demanded by various applications such as city management, urban planning, and intelligent transportation systems. For city management and urban planning, accurate land cover information is needed to document cities growth, make policy decisions, and improve land use planning [1]. For intelligent transportation systems, updated geodatabases that include the location of urban objects and traffic signs are required for terrestrial navigation and, of course, to decrease traffic congestion, lessen the risk of accidents [2], and develop autonomous driving systems [3]. Geospatial information has been widely used to meet these requirements for accurate and up-to-date remote sensed data. Light detection and ranging (LIDAR) technology has been used extensively in surveying and mapping. This technology provides three-dimensional data that complements the spectral information contained in two-dimensional images. Laser scanner sensors can be placed on aerial (airborne laser scanner, ALS) and terrestrial platforms (terrestrial LIDAR). Terrestrial LIDAR can be subdivided into two types: static and dynamic. Static terrestrial LIDAR technology (terrestrial laser scanner, TLS) data is collected from a sensor fixed in a base station. Thus, a small area can be mapped with high accuracy, but several scans are needed to cover large areas. Dynamic terrestrial LIDAR sensors (mobile laser scanner, MLS) are installed in vehicles provided with, as for ALS platforms, a navigation system based on global navigation satellite systems (GNSS) and inertial measurement units (IMUs). These devices determine the position of the mobile platform and the direction and orientation of the sensor at every moment [4].

Given that MLSs and ALSs capture data in large areas within short periods, both sensors are commonly used for urban applications, while the TLS is reserved for short-range applications, such as forest inventory [5], deformation monitoring [6] or heritage documentation [7]. ALS and MLS sensors provide three-dimensional (3D) point cloud data from mobile platforms, but significant differences exist between the two systems. ALS capture objects from the top view, while MLS and TLS collect data from the side-view, which makes the data taken by both types of sensors complementary. Additionally, the distance between the sensors and the ground is shorter in an MLS than in an ALS; consequently, the former performs measurements with higher resolution and greater density than the aerial sensors. ALS sensors cover large areas cost-effectively and rapidly but fail to capture details of small urban targets. Thus, MLS sensors are suitable for ground-based object modeling and to detect and extract elements located at street level, hardly achievable tasks in low density ALS data [8]. The main disadvantage is that MLS output files are large and hard to manage, forcing the development of organizing, cataloging, and optimizing methodologies to reduce the computation time significantly.

Many works in which point clouds are involved incorporate a preprocessing step or develop techniques that facilitate the treatment of the datasets and reduce the processing times. In some cases, a voxelization is performed to divide the point cloud space in a 3D grid of small regular cubes called voxels (volume elements) whose resolution depends on the size of the grid cells [9,10]. On a different

approach, the point cloud is decomposed into several two-dimensional vertical slices using the global positioning system (GPS) time as auxiliary information [11] or into horizontal sections, parallel and above the ground [12]. Other works analyze each scan line individually instead of considering the cloud as a whole [13,14]. Removal of parts of the cloud that belong to objects that are not the focus of the study [15] is another common technique. A segmentation procedure is also routinely used for point cloud handling. Segmentation is the process of grouping the points of the cloud into segments: points in the same region are given the same category and treated as a set [16]. Some segmentation techniques such as graph cut [17], region growing [18], and 3D connected components [19] are also applied to facilitate the handling of the point cloud.

Creating and updating the databases of vegetation elements and street furniture in urban environments is an important issue in 3D city modeling, city management, and urban planning. Some cities such as Melbourne, Australia, have created their own street objects database in order to improve the design, amenity, and quality of the public environment [20]. The creation of these inventories with field visits and photo interpretation of remote sensing data can be an expensive, tedious, and imprecise work. Thus, recent studies have also started to address the automatic or semi-automatic computerized extraction of urban objects. Generally, these types of elements, whether trees, lampposts, or signs, are cylindrical or conical in geometry. In [21] and [22] two methods for detecting generic cylindrical elements using Hough transform and Random Sample Consensus (RANSAC), respectively, were proposed. In [23] and [24] the authors searched vertical isolated elements in a point cloud previously structured in voxels or regions within a previous segmentation procedure. [25,26] developed different methods that also depend on the geometry of vertical urban elements. In these cases, the detection is based upon the study of the three eigenvalues obtained from the covariance matrix of each segment in which the cloud was previously decomposed. In [27], trees were detected from *a priori* information of geometric features, such as the roughness and the point density ratio. Continuing this trend, in [28] a knowledge-based classifier that uses the size, shape, height, and reflectance intensity information of each pole as descriptors is proposed. Another useful technique consists of simplifying the 3D point cloud by projecting it in several 2D planes, both horizontal and vertical, and searching and classifying street objects represented in the cloud. This approach is followed in [29] where a method for extracting trees that voxelizes the point cloud and studies layers at different heights is developed. Potential trees are represented by the voxels that are isolated in consecutive layers. In [30] the authors segmented every scan line based on the distance between adjacent points; clusters were merged to group the segments that represented the same pole-like object. The classification between poles and non-poles was based on *a priori* information of geometric features such as the length of the cluster, its shape, direction, and number of sweeps. In [15] an algorithm for extracting lampposts was proposed in which a gridding process is applied to the point cloud. In every cell of the grid, the height of the highest point is stored; those cells that are taller than an established threshold are considered lampposts. An automatic method for extracting individual trees is presented in [31]. It consists of separating trees from man-made objects by projecting 3D points on horizontal grid accumulators at three heights and performing a cross comparison through these layers. In [32] the point cloud was projected in planes orthogonal to the direction of the MLS trajectory before the extraction of street curbs. Among the non-road segments, the street light poles were segmented using a pairwise 3D shape context based on *a priori* information of the type of lampposts of the area.

In our approach a fully automated method for detecting pole-like objects and classifying them as trees and man-made poles is developed. This method detects and classifies vertical urban elements from MLS data by means of a three step procedure:

1. A preprocessing stage, including a reference frame transformation and a region of interest (ROI) isolation. These procedures diminish the size of the original point cloud, the number of false positives in the following procedures, and the computational effort of the successive stages.
2. Vertical urban elements detection using the Reed and Xiaoli (RX) anomaly detection algorithm. Previously the preprocessed point cloud is organized in a pillar structure.
3. Vertical elements classification into two classes (trees and man-made poles) using an unsupervised classification algorithm.

2. Method

2.1. Preprocessing

Three-dimensional point cloud data files from MLS data systems include not only X, Y, and Z point coordinates but also additional information such as GPS time, scan angle, or reflectance intensity information, for the millions of points contained in the point cloud. In the current paper, the preprocessing step is divided into two main stages: (i) transforming the reference frame and (ii) removing the parts of the cloud that are not of interest in this work (point cloud reduction).

2.1.1. Reference Frame Transformation

Point clouds registered by MLS sensors are properly geo-referenced in a global reference system by a navigation system (GNSS) and an IMU, which provide coordinates within a global frame to every registered point. The original coordinate system is now transformed by means of a translation and three rotations into a local Cartesian coordinate system. The origin of the new reference frame is located at the beginning of the MLS trajectory, the z-axis is coincident with the local vertical direction, and the x-axis is coincident with the average direction of the vehicle. The y-axis completes the dextro-rotatory set, which makes local (x,y,z) coordinates handier than the global ones.

2.1.2. Removing Uninteresting Points

In an urban environment, objects such as columns of buildings, fences, or decorative elements on façades that are not of interest in this work can be found; they are not urban elements and, in addition, they can be wrongly detected as pole-like elements in the detection procedure. Normally, these elements are located in distant areas of the mobile laser scanner data, inside buildings or local businesses; meanwhile, vertical urban furniture and trees are located on the sidewalks and the surrounded area of the road. To avoid these false positives, a method to remove all these uninteresting points from the original point cloud was developed. The procedure consists of two steps: (i) an index is developed based on geometric features to determine the vertical (mainly buildings and fences) and large horizontal surfaces (roads and sidewalks); and (ii) the 3D connected components are segmented to group the points that are part of the same surface.

Geometric Index Definition

To identify the façades of the point cloud, a geometric index was developed. Indexes developed from geometric features of the cloud have been adopted in previous works such as [33], in which an operator based on a normal vector was introduced as a preprocessing step of an object recognition procedure. The index elaborated in the current paper is called the Geometric Index (GI) and combines the information provided by the normal vector and roughness values of every point of the cloud:

$$GI_i = \frac{|N_{xi}| + |N_{yi}| - |N_{zi}|}{|N_{xi}| + |N_{yi}| + |N_{zi}|} \times \frac{1}{e^{R_i}} \quad (1)$$

In Equation (1) (N_{xi} , N_{yi} , N_{zi}) are the components of the normal vector \vec{N} in the point P_i and R_i is the roughness of the studied point. These values are measured from those points contained in a sphere of radius r centered in the studied point (P_i). Roughness (R_i) is defined as the distance between the studied point P_i and the least square best fitting plane comprising P_i and its neighborhood points inside the radius r sphere [6]. The first term of Equation (1) combines the three elements of the normal vector in a single value normalized in $[-1, +1]$. The behavior of the normal vector and its sensitivity to variations in the neighborhood size have been analyzed in five urban element types, easily identified in urban environments: façades, treetops, poles, roads, and cars. Significant differences have been found between these elements. In those elements with a horizontal flat surface that are determined as a trend surface (mainly roads and sidewalks), the vertical normal component (N_{zi}) takes higher values than the horizontal ones N_{xi} and N_{yi} . The opposite occurs on façades and fences, which are best fitted by vertical surfaces, in which horizontal normal vector components (N_{xi} and N_{yi}) take greater values than the vertical one. Other elements such as trees or cars present an irregular appearance because of their irregular and heterogeneous shapes. The roughness is included in the denominator of the second term of the GI Equation as an exponential to improve the separation between flat and rough surfaces. The lowest roughness values correspond to flat surfaces while higher roughness values take place in those elements with irregular shapes. According to the roughness study shown in Figure 1a, roughness R_i takes values around 0m in flat elements and higher values in rough surfaces; thus, term $\frac{1}{e^{R_i}}$ takes values around one for flat surfaces and lower in points that are further from the fitted plane. Consequently, the second term will not significantly affect the value of the GI in flat elements but will notably reduce it in rough surfaces, which helps to identify these elements in the point cloud. Since e^{R_i} is close to one for flat surfaces, this term has no effect on the GI but in contrast tends to substantially decrease the GI for rough surfaces, when $\frac{1}{e^{R_i}}$ is close to zero. To get the most suitable neighborhood size for the GI computation, normal and roughness features were studied in different radii values at the test sites. For small neighborhood radii (less than 20 cm), in many positions there are not enough point neighbors to compute the roughness and normal vector, making the distinction unclear. With large radii (more than 150 cm), the behavior of the GI in horizontal surfaces and elements at the ground level such as cars, pedestrians, or containers was quite similar. The neighborhood must be small enough not to consider points that belong to other elements but large enough to hold sufficient points to accommodate the interest features. Furthermore, the computational time increases exponentially with the radii and makes the process notoriously slow. Radii of 50 cm were set as optimal for extracting surfaces, because with this size (i) the GI values of flat surfaces, both horizontal and vertical, are suitably separated from other urban elements

and (ii) the processing time is acceptable. In Figure 1, the roughness and the GI with different neighborhood sizes are shown. These studies were conducted in the two test sites. Figure 1a shows that the lowest roughness values correspond to flat surfaces; while higher roughness values correspond to the elements with irregular shapes. According to Figure 1b, the highest GI values, close to one, correspond to building façades and the lowest, around -1 , to surfaces such as roads or pavement. Figure 2a shows the GI of the point cloud used as test site B in a color palette in which red corresponds to higher GI values, close to one, blue is reserved for the lowest GI values, and yellow and green represent the points with an intermediate GI value, around zero.

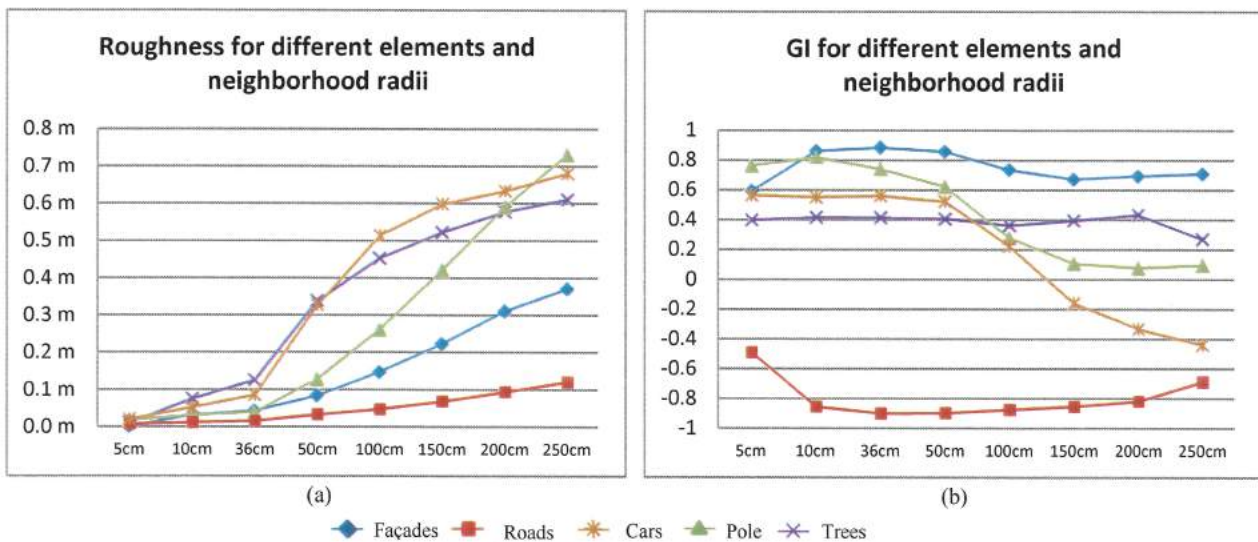


Figure 1. Behavior of the roughness (a) and GI (b) in five street elements for different neighborhood radii.

Extraction of Vertical and Horizontal Surfaces

To extract the vertical and horizontal surfaces, two thresholds α_V and α_H are set on the GI index. Those points (P_i) with a higher GI_i than α_V are considered to belong to a vertical surface; meanwhile, points with a GI_i below α_H are treated as horizontal surfaces. Point clouds obtained after thresholding are composed of vertical and horizontal surfaces but also by points that satisfy these conditions that do not belong to these surfaces. These points are usually isolated or belong to small urban elements, such as treetops or pole-like objects.

The 3D-connected components were segmented in favor of (i) grouping the points that belong to the same surface and (ii) removing isolated noisy points. Connected components analysis scans an image and labels its pixels into components if they are connected to each other (either four or eight connected) [34]. Once all groups have been determined, each pixel is labeled with an identifier according to the component the pixel was assigned to [35]. This technique is adapted to 3D point clouds structured in octrees. In a similar manner as for 2D images, the 3D connected components analyze the connectivity of the octrees and group in the same segment those that have a common side. In this case, the 3D connected components segmentation is defined by two parameters: the octree level (OL) and the minimum number of points per segment (MINP). The OL is related to the size of the octrees in which

the point cloud is organized. It must be large enough for every octree not to be empty of points but sufficiently small for different urban elements to belong to independent octrees. *A priori* knowledge of the point cloud density is required to set the appropriate OL. Optimal OL has been empirically established, by the authors, as five times the mean distance between the points of the cloud. The MINP determines the number of components and their size. The objective of this step is removing isolated noisy points, and only large segments that represent building façades and pavement are considered. Once the 3D connected components are segmented, the entire segments recognized as façades are grouped into a single point cloud. This operation is repeated for the segments that represent roads, resulting in three point clouds: the original measured by the MLS sensor, one containing points that belong to building façades, and one with roads and sidewalks information (Figure 2b).

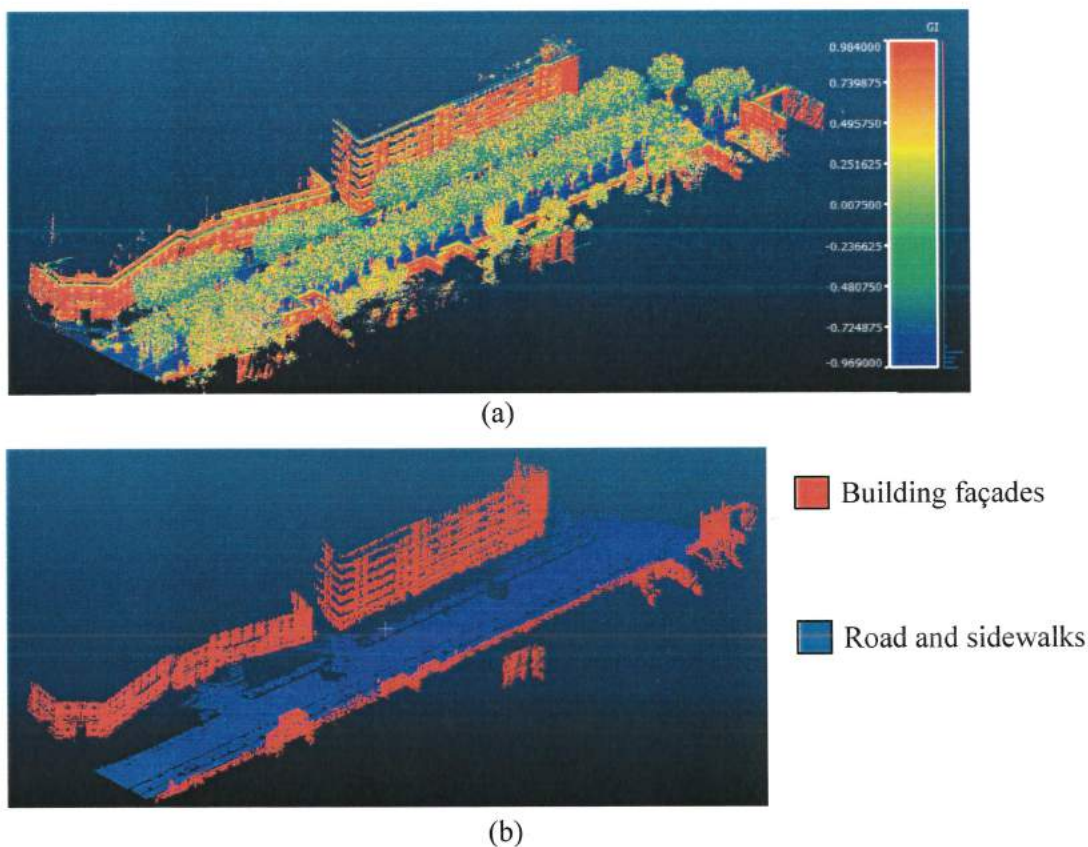


Figure 2. (a) GI in test site 2 and (b) façades detected after the connected components segmentation.

Original Point Cloud Reduction

The isolated region coming from preceding procedures that represents the road is analyzed using two-meter-wide sections, perpendicular to the x-axis of the local reference frame (Figure 3a). For each section, the center of the road and the location of building façades at both sides of the street are determined by analyzing the histogram of these point clouds. In every section, the road center is considered the modal class value in the y-coordinate histogram of the horizontal surfaces point cloud (Figure 3b). Thus, it is possible to approximately recreate the path followed by the MLS sensor, providing a kind of virtual MLS trajectory by joining the pavement center detected in each section.

Additionally, for every 2-m-wide section, the alignment of the existing buildings is established by searching the modal class values of the y-coordinate histogram at both sides of the road center. A new point cloud is then generated by removing the points that lie beyond the façade line at both sides of the street (Figure 3d). This procedure automatically reduces the volume of the original point cloud, speeding up the following processes and removing potential false positives caused by vertical building columns. Furthermore, since this method is applied in narrow sections 2 m wide, it also accurately and precisely eliminates building façades in curved street sections or difficult areas, such as road intersections.

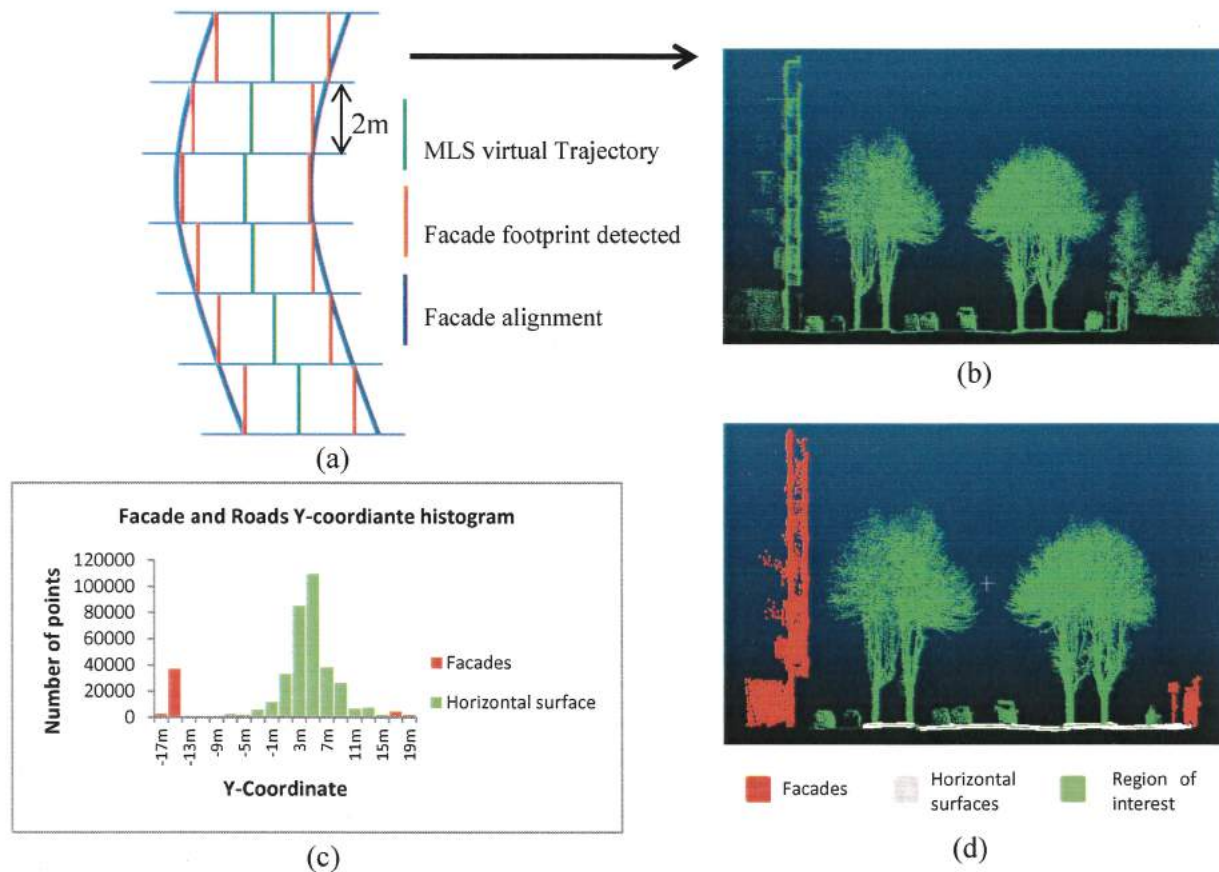


Figure 3. (a) Cloud MLS analysis in two meters width sections; (b) Original point cloud; (c) Histogram of façades and horizontal surfaces extracted and (d) Point cloud reduced: Isolated region of interest in green and removed façades in red.

2.2. Pole-Like Elements Detection

2.2.1. Point Cloud Structuring

MLS data is composed of several million points so analyzing every single element and its neighborhood is computationally expensive and unproductive in terms of feature extraction. To speed up the detection and extraction procedure, the point cloud obtained in the previous step is organized and analyzed in a 3D vertical pillar structure pattern (Figure 4) [36].

Every point of the cloud is associated with a pillar, and all the points belonging to the same pillar are considered a set. The point cloud is divided in a 2D ($m \times n$) grid composed of m columns and n rows.

Each cell of the grid represents a pillar. Every pillar has a unique identifier ID assigned from its (x,y) coordinates in the 2D grid. Thus, for every cell $c_i = (x_i, y_i)$, with $x_i \in [0, m]$ and $y_i \in [0, n]$ corresponds the identifier $ID_c = (m \times y_i + x_i)$.

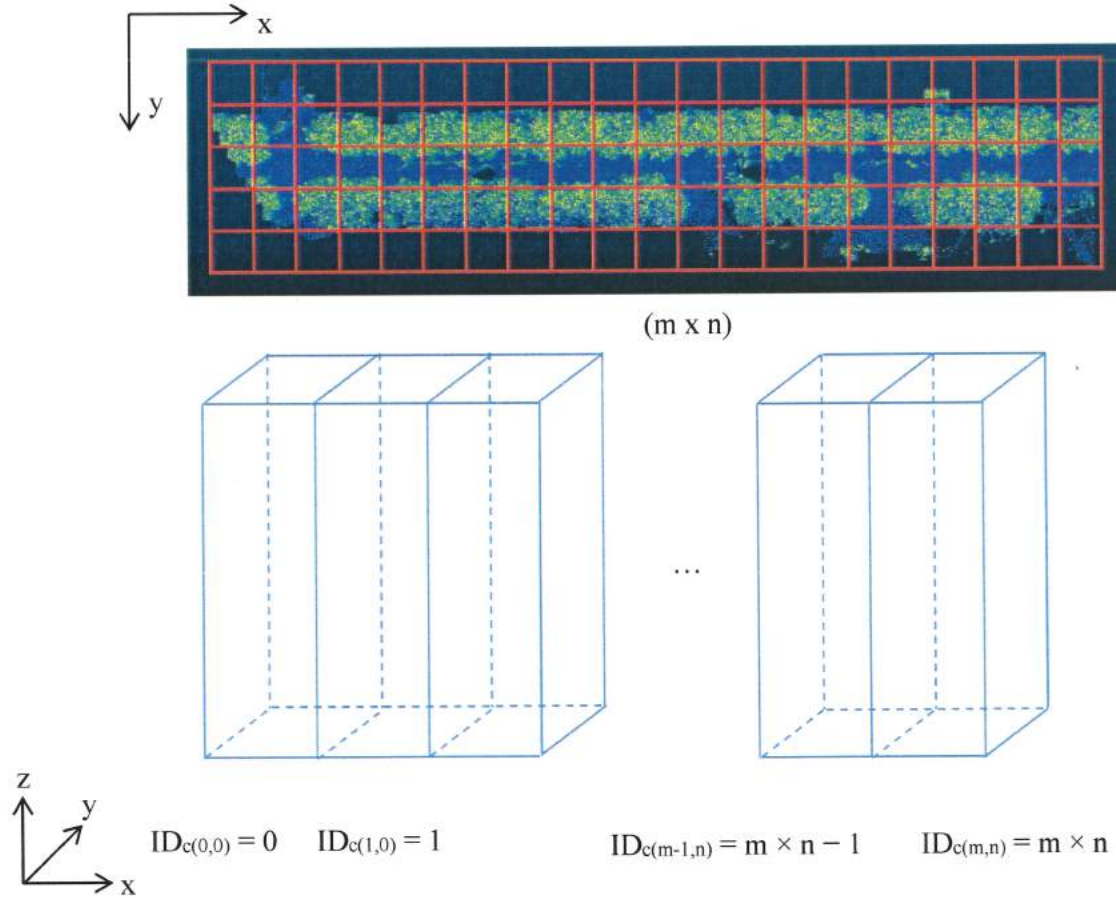


Figure 4. Creation of the pillar structure in the studied point cloud.

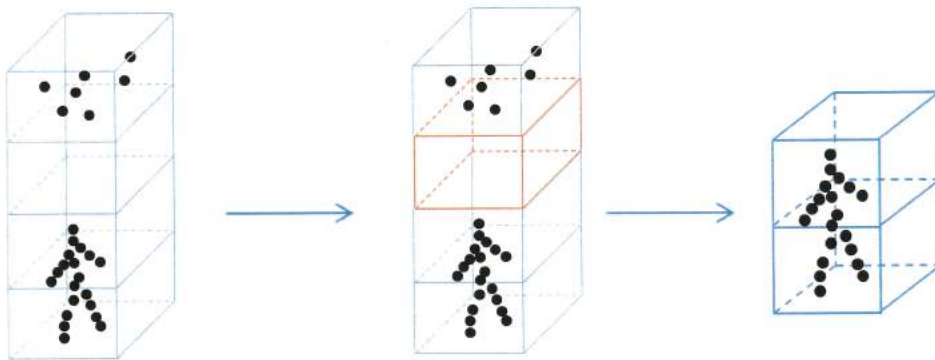


Figure 5. Pillar height is delimited until an empty voxel is found.

To avoid considering pillars as infinitely tall elements, the point distribution in each pillar is analyzed. This is achieved by decomposing the pillars into voxels of regular heights. The process starts searching the lowest occupied voxel, that is, the voxel with the lowest height that contains at least one point, and continues studying the voxels above it until an empty voxel is detected. Once a discontinuity is observed,

that is, the first empty voxel above the occupied ones, the points above the discontinuity, if any, are discarded and not considered in the following steps. Thus, every pillar is formed by the points whose z-coordinate is between the lowest occupied voxel and the first discontinuity (empty voxel), found in the pillar. After this operation, every pillar is formed only by the elements connected to the ground level and disconnected points that unnecessarily increase the weight of the pillar and may hinder the detection and classification process are removed (Figure 5).

2.2.2. RX Anomaly Detection Algorithm

Once the point cloud has been structured, vertical urban elements are extracted and classified from the pillars in which the point cloud has been decomposed. It is necessary to determine which pillars contain a target element and which not. The RX anomaly detection algorithm is applied with this goal. This algorithm is commonly used to detect outliers in hyperspectral images, but it can also be used in multispectral images. The RX algorithm was developed by Reed and Xiaoli Yu [37]. It is based on the Mahalanobis distance and follows Equation (2) [38]:

$$\delta_{RX}(P_i) = (r_i - \mu)^T K_{LXL}^{-1} (r_i - \mu) \quad (2)$$

where r_i is a vector in which considered features in the studied pillar P_i are saved, μ stores the mean values of the considered variables in the set of pillars of the whole point cloud, K is its sample covariance matrix, and L is the number of considered variables. i is the number of pillars in which the point cloud is structured. The minimum value of i is zero (the first studied pillar) and the maximum value depends on the size of the considered pillars. The Mahalanobis distance is used to calculate how far each pillar is from the center of the cloud formed by the other pillars, and the shape of the cloud is considered through K . Mathematically, the RX algorithm performs some kind of inverse procedure of the principal component analysis (PCA); this was proved by Alonso *et al.* [39]. Anomalies should be understood as those elements whose spectral signature differs from the terrain in which they are. Anomalies are significant features of special interest to image analysts. In a hyperspectral image, every band contains information from a certain wavelength of the electromagnetic spectrum. The RX algorithm detects those pixels for which, in any band of the hyperspectral image, exists an anomalous spectral response compared with the response of the rest of the pixels of the image. MLS point clouds do not provide spectral information, but some geometric features can be computed for each point and its neighborhood. These geometric features have singular behaviors in vertical elements, quite different from other street elements.

In this work, the RX algorithm is applied to three features for every pillar of the point cloud. Height difference and the points' spatial dispersion have been considered to detect those pillars that represent a vertical urban element. To study the behavior of street objects in the variables, pillars that represent horizontal surfaces and vertical elements were chosen as ground truth (Table 1).

Height difference (Δh): every pillar is formed by points whose z-coordinate is between the lowest occupied voxel and the first voxel discontinuity. The height difference is referred to the distance, in terms of the z-coordinate, between the lowest and highest points of all points belonging to a pillar. The pillars in roads or pavement areas present a low height difference; however, vertical elements show a larger height difference between their lowest and highest points. Most pillars of an urban point cloud correspond to horizontal elements because they are the most common ones in streets environments. As

can be seen in Table 1, the average value for the height difference in the full set of pillars is close to the trend of horizontal elements, with a low height difference (around 0.15 m).

Spatial dispersion is calculated from x- and y-coordinate dispersion (σ_x , σ_y). The distribution of the (x,y) coordinates of the points contained in every pillar depends on which element is contained in it. The standard deviation of both planimetric coordinates (x,y) are the dispersion measures used as a geometric feature. In Table 1, the average (x,y) dispersion in roads and pavement is around 0.14 m; in pole-like elements, the average dispersion is a bit lower, around 0.10 m.

The number of points contained in every pillar (density) in which the point cloud is organized has been used in other works as a feature for extracting urban objects with satisfactory results [40]. Furthermore, surfaces that are orthogonal to the laser pulses show a higher density than those that are nearly parallel [11], a useful property for differentiating orthogonal from parallel elements. However, in the current work the accumulative number of points in every pillar was discarded and not included as a feature for detecting vertical elements. This is because the number of points that represent an urban element depends on the relative position of every element in relation to the MLS sensor and on the laser scanner properties. The same urban furniture located at both sides of the street does not have the same number of points in the 3D dataset even though they correspond to the same type of element. The closer an element is to the sensor, the more points represent it in the point cloud. Incorporating the point accumulation as a descriptor in an automatic detection procedure may cause errors in the process due to the different behavior of the elements shown in the point cloud.

To determine the relationship between the RX values and the features, the correlation between these variables was studied (Table 2). The RX values and height differences had a high positive correlation (0.72); meanwhile, the RX and both dispersions presented a negative correlation (−0.44 for σ_x and −0.57 for σ_y). The pillars with a ΔH higher than the average and dispersions (σ_x and σ_y) lower than the average have higher RX values. In Table 1, the mean value of the features (ΔH , σ_x , σ_y) in three RX percentiles (P90, P95, and P99) are shown. As the correlation study suggested, the higher the RX values, the higher the ΔH and the lower the σ_x and σ_y . The pillars included in the RX 99th percentile are considered vertical urban elements since they perform a behavior similar to that of vertical elements' ground truth.

Table 1. Behavior of horizontal surfaces and pole-like elements in the considered features and average values among the full set of pillars and in percentiles 90, 95, and 99 of RX values.

	ΔH (m)	σ_x (m)	σ_y (m)
Ground Truth Horizontal surfaces	0.044	0.141	0.140
Ground Truth Vertical elements	2.78	0.103	0.098
Full pillars average	0.151	0.136	0.134
P ₉₀	1.16	0.129	0.114
P ₉₅	1.64	0.121	0.103
P ₉₉	2.96	0.106	0.102

Table 2. Correlation matrix between RX and considered geometric features.

	ΔH	σ_x	σ_y
RX	0.72	-0.44	-0.57

2.3. Pole-Like Elements Classification

Once the vertical pole-like elements are extracted they are classified into two categories: man-made poles and trees. In this step each detected vertical element is isolated from the rest and treated as an independent set of points. The correct selection of descriptors is a key point to obtain good results in the classification procedure. In our case three descriptors for vertical element were computed: the roughness of their points (both mean and dispersion values) and the scattering of radial distance (ρ) of the cylindrical coordinate frame centered in the studied pole-like set of points.

Cylindrical coordinates: After the reference frame transformation performed in the preprocessing step, the point cloud is referred to a local coordinate system. In the current step a new reference frame transformation is performed for every detected pole, moving from the Cartesian local reference frame (x,y,z) to a cylindrical coordinate system (ρ, ϕ, z). For every detected pole-like object its own cylindrical coordinate frame system is established. Its cylindrical axis coincides with the direction of Z-axis in the local coordinate system and it is located in the (x,y) centroid of the set of the points that belong to the pole-like object. From the cylindrical triplet of coordinates, the most interesting feature to accomplish this classification is the radial distance (ρ_P). This is because points that belong to man-made poles are closely located around the vertical cylindrical axis than those that represent trees due to their thin appearance. Thus, the dispersion of ρ_P in these elements is lower than in trees.

Roughness: It has been observed that both mean and standard deviation of roughness have a different behavior in each category, being their values significantly differ in both types of pole objects. Roughness values of artificial poles are lower than trees due to their flat and smooth shape on their upper part, contrary to the irregular and rough appearance of treetops, which cause higher values on these descriptors. Additionally, dispersion of this parameter in poles is lower than in trees due to the heterogeneity caused by branches and treetops

In order to test whether the geometric descriptors taken into account are distinguishable and present a distinctive behavior in the two considered classes, a separability study has been carried out. To achieve this inspection a ground truth has been generated by identifying diverse elements of both categories in the point cloud. There are several methods to measure the separability between variables; in this work Jeffries-Matusita (JM) distance and transformed divergence, computed from Bhattacharyya distance (BD) (3) has been used as separability measure [41]. In Equation (3), (μ_a, μ_b) and (σ_a, σ_b) are, respectively, the mean and standard deviation of classes a and b. JM distance (4) takes values in the range [0,2]. The higher JM values, the higher the separability between the studied classes. As can be seen in Table 3, differences between man-made poles and trees are considerably higher in the three examined variables, taken values around 1.5 and 1.8 for mean and dispersion roughness respectively, and above 1.5 in the radial distance. According with the given separability values, it is expected to obtain accurate results by the clustering algorithm in the classification of man-made poles and trees.

$$BD = \frac{1}{8} \times (\mu_a - \mu_b)^2 \times \frac{2}{(\sigma_a^2 + \sigma_b^2)} + \frac{1}{2} \times \log\left(\frac{\sigma_a^2 + \sigma_b^2}{2 \times \sigma_a \times \sigma_b}\right) \quad (3)$$

$$JM = 2 \times (1 - e^{-BD}) \quad (4)$$

Table 3. Jeffries-Matusita distances for man-made poles and trees in the considered descriptors: mean and standard deviation of roughness (μ_r and σ_r) and standard deviation of ρ (σ_ρ).

Test Case	μ_r poles-trees	σ_r poles-trees	σ_ρ poles-trees
Dataset A	1.51	1.76	1.72
Dataset B	1.52	1.88	1.53

3. Test Cases

The efficiency of the proposed method was tested in two datasets measured by different MLS sensors. In every test site the detection and classification procedure have been performed in order to test the capability of the proposed method to extract and classify pole-like objects.

3.1. Mapping Data

3.1.1. Dataset A

The point cloud used as test site 1 represents a 300 m section of an urban street in Boadilla del Monte, a city in western Madrid, Spain. This street is a type of a wide boulevard, with two lanes for each direction, the tracks of a tram in the median strip, and sidewalks and parking areas on both sides of the street. Features such as trees, shrubbery, traffic lights, lampposts, containers, bus shelters, pedestrians, or vehicles are present in this scene. This dataset was selected to test the method in areas of the city with wide streets and a great variety of vertical elements. The slope, 5% on average in this street section, also affected the selection of this test site. This dataset comprises more than 3 million points and was acquired with the IP-S2 Compact + system produced by Topcon Inc. The IP-S2 incorporates a dual frequency GNSS receiver, an IMU, and a connection to external wheel encoders, which receive odometry information. These three systems provide a highly-accurate 3D position for the vehicle. The IP-S2 Compact + scanner is equipped with five laser scanners that collect 150,000 points per second at a range of 40 m, with a vertical field of view of 360°. It is also equipped with a panoramic camera that delivers 360° spherical imagery.

3.1.2. Dataset B

A dataset corresponding to test site 2 was measured by a Lynx Mobile Mapper system, produced by Optech Inc. The Lynx scanner collects survey-grade LIDAR data at 500,000 measurements per second with a 360° field of view (FOV). The Lynx also incorporates the POS LV 520, by Applanix, which integrates an IMU with a two-antenna heading measurement system. LIDAR sensors are located in the rear of a van. Each sensor registers points in a plane at 60° to the horizontal and 45° to the longitudinal axis of the driving direction. This laser scanner provides absolute accuracies of 0.015° in heading, 0.005° in roll and pitch, 0.02 m in the X, Y positions, and 0.05 m in the Z position. All values are determined

via differential GPS post-processing after data collection using GPS base station data [42]. In this case, the point cloud was composed of more than 6 million points, and the measurements were made along a 400-m-long street in Busto Arsizio, in the Lombardy region, in northern Italy. The street is narrow, and there is one lane in each direction and sidewalks, parking areas, and buildings on both sides of the road. Furthermore, there is a double barrier of leafy tall trees on both sides of the road that causes occlusions in urban furniture, such as lampposts or traffic signs present in this test site. This site was chosen to test the efficiency of the method in narrow streets covered by dense woody vegetation.

3.2. Reference Data

A ground truth was created in each of the two datasets in order to evaluate the results provided by the detection and classification procedures. The target elements included in the detection ground truth database are those with a pole-like shape, among which are lampposts, traffic signs, traffic lights, and trees. In the classification reference data, pole-like objects are sorted into two categories: man-made poles and trees. The reference datasets were composed of all the pole-like elements that were identifiable in the original point cloud. Ground truth in Dataset A is composed of 241 pole-like objects; 141 were man-made poles and 100 were trees. In Dataset B, a total of 228 pole-like elements were observed; 56 were trees and 172 artificial poles.

The validity of our model was quantified by means of completeness, correctness and quality quantifiers, which follow Equations (5)–(7), respectively [43]. TP (true positive) are the detected poles that matched the reference, FP (false positive) represents the detected poles that do not match the ground truth, and FN (false negative) symbolize the poles that exist in the ground truth but are not detected by the proposed method.

$$\text{Completeness} = \frac{\text{poles matched the reference}}{\text{poles of reference}} = \frac{TP}{TP + FN} \quad (5)$$

$$\text{Correctness} = \frac{\text{poles matched reference}}{\text{extracted poles}} = \frac{TP}{TP + FP} \quad (6)$$

$$\text{Quality} = \frac{\text{poles matched the reference}}{\text{extracted poles} + \text{unmatched reference}} = \frac{TP}{TP + FP + FN} \quad (7)$$

To quantify the results of the classification step, the classification ground truth was compared with the labeled point cloud provided by the clustering algorithm. For every test site, a confusion matrix was constructed from which five parameters well-known in the evaluation of classification procedures are extracted: overall accuracy, commission and omission errors, and user and producer accuracy [44].

3.3. Algorithm Settings

One of the main purposes of this work was to develop automated extraction and classification procedures, which minimize user interaction. To achieve this goal, the variables and the parameters must be robust enough to be independent of the attributes of the point cloud and the configuration of the study street. We determined that the critical parameters are (i) thresholds in the geometric index to extract vertical and horizontal surfaces, (ii) the settings of the connected components segmentation, and (iii) the percentile of RX values that represent pole-like objects. The sensibility of each parameter has been

analyzed in order to establish the range of values that every parameter can take without affecting the final result of the procedure (Table 4). Regarding RX percentile, which is the parameter that determines the pole-like objects detection, its influence in the extraction has been studied and quantified for different percentile values in order to determine the optimal ones. It has been concluded that RX percentile values that provide the best quality rates are $P_{98.5}$ and P_{99} (Table 5).

In the current work, the GI thresholds were set from the studies summarized in Figure 1, in which the vertical surfaces (façades) were detected for $\alpha_V > 0.8$ and horizontal elements (pavement and sidewalks) were located when $\alpha_H > -0.8$. Thus, the vertical and horizontal surfaces were set to $GI_V > 0.8$ and $GI_H < -0.8$, respectively. Regarding the 3D connected components segmentation, the MINP was set to 2000 points/region. For the octree level (OL), in the cases the mean distance between points was almost 4 cm, which implies an OL of 20 cm. Other parameters, such as pillar size and RX, are less dependent on the characteristics of the cloud and had similar values in every case because they refer to the properties of pole-like urban elements. For the test sites used in this work, the pillar size was established at 50×50 cm, and the RX percentile was fixed at P_{99} . The same settings were applied to both test sites (Table 4).

Table 4. Algorithm settings used in the test sites A and B and range of values that every parameter can take.

	Algorithm Settings	Parameter Ranges
Vertical surfaces threshold (α_V)	0.8	[0.75; 0.85]
Horizontal surfaces threshold (α_H)	-0.8	[-0.9; -0.7]
Minimum number of points (MINP)	2000 points	[2000; 3000]
Octree level (OL)	20 cm	[15cm ; 25cm]
Pillar size	0.5m	[0.4m; 0.6m]
RX Percentile	P_{99}	[$P_{98.5}$; P_{99}]

4. Results

4.1. Dataset A

In the point cloud corresponding to this dataset, 241 pole-like elements have been observed among trees, lampposts, traffic signs, traffic posts, and tram posts. The detection procedure extracts 233 vertical elements (Figure 6a), of which 230 match with the ground truth reference and the three remaining detected poles correspond with a working vehicle that has a similar structure to the pole-like objects (Figure 7e). Consequently, eleven poles were undetected, nine of them due to their position in occluded or shadowed regions of the point cloud (Figure 7c). The two others non-detected poles are traffic signs of low height included in the reference dataset, but not high enough to be extracted by the method (Figure 7a,b). According with these results, the detection step takes completeness, correctness, and quality rates of 95.4%, 98.7%, and 94.3%, respectively (Table 5).

Regarding the classification procedure, 217 out of 230 vertical elements were correctly labeled (Figure 6b), which means an overall accuracy of 94.35% (Table 6). About trees category, 85 trees were correctly labeled and eight were wrongly classified as artificial poles due to their scarce and sparse vegetation, similar to that of a man-made pole (Figure 7i). In terms of producer's and user's accuracy, 91.4% and 94.44% are obtained in trees category with commission and omission errors of 5.56% and

8.6%, respectively. In relation to poles, five of 137 man-made poles included in the ground truth reference were incorrectly labeled. These poles are close to trees and their branches modify the appearance of the artificial poles, providing a scattered shape more characteristic of trees than of its own nature (Figure 7f,g). This classification results in a commission and omission errors of 5.71% and 3.65%, being the producer's and user's accuracy achieved 96.35% and 94.29%, respectively (Table 6). In an overall evaluation of detection and classification procedures, 217 pole-like objects out of 241 were correctly detected and classified, which means an accuracy of 90.04% (Table 7).

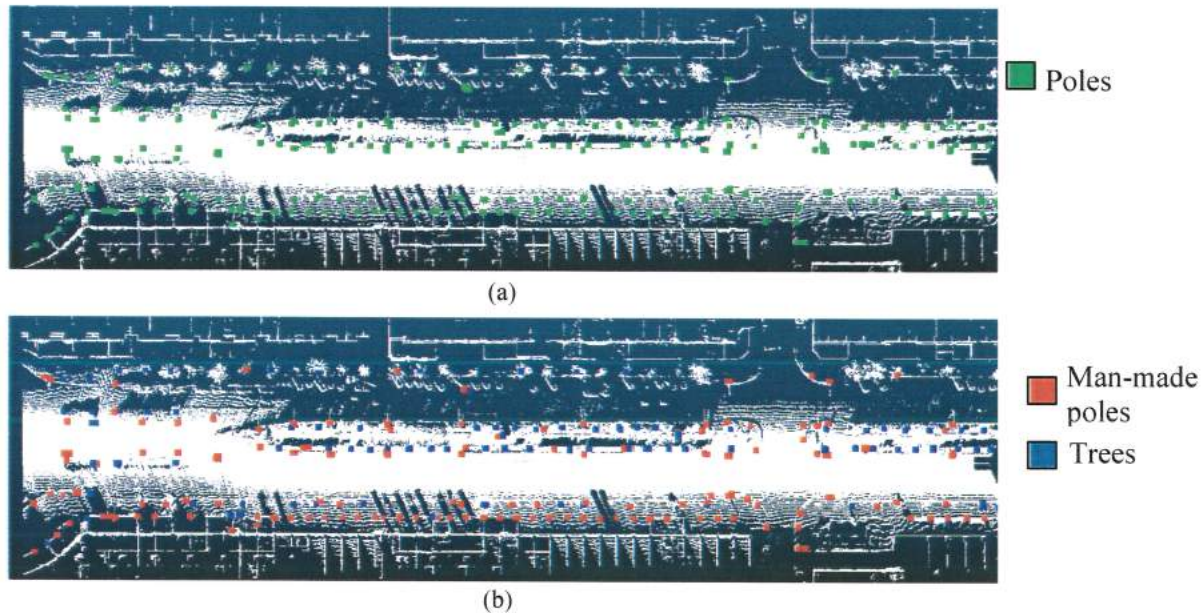


Figure 6. Results for the detection (a) and classification (b) procedure in Test Site 2.

Table 5. Completeness, correctness and quality achieved with the proposed detection method in the two studied test sites with different RX percentile values.

Test Site A/ RX Percentile	Observed	Detected	FP	FN	TP	Completeness	Correctness	Quality
97.5	241	347	111	5	236	97.93	68.01	67.05
98	241	314	78	5	236	97.93	75.16	73.98
98.5	241	252	17	6	235	97.51	93.25	91.09
99	241	233	3	11	230	95.4	98.7	94.3
99.5	241	144	2	99	142	58.92	98.61	58.44
Test Site B/ RX Percentile	Observed	Detected	FP	FN	TP	Completeness	Correctness	Quality
97.5	228	359	136	5	223	97.81	60.43	61.26
98	228	314	91	5	223	97.81	68.83	69.91
98.5	228	244	21	5	223	97.81	91.39	89.56
99	228	222	2	8	220	96.5	99.1	95.7
99.5	228	119	1	110	118	51.75	99.16	51.53

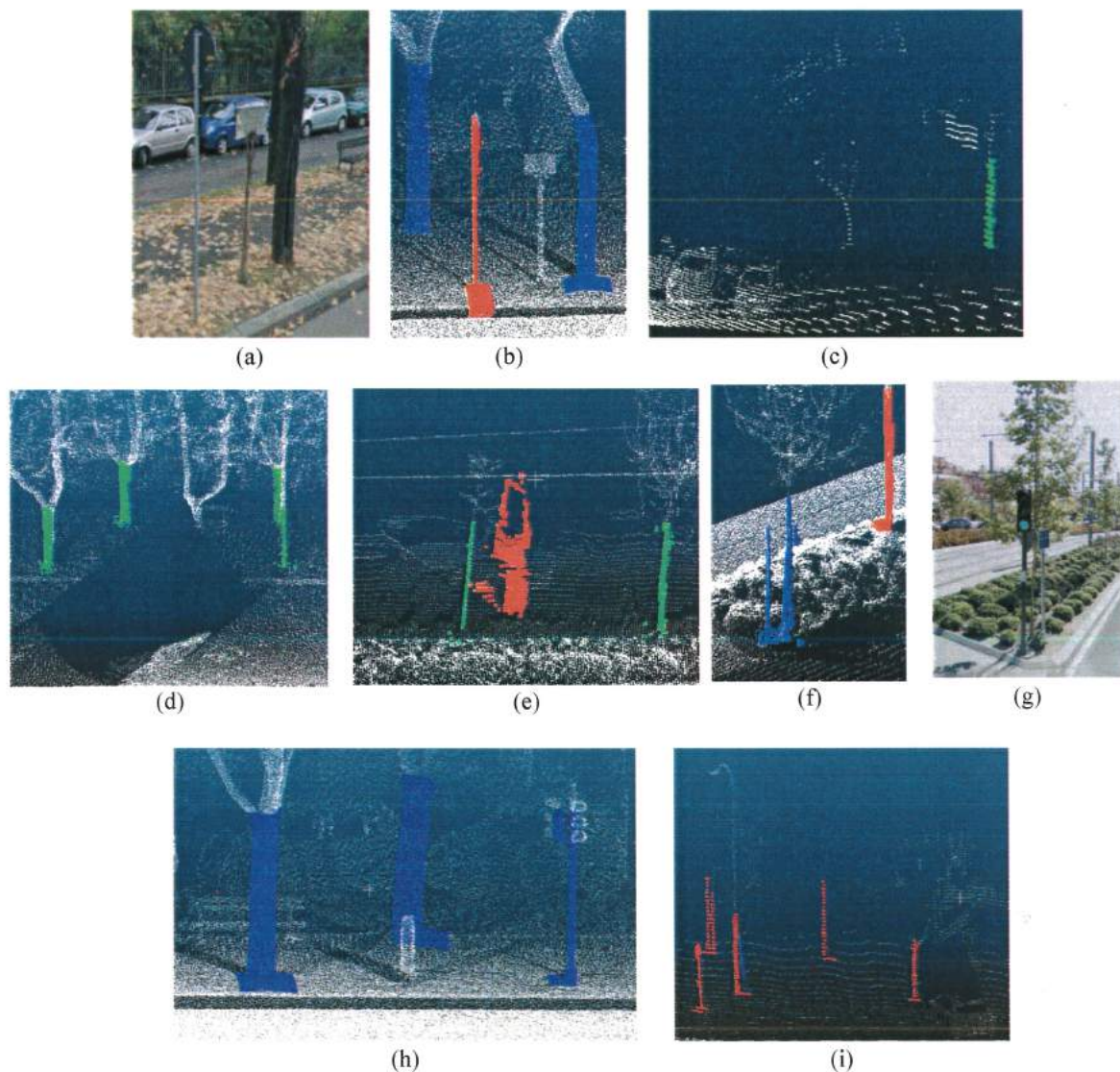


Figure 7. (a,b) little signals appearance in a RGB image and in the point cloud, (c,d) occlusion of a tree trunk, (e) in red, features detected in a work vehicle, (f,g) man-made pole surrounded by tree branches in a RGB image and in the point cloud, (h) rough and scattered man-made traffic light wrongly classified as a tree, and (i) tree with scarce and sparse vegetation misclassified as a man-made pole.

Table 6. Confusion matrix of the classification procedure in test site A, where columns are the ground truth and rows represent the classification results.

Dataset A	Trees	Poles	Σ
Trees	85	5	90
Poles	8	132	140
Σ	93	137	230
Overall Accuracy = 94.35% (217/230)			

Table 6. Cont.

Dataset A	Commission	Omission
Trees	5.56% (5/90)	8.6% (8/93)
Poles	5.71% (8/140)	3.65% (5/137)
Producer's Accuracy		User's Accuracy
Trees	91.4% (85/93)	94.44% (85/90)
Poles	96.35% (132/137)	94.29% (132/140)

Table 7. Quality evaluation complete procedure in Dataset A and B.

	Observed	Detected	FP	Undetected	Correctly Labeled	Wrongly Labeled	Accuracy
Test site A	241	233	3	11	217	13	90.04 (217/241)
Test site B	228	222	2	8	209	11	91.67 (209/228)

4.2. Dataset B

In this street section, 228 vertical elements were observed of which 220 were correctly extracted, eight were undetected, and two were falsely detected. Thus, the completeness of the detection procedure was higher than 96%, the correctness above 99%, and the quality higher than 95% (Figure 8a,b and Table 5). Regarding the eight false negatives, the undetected elements, seven were discarded by the method because they were a special kind of traffic sign, with a lower height than ordinary signs (Figure 7a,b). The remaining missing pole element corresponded to a tree trunk, which was partially occluded in the point cloud by a parked van (Figure 7d). The two false positives were detected from the structure of a van that had a shape similar to pole-like objects, with high height differences and low dispersion in (x,y) coordinates. The number of non-target pole-like elements detected would have increased, especially inside the footprint of buildings, unless the original point cloud reduction step had not been carried out. In relation to the classification step, in this road section the overall accuracy rate was 95.0%, which means that 209 out of 220 vertical elements were correctly labeled (Figure 8c,d). According to Table 8, ten man-made poles were mistakenly labeled as trees. Six of these poles were surrounded by branches of nearby trees, which caused the scattered and rough appearance of their pole in the cloud. The remaining four poles were low traffic lights, which were misclassified due to the roughness generated by their upper light structure (Figure 7h). Only one tree was wrongly classified as an artificial pole. The shape of this tree was similar to a pole, with a thin, tall trunk and barely scattered branches. These results provide a commission and omission rate of 6.02% and 0.63% in the trees and 1.85% and 15.87%, respectively, in the man-made poles category. For accuracy, tree classification achieved a producer accuracy of 99.36% and a user accuracy of 93.98%; meanwhile, the pole labeling was 84.13% and 98.15% in the producer and user accuracy, respectively (Table 8). Thus, 209 vertical elements out of 228 were correctly detected and labeled, which meant a global accuracy of 91.67% of the complete procedure (Table 7).

Table 8. Confusion matrix of the classification procedure in Dataset B, where columns are the ground truth and rows represent the classification results.

Dataset B	Trees	Poles	Σ
Trees	156	10	166
Poles	1	53	54
Σ	157	63	220
Overall Accuracy = 95.0% (209/220)			
Dataset B	Commission	Omission	
Trees	6.02% (10/166)	0.63% (1/157)	
Poles	1.85% (1/54)	15.87% (10/63)	
	Producer's Accuracy	User's Accuracy	
Trees	99.36% (156/157)	93.98% (156/166)	
Poles	84.13% (53/63)	98.15% (53/54)	

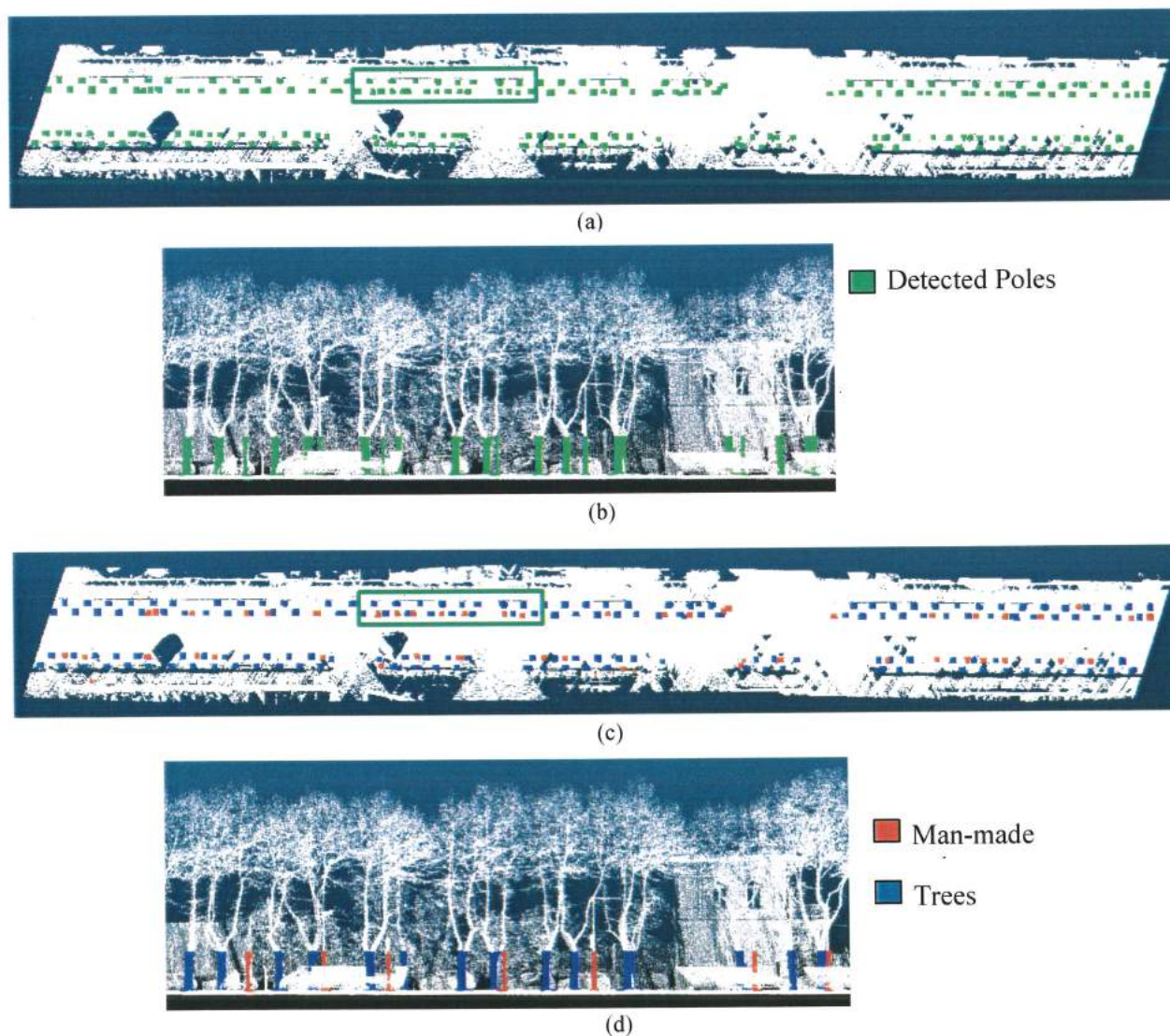


Figure 8. A zenithal and perspective view of the detection (a,b) and classification (c,d) results achieved with the proposed method in dataset B.

4.3. Comparison with Previous Methods

The results provided by our method were compared with other algorithms to evaluate its performance. In the current literature, several methods focus on extracting urban objects. In [15] the target elements were lampposts; trees were the main category in [27], and [23] extracted all types of pole-like objects without differentiating between different types. The lack of a common dataset with a ground truth associated means that every work uses its own dataset and creates a ground truth with visual inspections of the field and the point cloud. In [23] a method for extracting pole-like objects is presented that achieves a completeness detection rate average of 92.3% and a correctness of 83.8% in the four datasets. Most false positives obtained by this method are detected inside the footprint of buildings. The method developed by [30] achieved completeness and correctness rates of 77.7% and 81.0%, respectively, for targets closer than 30 m to the scanner route, which means a mean accuracy of 79.3%. Only when targets closer than 12.5 m were considered, these rates increased, achieving 83.5% and 86.5% for completeness and correctness, respectively, and a mean accuracy of 85%. Most failures in the remotest parts of the clouds were due to shadowed areas and low point density in these areas. [32] extracted lampposts in six datasets achieving completeness rates above 99% and correctness between 97.55% and 99.01; the quality index ranged from 96.74% to 98.21%. Despite the high accuracy, this method seems to be far from automated due to the large number of thresholds to be set to conduct the extraction. Individual street trees were extracted in [29] and accuracy rates above 98% were achieved. This method presents some limitations because it is designed to be used in flat terrains, and all trees must be the same height from the ground. Furthermore, this method achieves accurate results in individual street trees, but its effectiveness in dense vegetated areas where treetops are merged has not been tested. In [26], the accuracy in pole-like objects recognition was 63.9%, and in [31] the completeness and correctness achieved in detecting individual trees ranged from 80.7% to 81.2% and from 70.2% to 75.5%, respectively.

The pole-like object detection method proposed in this paper achieved quality rates in the two datasets of 94.3% and 95.7%, respectively, which are slightly higher than some of the previous methods. The two datasets used to test this method were measured by different sensors in diverse scenarios, which prove its robustness. This algorithm is independent of the scanning geometry and of the slope of the street because the coordinates are transformed in the preprocessing step. In addition, this process detects the horizontal and vertical surfaces in the point cloud and automatically delimits the regions of interest, thus avoiding false positives inside the footprints of buildings. Furthermore, this process does not require *a priori* information or previous training, and the number of thresholds has been minimized in order to automate the procedure. However, certain problems may occur in remote areas of the cloud with low point density and in trees whose trunks appear tilted. A previous work [30] proposed the development of methods for separating tree trunks from other poles. In the current work, trees and man-made poles were distinguished with a clustering algorithm. This classification procedure achieved an overall accuracy higher than 90% in every data case.

5. Conclusions and Future Works

The main novelties of the present work are: (i) the development of a geometric index that extracts horizontal and vertical surfaces and can also be used to reconstruct the MLS vehicle trajectory, (ii) the

detection of pole-like objects by means of an anomaly detection algorithm and their classification in trees and man-made elements without prior training data, and (iii) the definition of a robust procedure that can be easily automated and provides accurate results with minimal user intervention.

The pole-like object detection method proposed in this paper achieved quality rates in the two datasets of 94.3% and 95.7%, respectively, which are slightly higher than other methods. The two datasets used to test this method were measured by different sensors in diverse scenarios, which prove its robustness. This algorithm is independent of the scanning geometry and of the slope of the street because the coordinates are transformed in the preprocessing step. In addition, this process detects the horizontal and vertical surfaces in the point cloud and automatically delimits the regions of interest, thus avoiding false positives inside the footprints of buildings. Furthermore, this process does not require *a priori* information or previous training, and the number of thresholds has been minimized in order to automate the procedure. However, certain problems may occur in remote areas of the cloud with low point density and in trees whose trunks appear tilted.

The typology and casuistry of urban pole-like objects are very diverse, and there is probably no single best method for detecting and classifying them in all cases. According to the results in this work, we can conclude that this method is robust, useful for automatically detecting and classifying pole-like objects, and provides satisfactory results regardless the heterogeneity of the area and the specifications of the sensor and does not need the knowledge of the measured MLS trajectory. In the future, other anomaly detection algorithms could be tested in the detection step, and other features such as laser intensity could be introduced in the classification procedure to expand the classification to other types of urban elements. The detecting procedure provided quality values of around 95% in two test sites, and the classification step achieved an overall accuracy above 94%. In an overall evaluation of both procedures, more than 90% of the vertical elements were correctly detected and classified.

Acknowledgments

The authors would like to thank the Optech Inc. and TOPCON Inc. for providing the datasets to test the proposed method.

Author Contributions

The authors, Borja Rodríguez-Cuenca, Silverio García-Cortés, Celestino Ordóñez and María C. Alonso, designed the research, performed data analysis, and contributed with ideas, writing and discussion.

Conflicts of Interest

The authors declare no conflict of interest.

References and Notes

1. Mundia, C.; Aniya, M. Analysis of land use/cover changes and urban expansion of Nairobi city using remote sensing and GIS. *Int. J. Remote Sens.* **2005**, *26*, 2831–2849.
2. Dimitrakopoulos, G.; Demestichas, P. Intelligent transportation systems. *IEEE Veh. Technol. Mag.* **2010**, *5*, 77–84.

3. Levinson, J.; Askeland, J.; Becker, J.; Dolson, J.; Held, D.; Kammel, S.; Kolter, J.Z.; Langer, D.; Pink, O.; Pratt, V. Towards fully autonomous driving: Systems and algorithms. In Proceedings of IEEE Intelligent Vehicles Symposium (IV), Baden-Baden, Germany, 5–9 June 2011; pp 163–168.
4. Jiang, X.; Bunke, H. Fast segmentation of range images into planar regions by scan line grouping. *Machine Vis. Appl.* **1994**, *7*, 115–122.
5. Hyypä, J.; Jaakkola, A.; Chen, Y.; Kukko, A. Unconventional LiDAR mapping from air, terrestrial and mobile. In Proceedings of the Photogrammetric Week, Stuttgart, Germany, 9–13 September 2013; pp 205–214.
6. Zogg, H.; Ingensand, H. Terrestrial laser scanning for deformation monitoring—Load tests on the Felsenau Viaduct (CH). *Int. Arch. Photogramm. Remote Sens.* **2008**, *37*, 555–562.
7. Rüther, H.; Held, C.; Bhurtha, R.; Schröder, R.; Wessels, S. Challenges in heritage documentation with terrestrial laser scanning. In Proceedings of the 1st AfricaGEO Conference, Capetown, South Africa, 30 May–2 June 2011.
8. Zhu, L.; Hyypä, J. The use of airborne and mobile laser scanning for modeling railway environments in 3D. *Remote Sens.* **2014**, *6*, 3075–3100.
9. Vosselman, G.; Gorte, B.G.; Sithole, G.; Rabbani, T. Recognising structure in laser scanner point clouds. *Int. Arch. Photogramm. Remote Sens. Spat. Inf. Sci.* **2004**, *46*, 33–38.
10. Douillard, B.; Underwood, J.; Kuntz, N.; Vlaskine, V.; Quadros, A.; Morton, P.; Frenkel, A. On the segmentation of 3D LiDAR point clouds. In Proceedings of IEEE International Conference on Robotics and Automation (ICRA), Shanghai, China, 9–13 May 2011; pp 2798–2805.
11. Yang, B.; Fang, L.; Li, J. Semi-automated extraction and delineation of 3D roads of street scene from mobile laser scanning point clouds. *ISPRS J. Photogramm. Remote Sens.* **2013**, *79*, 80–93.
12. Rodríguez-Cuenca, B.; García-Cortés, S.; Ordóñez, C.; Alonso, M.C. An approach to detect and delineate street curbs from MLS 3D point cloud data. *Autom. Constr.* **2015**, *51*, 103–112.
13. Jaakkola, A.; Hyypä, J.; Kukko, A.; Yu, X.; Kaartinen, H.; Lehtomäki, M.; Lin, Y. A low-cost multi-sensoral mobile mapping system and its feasibility for tree measurements. *ISPRS J. Photogramm. Remote Sens.* **2010**, *65*, 514–522.
14. Lehtomäki, M.; Jaakkola, A.; Hyypä, J.; Kukko, A.; Kaartinen, H. Performance analysis of a pole and tree trunk detection method for mobile laser scanning data. *Int. Arch. Photogramm. Remote Sens. Spat. Inf. Sci.* **2011**, *38*, 197–202.
15. Yujie, H.; Xiang, L.; Jun, X.; Lei, G. A novel approach to extracting street lamps from vehicle-borne laser data. In Proceedings of 19th International Conference on Geoinformatics, Shanghai, China, 24–26 June 2011; pp 1–6.
16. Rabbani, T.; van den Heuvel, F.; Vosselmann, G. Segmentation of point clouds using smoothness constraint. *Int. Arch. Photogramm. Remote Sens. Spat. Inf. Sci.* **2006**, *36*, 248–253.
17. Golovinskiy, A.; Funkhouser, T. Min-cut based segmentation of point clouds. In Proceedings of IEEE 12th International Conference on Computer Vision Workshops (ICCV Workshops), Kyoto, Japan, 27 September–4 October 2009; pp 39–46.
18. Belton, D.; Lichti, D.D. Classification and segmentation of terrestrial laser scanner point clouds using local variance information. In Proceedings of ISPRS Commission V Symposium: Image Engineering and Vision Metrology (IAPRS), Dresden, Germany, 25–27 September 2006.

19. Verma, V.; Kumar, R.; Hsu, S. 3D building detection and modeling from aerial LiDAR data. In Proceedings of IEEE Computer Society Conference on Computer Vision and Pattern Recognition, New York, USA, 17–22 June 2006; pp 2213–2220.
20. City of Melbourne Street Furniture Plan. Available online: <http://www.melbourne.vic.gov.au/> (accessed on 22 June 2015).
21. Rabbani, T.; Van Den Heuvel, F. Efficient hough transform for automatic detection of cylinders in point clouds. In Proceedings of ISPRS Workshop: Laser Scanning 2005, Enschede, The Netherlands, 12–14 September 2005; pp. 60–65.
22. Schnabel, R.; Wahl, R.; Klein, R. Efficient RANSAC for point-cloud shape detection. *Comput. Graph. Forum* **2007**, *26*, 214–226.
23. Cabo, C.; Ordoñez, C.; García-Cortés, S.; Martínez, J. An algorithm for automatic detection of pole-like street furniture objects from mobile laser scanner point clouds. *ISPRS J. Photogramm. Remote Sens.* **2014**, *87*, 47–56.
24. Brenner, C. Extraction of features from mobile laser scanning data for future driver assistance systems. In *Advances in Giscience*; Springer: Berlin/Heidelberg, Germany, 2009; pp 25–42.
25. El-Halawany, S.I.; Lichti, D.D. Detection of road poles from mobile terrestrial laser scanner point cloud. In Proceedings of International Workshop on Multi-Platform/Multi-Sensor Remote Sensing and Mapping (M2RSM), Xiamen, China, 10–12 January 2011; pp 1–6.
26. Yokoyama, H.; Date, H.; Kanai, S.; Takeda, H. Pole-like objects recognition from mobile laser scanning data using smoothing and principal component analysis. *Int. Arch. Photogramm. Remote Sens. Spat. Inf. Sci.* **2011**, *38*, pp. 115–120.
27. Rutzinger, M.; Pratihast, A.; Oude Elberink, S.; Vosselman, G. Detection and modelling of 3D trees from mobile laser scanning data. *Int. Arch. Photogramm. Remote Sens. Spat. Inf. Sci.* **2010**, *38*, 520–525.
28. Li, D.; Elberink, S.O. Optimizing detection of road furniture (pole-like objects) in mobile laser scanner data. *ISPRS Ann. Photogramm. Remote Sens. Spat. Inf. Sci.* **2013**, *1*, 163–168.
29. Wu, B.; Yu, B.; Yue, W.; Shu, S.; Tan, W.; Hu, C.; Huang, Y.; Wu, J.; Liu, H. A voxel-based method for automated identification and morphological parameters estimation of individual street trees from mobile laser scanning data. *Remote Sens.* **2013**, *5*, 584–611.
30. Lehtomäki, M.; Jaakkola, A.; Hyypä, J.; Kukko, A.; Kaartinen, H. Detection of vertical pole-like objects in a road environment using vehicle-based laser scanning data. *Remote Sens.* **2010**, *2*, 641–664.
31. Yao, W.; Fan, H. Automated detection of 3D individual trees along urban road corridors by mobile laser scanning systems. In Proceedings of International Symposium on Mobile Mapping Technology (MMT), Tainan City, Taiwan, 1–3 May 2013.
32. Yu, Y.; Li, J.; Guan, H.; Wang, C.; Yu, J. Semiautomated extraction of street light poles from mobile lidar point-clouds. *IEEE Trans. Geosci. Remote Sens.* **2015**, *53*, 1374–1386.
33. Ioannou, Y.; Taati, B.; Harrap, R.; Greenspan, M. Difference of normals as a multi-scale operator in unorganized point clouds. In Proceedings of 2nd International Conference on 3D Imaging, Modeling, Processing, Visualization and Transmission (3DIMPVT), Zurich, Switzerland, 13–15 October 2012; pp 501–508.

34. Di Stefano, L.; Bulgarelli, A. A simple and efficient connected components labeling algorithm. In Proceedings of International Conference on Image Analysis and Processing, Venice, Italy, 27–29 September 1999; pp. 322–327.
35. Anagnostopoulos, C.N.E.; Anagnostopoulos, I.E.; Loumos, V.; Kayafas, E. A license plate-recognition algorithm for intelligent transportation system applications. *IEEE Trans. Intell. Transp. Syst.* **2006**, *7*, 377–392.
36. Hu, H.; Munoz, D.; Bagnell, J.A.; Hebert, M. Efficient 3-D scene analysis from streaming data. In Proceedings of IEEE International Conference on Robotics and Automation (ICRA), Karlsruhe, Germany, 6–10 May 2013.
37. Reed, I.S.; Yu, X.; Adaptive multiple-band CFAR detection of an optical pattern with unknown spectral distribution. *IEEE Trans. Acoust. Speech Signal Process.* **1990**, *38*, 1760–1770.
38. Chang, C.-I.; Chiang, S.-S. Anomaly detection and classification for hyperspectral imagery. *IEEE Trans. Geosci. Remote Sens.* **2002**, *40*, 1314–1325.
39. Alonso, M.C.; Malpica, J.A. The combination of three statistical methods for visual inspection of anomalies in hyperspectral imageries. In Proceedings of 7th International Conference on Advances in Pattern Recognition (ICAPR), Kolkata, India, 4–6 February 2009; pp. 377–380.
40. Hongchao, F.; Wei, Y.; Long, T. Identifying man-made objects along urban road corridors from mobile LiDAR data. *IEEE Geosci. Remote Sens. Lett.* **2014**, *11*, 950–954.
41. Kailath, T. The divergence and Bhattacharyya distance measures in signal selection. *IEEE Trans. Commun. Technol.* **1967**, *15*, 52–60.
42. Puente, I.; González-Jorge, H.; Riveiro, B.; Arias, P. Accuracy verification of the Lynx mobile mapper system. *Opt. Laser Technol.* **2013**, *45*, 578–586.
43. Heipke, C.; Mayer, H.; Wiedemann, C.; Jamet, O. Evaluation of automatic road extraction. *Int. Arch. Photogramm. Remote Sens.* **1997**, *32*, 151–160.
44. Jensen, J.R.; Lulla, K. *Introductory Digital Image Processing: A Remote Sensing Perspective*, 2nd ed.; Prentice-Hall: Upper Saddle River, NJ, USA, 1996.

© 2015 by the authors; licensee MDPI, Basel, Switzerland. This article is an open access article distributed under the terms and conditions of the Creative Commons Attribution license (<http://creativecommons.org/licenses/by/4.0/>).

3.2. Paper N°3: An approach to detect and delineate street curbs from MLS 3D point cloud data

3.2.1. Summary

Following the research focus of the current chapter, focused on urban entities detection from mobile laser scanner sensors, this article describes a methodology for extracting street curbs from MLS point clouds. Roadside detection is useful in several applications such as 3D urban modeling, road maintenance, and autonomous navigation system development. This method consists of a point cloud rasterization and a linear element search contained in the 2D raster through morphological operators. A mechanism has also been developed for extracting the upper and lower curb edges and estimating those invisible curbs occluded by automobiles, containers, or other obstacles in the street. The effectiveness of this method has been tested in urban areas with different settings and frameworks and in datasets recorded by sensors with different characteristics. The results were published in the scientific paper [76]. The detection method provided accuracies higher than 95% in the studied areas and correctly estimated over 96% of hidden curbs.

3.2.2. Quality Indicators

The current contribution has been published in the Automation in Construction Journal, with an impact factor of 1.812 according to a 2014 JCR evaluation. This journal is included in the top quartile of two JCR categories: Construction and Building Technology and Civil Engineering. This paper has been cited by other research works and, to date, has one reference according to WOS and SG databases. The developed method was also presented at the 2015 EGU conference [77].

Research works included in this chapter, related to urban furniture and cartographic entities extraction and classification from MLS 3D point clouds, are the fruit of the collaboration with the “GEOGRAPH: Geomatic and

Graphic Computation” research group. This group belongs to the Department of Mining Exploitation of the University of Oviedo. They have extensive experience in 3D point cloud analysis and treatment, as demonstrated by their publications in this research field [78, 79].

The main objective of the works included in this chapter is the development of methods to automatically extract information from 3D MLS point clouds and trying to minimize user intervention. Developed algorithms are a useful tool for urban furniture and vegetation inventory creation and updating in urban environments.



Contents lists available at ScienceDirect

Automation in Construction

journal homepage: www.elsevier.com/locate/autcon

An approach to detect and delineate street curbs from MLS 3D point cloud data

Borja Rodríguez-Cuenca^{a,*}, Silverio García-Cortés^b, Celestino Ordóñez^b, Maria C. Alonso^a^a Department of Physics and Mathematics, University of Alcalá, Campus Universitario Ctra. Madrid-Barcelona, km. 33,600, 28871 Alcalá de Henares, Madrid, Spain^b Department of Mining Exploitation, University of Oviedo, Escuela Politécnica de Mieres, C/Gonzalo Gutiérrez Quirós, 33600 Mieres, Asturias, Spain

ARTICLE INFO

Article history:

Received 4 June 2014

Received in revised form 9 October 2014

Accepted 11 December 2014

Available online xxxx

Keywords:

Mobile laser scanner

Curb extraction

3D point cloud

Feature extraction

Urban modeling

Segmentation

ABSTRACT

This paper is focused on the detection and delineation of curbs and street boundaries using a 3D point cloud registered by a mobile laser scanner (MLS) system. Non-manual roadside detection is an important issue in road maintenance, 3D urban modeling, and autonomous navigation fields. The proposed method is able to detect upper and lower curb edges and delineate even occluded or hidden roadsides in most environments. It is based on a rasterization and segmentation approach for curb detection while preserving the reference to the original point cloud avoiding loss of information.

The method was tested using two point clouds from various street scenes measured by an Optech Lynx Mobile Mapper System, providing accuracies in curb extraction over 95% in both datasets.

© 2014 Elsevier B.V. All rights reserved.

1. Introduction

The automatic detection of the various constructed elements in roads and streets has become the subject of research in recent years because of its practical interest. Accurate automatic detection saves a great deal of time and money during the creation and updating of cartographic databases [1]. Moreover, recently, there have been important advances in the development of autonomous driving systems. These systems require an accurate detection of road boundaries between which the autonomous vehicle [2,3] or pedestrian robot [4] must drive. Precise road boundary detection will increase autonomous driving systems safety and prevent accidents.

Several methods have been developed to detect roads based on imagery data. A thorough review can be found in [5,6]. Road extraction and classification from images have been under research for many years. The different approaches vary depending on the road model and road representation selection which, in turn, are directly related with the sensor resolution [7]. In low-resolution images, roads appear as thin lines. In these cases, detection is reduced to center road extraction. In high-resolution data, roads appear as two-dimensional areas rather than one-dimensional line. In these cases, the boundaries of roads will be detected instead the centerline [8]. In [1,6,9,10], some methodologies to extract roads from aerial and satellite images are presented. Many

other approaches focus on road detection methods from Radio Detection And Ranging (RADAR) and Light Detection And Ranging (LIDAR) data [8,11]. Detection in urban environments could be difficult due to the occlusions produced by high elements such as trees or buildings. Those elements produce errors in detecting land covers because they appear to overlap with the real land cover in the aerial images [12] and cast shadows on the ground in laser pulse datasets.

In the last decade, several laser scanner sensors have been developed. These sensors provide unstructured data in the form of point clouds with very high densities. This data open the possibilities for an automatic feature detection of cartographic entities in urban environments. Laser scanner sensors could be placed on aerial (aerial laser scanner (ALS) or aerial LIDAR) or terrestrial platforms (terrestrial laser scanner (TLS) or terrestrial LIDAR). Terrestrial LIDAR can be categorized into two types: static and dynamic. Static terrestrial LIDAR data collection is carried out from base stations: A sensor is fixed in the base station, from which the point cloud is sensed. Dynamic terrestrial LIDAR or mobile laser scanner (MLS) sensors are installed in a mobile platform. MLS sensors have a navigation system based on global navigation satellite systems (GNSS) and inertial measurement units (IMU). These devices determine the position of the mobile platform and the direction and orientation of the sensor at every moment [13]. The GNSS and IMU data are combined with measures carried out by the laser scanner sensor in order to obtain the final product: a geo-referenced point cloud [14].

Laser scanner sensors provide additional and complementary information to that provided by aerial images. TLS and MLS provide point

* Corresponding author. Tel.: +34 918 85 67 48.

E-mail address: borja.rodriguezc@edu.uah.es (B. Rodríguez-Cuenca).

clouds with a higher density than those detected with LIDAR flights (ALS), and they are useful in detecting cartographic entities in urban and rural areas. These instruments are very attractive in terms of documentation and inspection work due to the speed of data collection, their accuracy, and the fact that they do not require direct contact with the objects of interest for data collection [15].

The goal of this work is to present a new method to detect street curbs from 3D point clouds registered using a MLS sensor. These street elements are interesting for the development of autonomous driving applications and urban elements inventory purposes like pole-like elements, traffic signals, etc. This method provides a solution to this problem based on the projection of the measured point cloud on the XY plane. Over that plane, a segmentation algorithm and linear elements search is carried out in order to determine the location of street boundaries. The proposed method is valid in both straight and curved road sections. Furthermore, a solution to the problem of detecting the upper and lower edges of the curb and estimating occluded boundaries in the measured point cloud is provided. The paper is organized as follows: Section 2 summarizes the previous studies related to ours; in Section 3 the proposed method to detect street boundaries is detailed; and Section 4 shows the results obtained in two study cases, both performed in the north of Spain. Finally, our conclusions are given in Section 5.

2. Related work

Many applications for terrestrial laser scanners have been reported since the appearance of these systems. The 3D modeling of buildings, caves and indoor areas [16,17], maintaining control over soil erosion and rock fall hazards [18], the geometry verification of tunnels [19,20], the modeling and reconstruction of 3D trees [21], or the roughness soil description [22,23] are some of the applications for which TLS's have been used. Additionally, several applications for point clouds detected via MLS sensors exist in the current literature. They have been used in applications such vertical wall extraction, façade modeling, building footprint detection [24–26] and the extraction of pole-like objects, such traffic signs, lamp posts, or tree trunks [27,28].

The work presented in this paper is devoted to curb and street boundary extraction from point clouds detected by MLS sensors. In the current literature, there are some studies related to this issue. Some of them use as input data point clouds obtained from stereo vision. Recently, some authors have focused on the detection of road markings, lines, and road sides in straight and curved areas based on data obtained by stereo cameras [29,30]. Siegemund et al. [31] present a real-time method to determine and reconstruct curbs from 3D point clouds created from stereo vision or measured by a MLS. They determine the values of certain parameters about surfaces and curbs that are included in a model. Detection is carried out in an iterative procedure that involves two steps. First, the points of the 3D point cloud are assigned to curbs or adjacent surfaces; and then, surfaces and curbs are reconstructed by fitting a cubic/three-order polynomial. In [32], a robust algorithm that performs real-time lane detection and tracking based on Random Sample Consensus (RANSAC) is proposed. This algorithm works with images obtained by a camera installed on a car.

There are also some methods in the current literature to detect curbs and roadsides based on point clouds measured with TLS and MLS sensors. In [33], a method to detect curbs using 3D scanner sensor data is presented. The detection process starts with the voxelization of the point cloud and the separation of those points that represent the ground. Later, candidate points for curbs are selected based on three spatial variables: height difference, gradient value, and normal orientation. Using a short-term memory technique, every point located in a voxel whose vertical projection is in the road is considered a false positive and is deleted. Finally, the curb is detected by adjusting a parabolic model to the candidate points and performing a RANSAC algorithm to

remove false positives. The performance of the method depends on the correct selection of the thresholds for each of the three variables used. This method provides a detection rate of about 98% in two studied datasets.

Weiss and Dietmayer [34] automatically determined the position of lane markings, sidewalks, reflection posts, and guardrails by a vertically and horizontally automotive laser scanner data. Curb detection applies a third-order Gaussian filter to sharpen the vertical distance profile, which defines the shape of the curb. This profile is divided into sections with a certain width, forming an accumulative histogram. Candidate curbs are found through a histogram-based algorithm to search those slots of the histogram that are candidates to represent curbs and guardrails. Because not every candidate is a valid curb, the locations of real curbs are determined by analyzing the heights, slopes, and interruptions of every polygon.

Belton and Bae [15] proposed a method to automatize the identification of curbs and signals using a few steps. The rasterization of the 3D point cloud into a 2D grid structure allows each cell to be examined separately. The method first extracts the road; then cells which are adjacent to the road are likely to contain curbs. Points in these cells are used to determine the vertical plane of the curb, from which a 2D transversal section is calculated. The top and the bottom of the curb are determined as those points which are furthestmost above and below the line defined by the two furthestmost points in the 2D section. This procedure has several limitations. The proposed method would not provide good results detecting concave and non-horizontal roads; furthermore, the method could provide poor results for shorter or curved curbs due to confusing edges with other points of the studied profile.

Yang et al. [35] carried out an edge detection by dividing the measured point cloud into two-dimensional sections using the GPS time at which every point was registered. They applied a moving window to these 2D sections to detect the roads and road boundaries. Curbs were detected by analyzing the elevation and shape change in the moving windows studied. They also presented a method to detect curbs in occluded parts of the cloud, but some problems in areas with irregular shapes were detected. The value of the parameters and the length of the moving window are critical to the performance of the proposed method.

A recent work by Hervieu and Soheilian [36] describes a method to extract curbs and ramps, as well as reconstruct lost data in areas hidden by obstacles in the street. A system for the reconstruction of road and sidewalk surfaces is also proposed. They adjust a plane to a group of points from the cloud and compute the angular distance between the normal vector and the z vector. After that, a prediction/estimation model is applied to detect road edges. The procedure requires the user to manually select the curb direction, which is not always easy. This method could fail in curved or occluded sections. To solve this problem, they propose a semi-automatic solution in which the user must choose some points of the non-detected curb to reconstruct these sections.

In [37] Kumar et al. developed a method to detect road boundaries in both urban and rural roads, where the non-road surface is comprised of grass and soil and the edges are not as easily defined by slope changes alone. A 2D rasterization of the slope, reflectance, and pulse width of the detected point cloud is carried out. Gradient vector flow and a balloon model are combined to create a parametric active contour model, which allows the road boundaries to be determined. Roadside detection is carried out using a snake curve, which is initialized based on the navigation track of a mobile van along the road section. The snake curve moves using an iterative process until it converges on the roadsides, where the minimum energy state is located. This method has been tested in straight sections and provided good results, but its performance in curved sections is unknown. The procedure is computationally complex, which could make the detection process too slow.

There exist some solutions for curb detection in commercial software packages [38] but unfortunately the technical details could not be found in the literature. These solutions are not automatic at all; the

user must provide some initial elements to the software, especially in curved sections.

3. Method

The proposed method of detecting and delineating curbs consists of six steps. The flow chart of the procedure in Fig. 1 briefly describes every step of the method. The inputs of the process are 3D point clouds measured by the MLS sensor and vehicle trajectory points obtained from the GPS/INS systems, describing the trajectory of the vehicle. The outputs of the procedure are the points of the curbs and lines representing the curbs in occluded areas.

Every step of the proposed method is described in detail below:

3.1. Orientation and trimming

The point clouds obtained by mobile laser scanner (MLS) are properly geo-referenced in a global reference system by means of a navigation system and an IMU, which provides coordinates within a global frame to every point. In fact, the point clouds used in both study cases of this work are geo-referenced using UTM projection in Zone 29 and WGS84 ellipsoidal heights. In order to ease and speed up every operation, the original coordinate system is transformed by means of a translation and two rotations into a local Cartesian coordinate system whose origin is located at the beginning of the MLS trajectory, being the x-axis coincident with the average direction of the vehicle and the zero height plane at the height of the GNSS phase center system. It is obvious that points belonging to curbs will be placed below the new XY plane after the previous geometric transformation. Now a trimming process is carried out to reduce the point cloud size: only points with local negative z-coordinate values are kept, being removed those points located over the GPS antenna height.

3.2. Rasterization

The next step of the procedure consists of the rasterization of the point cloud to reduce its dimension and make it more manageable,

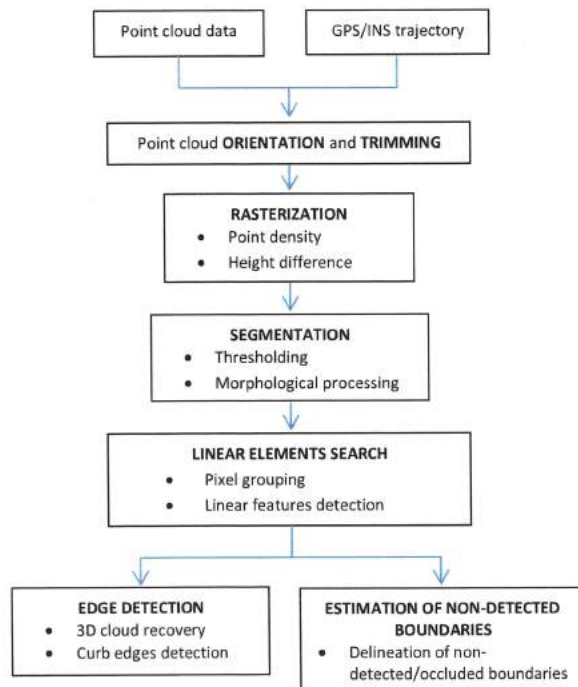


Fig. 1. Flow chart of the proposed method to detect and delineate street boundaries.

moving from a 3D cloud to a 2D raster image. Moreover, in a raster image, it is possible to apply image analysis techniques to detect those pixels that contain points that belong to a roadside.

The efficiency of the detection process will depend on the pixel size of the created image. Cell size also depends on the point density of the point cloud. The resolution of the rasterized image could grow proportionately with the point cloud's density, but these also could require more computation resources. In any case, the grid spacing must be large enough to contain a significant number of points, but small enough to allow only a small number of salient features in each cell [15]. To decide the proper size of the cell, distances between contiguous pulses on the pavement—just below the central rear point of the vehicle—were measured. These points are located at a constant distance for any dataset and have been used to compare nominal densities of different cloud points. In this study the used cell size was 5 times the distance between those contiguous pulses. We have found that this value allows a proper detection of curbs with different scan densities and curb widths. For each cell in the rasterization grid, two digital values (DV) are calculated and stored: (i) the difference between the highest and the lowest point of all points contained in the studied cell (resulting an image similar to a normalized digital surface model (nDSM) [39]) and (ii) the number of points contained in every cell. After the rasterization step two images are available: one with DV representing the height difference (referred to as nDSM from now on) and another in which each pixel's DV is the number of points contained within it (referred to as image density from now on).

3.3. Segmentation

3.3.1. Thresholding

In this stage a binary image will be created by thresholding the two former images. Common curbs show heights of few tens centimeters but they can vary depending on the country and type of street. Candidate curb pixels are chosen from the nDSM image by thresholding (Eq. (1)). The maximum and minimum thresholds will be set as the maximum curb height expected and the minimum value which allow avoiding extraction of points from the road. In Table 1 can be found the threshold values used for the test datasets.

$$H_{min} < nDSM[i, j] < H_{max} \quad (1)$$

Surfaces that are orthogonal to the laser pulses show a higher density than those that are nearly parallel to the laser pulses [28,35]. Thus, pixels that represent the vertical face of the curb must have a higher DV in the density image than those that represent a horizontal surface. A second condition was imposed on the density image: Pixels that represent a curb must have a DV in the density image that is higher than an established threshold (D_{min}) (Eq. (2)).

$$\text{Density image}[i, j] > D_{min} (\text{points/pixel}) \quad (2)$$

With these two restrictions, a new binary image is created, where candidate pixels are flagged with 1. The rest of the detection process will affect only to these pixels. There will be more pixels, in addition to those that represent curbs, which fulfill the conditions imposed, as those that represent steps of stairways, low vegetation or cars. The

Table 1

Algorithm settings used in the test sites 1 and 2.

Pixel size	5 × 5 cm
Δh (H_{min} and H_{max})	0.10 < nDSM < 0.20
Point density (D_{min})	5 points/pixel
Line width (p and q)	3 pixels < Line width < 6 pixels
Line percent (μ)	80%
Region aspect ratio (columns/rows) (m and n)	$\leq 1/3$ and ≥ 3

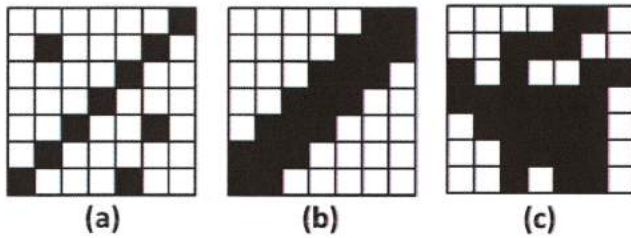


Fig. 2. (a) Synthetic image representing a linear structure and three isolated pixels, (b) Result of the morphological opening operation and (c) a nonlinear region.

following steps in the process will try to remove from the binary image those 1-value pixels which do not belong to curbs.

3.3.2. Morphological processing

A morphological opening is applied to the binary image obtained in the former step. This morphological operation is conceptually composed of two phases erosion and dilation [40]. The erosion operation will first remove those isolated pixels that do not represent a curb but satisfied the conditions established in the thresholding step. During the dilation operation, every pixel that is 4-connected with the candidate pixels of the original binary image is added to the curb candidate set of pixels being labeled with 1.

An example of the performance of the opening operation can be seen in Fig. 2. Dilation is applied to an image in which a linear structure and three isolated pixels are presented (Fig. 2(a)). The linear element represents a curb, and the isolated pixels correspond to those satisfying the rules of the thresholding step but not representing a roadside. By applying the morphological operator, this salt and pepper effect is removed and linear structure grows (Fig. 2(b)). The morphological processing removes the isolated pixels wrongly considered as candidates but not those groups of pixels that satisfy the imposed thresholds and represent other features different from curbs. These errors will be corrected in the next step through a study of the shape of the regions in the binary image.

3.4. Linear elements search

3.4.1. Pixel grouping

Those curbs that define the roadside have a linear shape different than other street elements. It is assumed that, in the binary image, pixels that represent curbs are grouped forming linear structures. Pixels that do not represent curbs are not grouped or are grouped without a particular distribution. Thus, every group of candidate pixels without a linear shape will be deleted. The linear element search starts with a grouping algorithm. Pixels with a value of 1 from the binary image that have an edge in common are grouped in a unique region. Thus, the former binary image becomes a segmented image. Every region created in this step has its own identifier.

The grouping procedure consists of an image segmentation based on a region-growing algorithm over the binary image [41].

3.4.2. Linear feature detection

In order to remove the noisy pixels, linear feature detection is carried out in every region that was created previously. A common feature of every target linear region is that its width is similar to the breadth of the real-curb line it represents. Counting the number of 1-value pixels in each column and in each row that exist in the window defined by the region, we find that most of them must have a number of pixels equal to the width of the target line. Thus, a diagonal 3 pixel width real-curb line is represented in Fig. 2(b) and (c), showing a nonlinear region, which corresponds to a wrong detected region that must be removed. Regions that represent curbs will be detected by imposing the condition that at least a certain percentage of columns or rows must have as many pixels as the width of the target line.

For each region, the number of rows and columns that have a width between p and q pixels was determined via Eqs. (3) and (4), where r and c represent the total number of rows and columns, respectively, in the studied region. Every region that has a percentage of rows or columns (rowpercent and colpercent in Eqs. (5) and (6)) with a number of pixels between the width line thresholds that are higher than a selected percentage (μ) will be considered to be a linear feature. Those regions that do not meet this requirement are discarded and not

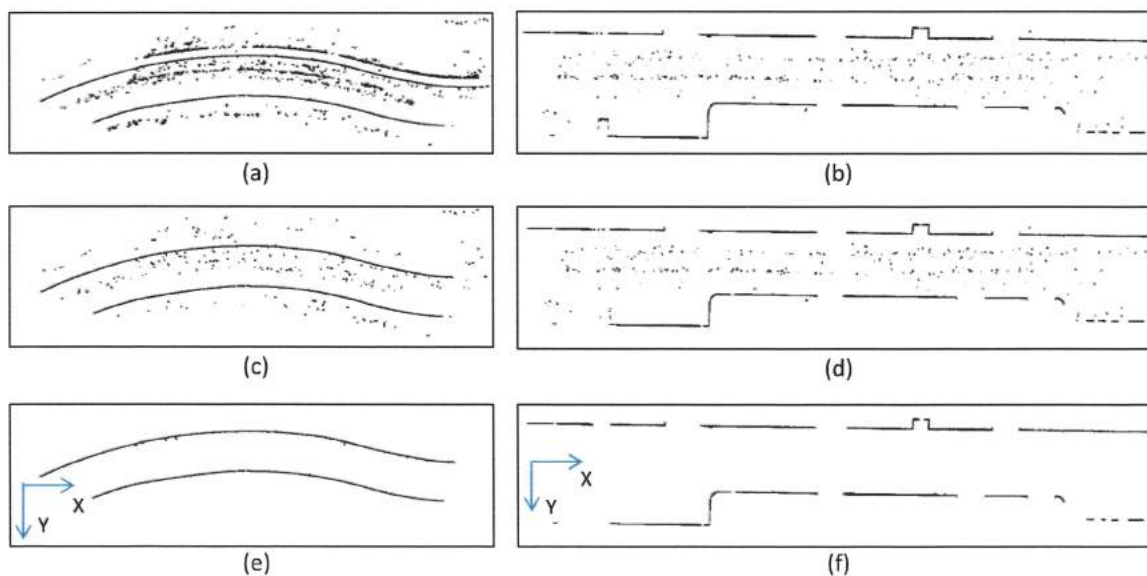


Fig. 3. Steps in the linear element detection procedure for Test Sites 1 and 2. (a) and (b) are the outputs of the threshold process, (c) and (d) are the images obtained after first step of the linear elements search, and (e) and (f) are the binary images based on curb detection.

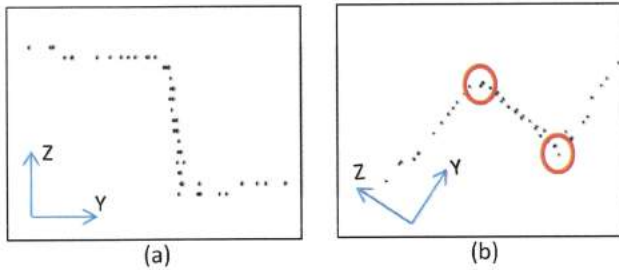


Fig. 4. (a) Profile corresponding to a curb before the rotation around the x-axis; the horizontal and vertical surfaces of the sidewalks, curbs, and roads could be easily recognized; (b) the same curb after the 45° rotation around the x-axis has been carried out; curb surfaces are now inclined at $\pm 45^\circ$. The edges correspond with points where the slope sign changes (those surrounded by red circles). (For interpretation of the references to color in this figure legend, the reader is referred to the web version of this article.)

considered to represent curbs.

$$\text{rowslines} = \sum_{i=1}^r \text{with } [p \leq \text{pixels per row} \leq q] \quad (3)$$

$$\text{colslines} = \sum_{i=1}^c \text{with } [p \leq \text{pixels per col} \leq q] \quad (4)$$

$$\text{rowspercent} = \frac{\text{rowslines}}{r} \leq \mu \quad (5)$$

$$\text{colpercent} = \frac{\text{colslines}}{c} \leq \mu \quad (6)$$

The linear feature detection step removes large regions that do not represent curbs because their shape is not linear. Nevertheless, there could be short nonlinear regions that, due to their small size, satisfy the linear condition, even without representing a curb. To avoid that, the relationship between the number of columns and rows is determined for each region. The computed region aspect ratio must have a value between the established thresholds (m and n in Eq. (7)).

$$m \leq \frac{\#cols}{\#rows} \leq n \quad (7)$$

The final result of the linear feature detection is a binary image in which 1-value pixels represent the location of curbs in the studied area. Pixels with a DV = 0 represent the background. At this moment, curbs and roadsides are located planimetrically (x and y coordinates). Fig. 3 shows the results obtained in every step of the procedure for one slice of every study test site. The final binary images obtained for each site are shown in Fig. 3(e) and (f).

3.5. Edge detection

3.5.1. 3D cloud recovery

Once the curb binary image has been produced, it is necessary to recover the 3D point cloud to detect the upper and lower curb edges. Thus, we move from the 2D raster image to a new 3D point cloud. This new point cloud will be more manageable than the original one because it is formed only by those points of the rotated point cloud (obtained in Step 3.1), which are contained in the 1-value pixels of the binary image.

3.5.2. Edge point detection

From the cloud of candidate points, the upper and lower edges of curbs are detected by performing a $\pm 45^\circ$ rotation around the x-axis, which is coincident with the average trajectory of the vehicle. Thus, the surfaces of the sidewalks, curbs, and roads, formerly horizontal and vertical, now have a slope of $\pm 45^\circ$, which is similar to the profile of a mountain and a valley (Fig. 4). This is valid even the road is sloped or flat due to the previous coordinate system change. This procedure helps in the edge curb extraction process because, in this way, the problem is reduced to detect changes in the slope sign.

In the data file provided by the laser scanner, the point cloud is organized according to the GPS time at which every point was scanned. To detect the points that represent the upper and lower edges of each curb, every point is compared with the previous and the next scanned points in the point cloud file. The slope of the vectors which links the studied point with its neighbor points is computed. If both calculated slopes have the same sign, the studied point represents a point in a vertical or horizontal surface (Fig. 5(a) and (c)). If the slopes have different signs, the studied point represents a change in slope and corresponds to an upper or lower curb edge (Fig. 5(b) and (d)).

The output of this step is a point cloud in which every point represents the upper or lower edges of the curbs that exist in the studied area (Fig. 6). From the edge curb point cloud, it is easy to determine those points in the scanned point cloud that belong to the sidewalk from those that belong to the road.

3.6. Estimation of non-detected boundaries

It is not always possible to detect the curbs and road boundaries based on MLS point clouds. Several obstacles on any given street may obstruct the view of curbs (street furniture, vehicles, or pedestrians that are between the MLS and the curb at the time of measurement). In other cases, the roadside exists but is not detectable with the proposed method. This occurs with access ramps at crosswalks: the curbs in these areas are at the same level as the road, making it difficult to detect the street boundary.

A method to estimate the locations of curbs and street boundaries is presented in this step. To perform it, we assume that non-detected boundaries must be aligned with their nearest neighboring boundaries correctly detected. From the 2D mask obtained in Step 3.4.3, a regional

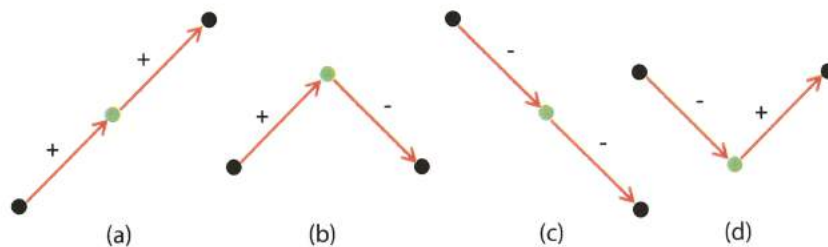


Fig. 5. Graphics (a) and (c) represent cases in which the studied point (the one in green color) does not represent a slope change; (b) and (d) show those situations in which the studied point represents a slope change and thus represents a curb edge. (For interpretation of the references to color in this figure legend, the reader is referred to the web version of this article.)

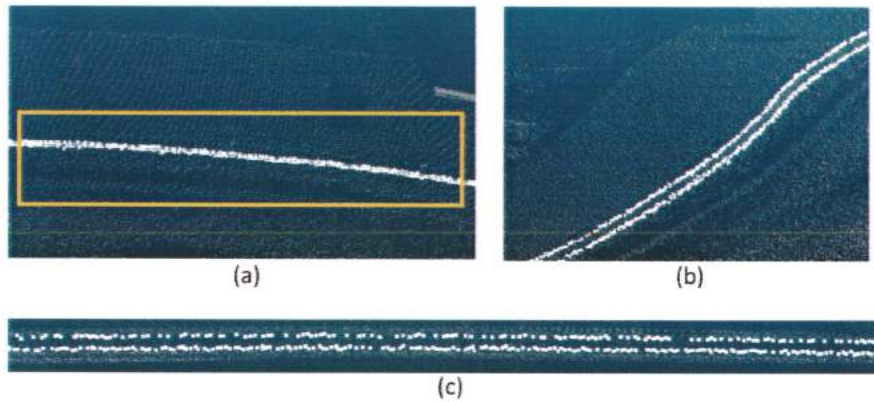


Fig. 6. (a) Curb section in the original point cloud, (b) curb section overlapped by detected curb edges (in white color), and (c) points detected as edges in a longitudinal profile marked in Fig. 7(a).

study is carried out in order to determine the direction of every curb region. Thus, for every region, three directions are computed: its direction, the nearest neighboring region's direction, and the direction of the vector that joins the centroids of both regions. These three two-dimensional vectors will determine the direction of both regions. If every vector has the same direction, the studied regions are aligned, and it is considered to be a roadside that was not detected by the proposed method. The cross-product is used to verify the fact that the vectors have the same direction. If the vectors are collinear, the cross-product between each pair must be null. In this case, we assumed that, between the two regions, a non-detected curb section exists (Fig. 7(a)). The proposed method cannot determine the existence of a non-detected boundary for those regions that are not collinear due to the fact that their directions are different (Fig. 7(b)).

The automatic method presented here for hidden boundaries curb estimation works properly only in straight curb sections. Other works, like those of Hervieu and Soheilian [36], have proposed a semi-automatic method for curb detection in curved sections, in which the user must supply the curb direction to the algorithm.

4. Test cases

4.1. MLS sensor

To determine the accuracy of the developed method, it was tested in two test sites acquired with the Lynx Mobile Mapper system, produced by Optech Inc. The lynx scanner collects survey-grade LIDAR data at

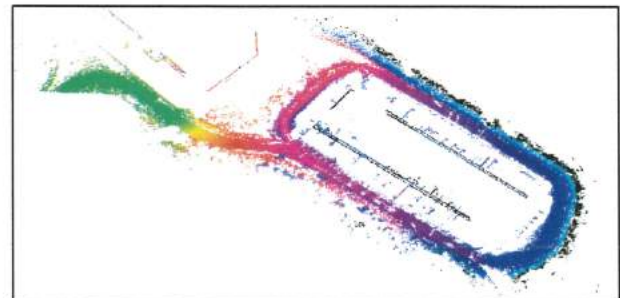
500,000 measurements per second with a 360° field of view (FOV). The Lynx also incorporates the POS LV 520, by Applanix, which integrates an IMU with a 2-antenna heading measurement system. LIDAR



(a)



(b)



(c)

Fig. 8. Test Site 1: (a) aerial image, (b) street appearance and (c) measured point cloud.

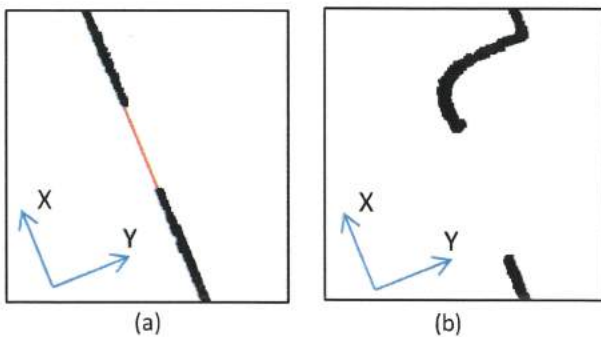


Fig. 7. (a) Collinear regions (in black) detected and the boundary estimated between both (in red); (b) non-collinear regions detected in the original point cloud with the proposed method.

sensors are located in the rear of a van. Each sensor registers points in a plane at 60° to the horizontal and 45° to the longitudinal axis of the vehicle (i.e. driving direction). This laser scanner provides absolute accuracies of 0.015° in heading, 0.005° in roll and pitch, 0.02 m in X, Y positions, and 0.05 m in Z. All these values are determined via differential GPS post-processing after data collection using GPS base station data [42]. One advantage provided by the MLS is the possibility of generating a geo-referenced point cloud combining LIDAR sensor data with IMU and a GPS installed in the mobile platform. The spatial resolution of the point cloud depends on the scan frequency of the LIDAR heads, the pulse repetition rate, the speed of the vehicle, and the distance to the measured objects [43].

4.2. Algorithm settings

The accuracy of the curb detection is directly related to the correct selection of different parameters. These settings depend on the attributes of the input point cloud and the environment of the studied road. We have realized that the critical parameters are (1) the pixel size of the grid, (2) the height difference restrictions in the threshold step, and (3) the point density. For the test sites used in this work, the pixel size was established at 5×5 cm. The characteristics of the existing curbs directly affect the height difference (Δh) parameter. Typically, the curb height is about 0.15 m, but it can vary depending on the studied area. The minimum (H_{min}) and maximum (H_{max}) curb height thresholds for both test sites were set to 0.10 m and 0.20 m, respectively. The point density (D_{min}) in each pixel was set to 5 points/pixel. Other parameters, such as line width, line percent, and region aspect ratio, are less dependent on the characteristics of the cloud. They take similar values in every case because they refer to the properties of lines rather

than those of the curbs. The line width (p and q thresholds) was set between three and six pixels, and the line percent (μ) was set to 80%. The region aspect ratio was fixed at 3 to 1. The values of the parameters for the study cases are listed in Table 1. The same settings were applied to both test sites. In both test sites the cloud is split in 150 m long slices. Every slice is computed separately in order to decrease the computational cost of the procedure. This split makes possible to detect curbs in curved sections.

4.3. Test Site 1

The point cloud used in Test Site 1 was measured in a polygonal park close to Vigo, in the north of Spain. In this area, there is an industrial-type building with an area of 9000 square meters. Around it, there is a two-way road that is 800 m long with both, straights and curved sections (Fig. 8). The presence of cars, trucks, and other obstacles, such as fences, lampposts, and poles, makes the roadside detection more difficult. The detected point cloud consists of more than 45 million points. This test site was used to check the capacity of the proposed method to detect curb edges.

4.3.1. Reference data

To evaluate the accuracy of the curb detection, a manual extraction of the road boundaries from the original point cloud was carried out. It was performed by digitizing the observed road borders from the point cloud as the ground truth data. For Test Site 1, the ground truth has a length of almost 1098 m. The evaluation of the results was carried out by comparing the curbs extracted via the proposed method with the previously prepared ground truth. This was performed by using three indices commonly used in the evaluation of

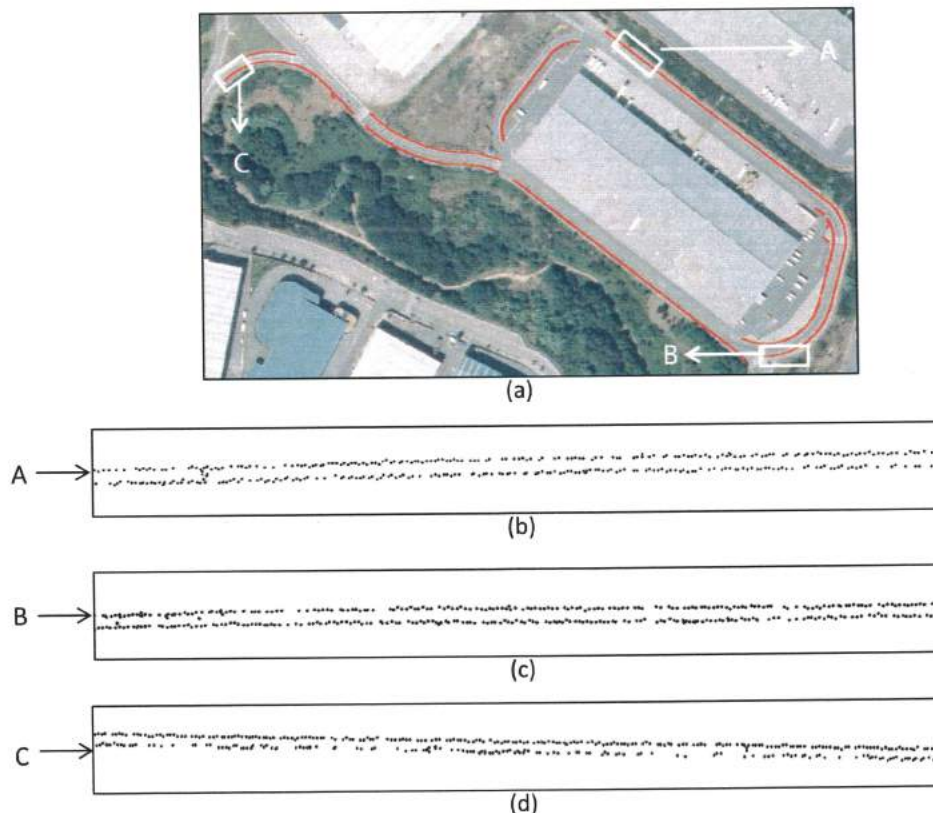


Fig. 9. (a) The point cloud formed by the upper and lower edges detected (in red), overlapping an aerial image of Test Site 1; (b), (c) and (d) represent points detected as upper and lower edges in A, B, and C details. (For interpretation of the references to color in this figure legend, the reader is referred to the web version of this article.)

Table 2

Accuracy of the detection method at Test Site 1.

Test Site 1	Algorithm-detected (AD)	User-detected	FP	FN	TP = AD – FP
Data-present curbs	1072.5	1097.8	18.1	25.3	1054.4
Completeness	97.65%	Correctness	98.31%	Quality	96.05%

road detection: completeness (Eq. (8)), correctness (Eq. (9)), and quality (Eq. (10)) [11,44,45].

$$\text{Completeness} = \frac{\text{length of matched reference}}{\text{length of reference}} = \frac{TP}{TP + FN} \quad (8)$$

$$\text{Correctness} = \frac{\text{length of matched extraction}}{\text{length of extraction}} = \frac{TP}{TP + FP} \quad (9)$$

$$\begin{aligned} \text{Quality} &= \frac{\text{length of matched extraction}}{\text{length of extracted + unmatched reference}} \\ &= \frac{TP}{TP + FP + FN} \end{aligned} \quad (10)$$

where TP (true positive) represents the length of the curb detected that matches the reference roadside, FP (false positive) represents the length of the detected curbs that do not matching with the ground truth, and FN (false negative) represents the total length of the undetected curbs that exist in the ground truth.

4.3.2. Results

For a visual analysis of the results obtained in Test Site 1, the detected curbs have been superimposed on an ortho-image of the studied

area (Fig. 9(a)). The result of the curb edge detection method is shown in three detailed images, which represent the curved and straight section of the test site (Fig. 9(b), (c) and (d)).

The proposed method identified 1072.5 m as curb from the Test Site 1 data, of which 18 m represents false positives caused by low vegetation and elements with geometry similar to those of curbs, such as car bottoms and steps. 1054.5 m of the detected curb matched the ground truth curb, and 25.3 m that belonged to the ground truth were not detected via the method due to the occlusion of the curb by grass or low vegetation. In these cases it is not possible to achieve the detection because of the change in the curb geometry. The parameters used to measure the accuracy of our method are written in Table 2. It can be appreciated that they are all above 96%.

4.4. Test Site 2

Test Site 2 corresponds to a 250 meter section of Rua Progreso Street in Ourense, a city in the north of Spain. This is a typical urban area that has a road with structured road boundaries in the form of curbs and ramps at crosswalks and garages (Fig. 10). These elements and others, such as cars and pedestrians, create shadows in the point cloud. Test Site 2 was used to test the performance of the proposed method of estimating those non-detected boundaries. The point cloud corresponding to Test Site 2 consisted of more than 18 million points.

4.4.1. Reference data

The results obtained for the detection and estimation procedures at Test Site 2 were evaluated by comparing the extraction with the two ground truth datasets. One ground truth was composed by curbs observed in the point cloud and it consists of more than 370 m of curbs. The other ground truth was formed by occluded curbs and

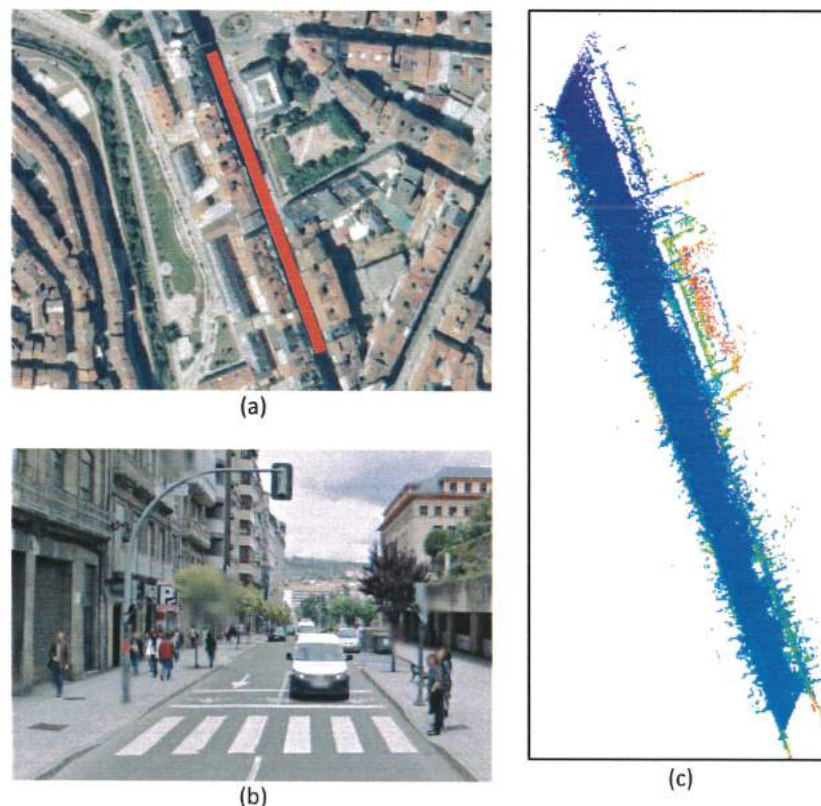


Fig. 10. Test site 2: (a) aerial image, (b) street appearance, and (c) measured point cloud.

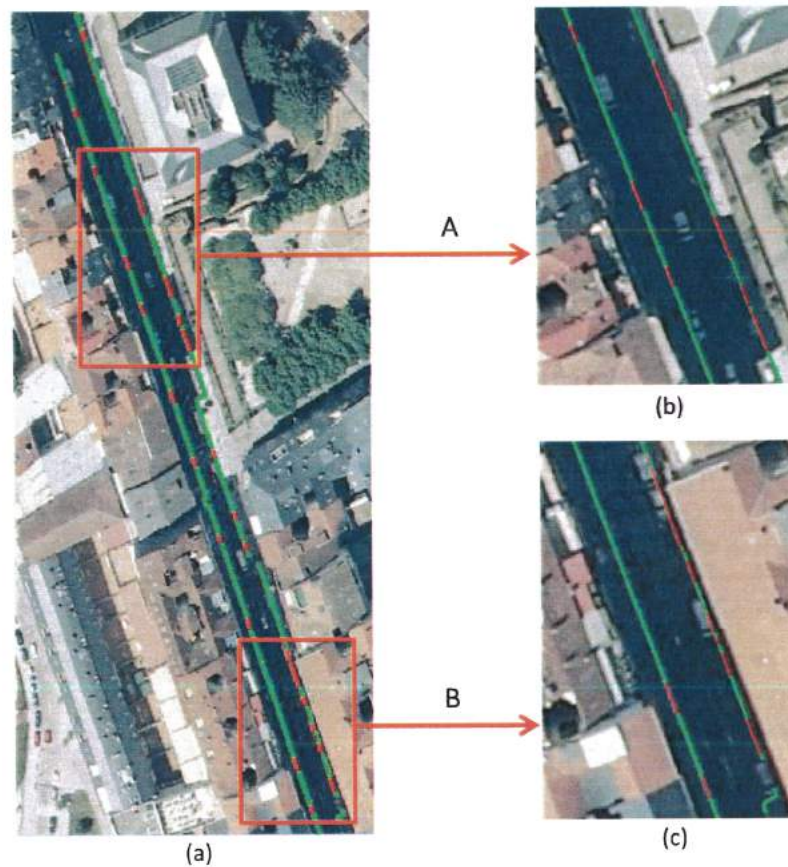


Fig. 11. (a) The detected curbs (green color) and estimated boundaries (red color) for Test Site 2; (b) and (c) show the results obtained in details A and B. (For interpretation of the references to color in this figure legend, the reader is referred to the web version of this article.)

ramps at sidewalks and garages. It consisted of more than 115 m and was used to evaluate the results of the curb estimation method.

4.4.2. Results

The detected curbs (green lines) and estimated sections (red lines) were rasterized and superimposed on an ortho-image of the studied area (see Fig. 11) in order to improve the visualization. Most of the detected segments in Fig. 11 are parallel to the vehicle trajectory, although a segment perpendicular to that is shown in the lower right corner of the image (c).

According to the results listed in Table 3, almost 358 m of curb was detected using our algorithm, of which only 2 m did not match the data present in the ground truth curbs. However, around 15 m that existed in the ground truth were not detected. According to these results, completeness, correctness and quality obtained were 95.9%, 99.36%, and 95.31%, respectively. Regarding the hidden boundaries, 112 m of the 116 m of hidden boundaries were delineated. Almost

4 m of hidden boundaries in the ground truth were not estimated via the method. These FN are located in curved sections. There was no FP in the estimation procedure, meaning that the completeness and quality values took the same values, providing a correctness of 100%. Almost 97% completeness and quality were achieved for the boundary estimation method.

5. Conclusions

In this paper, a novel method to detect and estimate curbs and street boundaries from MLS data is presented. The method begins with a coordinate system transformation and a rasterization that simplify the calculations involved and allow the use of image processing techniques to define linear features. Finally, edge points are detected by rotating the point cloud and looking for those points that represent a slope change. The upper and lower edges of the curb are extracted, resulting in a 3D representation of the road boundaries. In addition, an estimation of the boundaries is carried out in occluded areas located between straight segments by means of the direction and distance analysis of the neighboring detected segments.

The method was tested in two areas, one of which corresponded to an urban environment and the other corresponded to an industrial environment. The results obtained show completeness, correctness, and quality values higher than 95% for both detected and estimated boundaries. These results are quite better than the ones provided by other methods as [35] and [46] and are accurate enough for an autonomous driving system. From the results obtained at both test sites, it is possible to conclude that the proposed method is valid (1) for detecting the change of shapes road boundaries both in straight and curved road

Table 3
Accuracy of the detection and estimation method at Test Site 2.

Test Site 2	Algorithm detected	User detected	FP	FN	TP = AD – FP
Data-present curbs	357.5	370.4	2.3	15.2	355.2
Data-hidden boundary	111.8	115.5	0	3.7	111.8
Test Site 2	Data-present Curbs		Data-hidden boundaries		
Completeness	95.9%		96.8%		
Correctness	99.36%		100%		
Quality	95.31%		96.8%		

sections, (2) for accurately estimating the location of occluded curbs and undetected straight boundaries, and (3) for accurately determining the upper and lower curbs' edges. However, it is still difficult to deal with occluded curbs in curved sections and with boundaries without 3D shapes. In the near future, other variables as the topology or the texture will be incorporated to enhance the estimation method.

Acknowledgments

The authors would like to thank the Spanish Ministry of Science and Innovation for financial support, Project No. CGL2010-15357/BTE and Project No. BIA2011-26915.

References

- [1] X. Ding, W. Kang, J. Cui, L. Ao, Automatic extraction of road network from aerial images, *International Symposium on Systems and Control in Aerospace and Astronautics (ISSCAA)*, 2006, pp. 220–223.
- [2] R. Schmidt, H. Weisser, P. Schulenberg, H. Goellinger, Autonomous driving on vehicle test tracks: overview, implementation and results, *Proceedings of the IV IEEE Intelligent Vehicles Symposium*, 2000, pp. 152–155.
- [3] C. Urmsion, J. Anhalt, D. Bagnell, C. Baker, R. Bittner, M.N. Clark, H. Bae, T. Brown, D. Demitrius, J. Struble, M. Darms, Autonomous driving in urban environments: boss and the urban challenge, *J. Field Rob.* 25 (2008) 425–466.
- [4] J. Maye, R. Kaestner, R. Siegwart, Curb detection for a pedestrian robot in urban environments, *IEEE International Conference on Robotics and Automation (ICRA)*, 2012, pp. 367–373.
- [5] J.B. Mena, State of the art on automatic road extraction for GIS update: a novel classification, *Pattern Recogn. Lett.* 24 (2003) 3037–3058.
- [6] M.F. Auclair-Fortier, D. Ziou, C. Armenakis, S. Wang, Survey of work on road extraction in aerial and satellite images, *Can. J. Remote. Sens.* 27 (2001) 76–89.
- [7] C. Zhang, Towards an operational system for automated updating of road databases by integration of imagery and geodata, *ISPRS J. Photogramm. Remote Sens.* 58 (2004) 166–186.
- [8] S. Clode, F. Rottensteiner, P. Kootsookos, E. Zelniker, Detection and vectorization of Roads from Lidar Data, *Photogramm. Eng. Remote Sens.* 73 (2007) 517–535.
- [9] J. Amini, M.R. Saradjian, J.A.R. Blais, C. Lucas, A. Azizi, Automatic road-side extraction from large scale imagemap, *Int. J. Appl. Earth Obs. Geoinf.* 4 (2002) 95–107.
- [10] M. Song, D. Civco, Road extraction using SVM and image segmentation, *Photogramm. Eng. Remote Sens.* 70 (2004) 1365–1371.
- [11] S. Clode, P.J. Kootsookos, F. Rottensteiner, The Automatic Extraction of Roads from Lidar Data, presented at the ISPRS, Istanbul, Turkey, 2004.
- [12] I. Laptev, H. Mayer, T. Lindeberg, W. Eckstein, C. Steger, A. Baumgartner, Automatic extraction of roads from aerial images based on scale space and snakes, *Mach. Vis. Appl.* 12 (2000) 23–31.
- [13] X.Y. Jian, H. Bunke, Fast segmentation of range images into planar regions by scan line grouping, *Mach. Vis. Appl.* 7 (2) (1994) 115–122.
- [14] M. Varela-González, H. González-Jorge, B. Riverio, P. Arias, Performance Testing of 3D Point Cloud Software, presented at the ISPRS Workshop Laser Scanning, Antalya, Turkey, 2013.
- [15] D. Belton, K. Bae, Automating post-processing of terrestrial laser scanning point clouds for road feature surveys, *Int. Arch. Photogramm. Remote. Sens. Spat. Inf. Sci.* XXXVIII (2010) 74–79.
- [16] D. Gonzalez-Aguilera, A.L. Muñoz, J.G. Lahoz, J.S. Herrero, M.S. Corchon, E. García, Recording and Modeling Paleolithic Caves through Laser Scanning, *International Conference on Advanced Geographic Information Systems & Web Services (GEOWS)*, 2009, pp. 19–26.
- [17] X.-j. Cheng, H.-f. Zhang, R. Xie, Study on 3D laser scanning modeling method for Large-Scale history building, *International Conference on Computer Application and System Modeling (ICCSM)*, 2010 pp. V7-573–V7-577.
- [18] D. Tapete, G. Gigli, F. Mugnai, P. Vannocci, E. Pecchioni, S. Morelli, R. Fanti, N. Casagli, Correlation between erosion patterns and rockfall hazard susceptibility in hilltop fortifications by terrestrial laser scanning and diagnostic investigations, *IEEE International Geoscience and Remote Sensing Symposium (IGARSS)*, 2012, pp. 4809–4812.
- [19] R. Argüelles-Fraga, C. Ordóñez, S. García-Cortés, J. Roca-Pardiñas, Measurement planning for circular cross-section tunnels using terrestrial laser scanning, *Autom. Constr.* 31 (2013) 1–9.
- [20] M. Pejić, Design and optimisation of laser scanning for tunnels geometry inspection, *Tunn. Undergr. Space Technol.* 37 (2013) 199–206.
- [21] H. Park, S. Lim, J. Trinder, R. Turner, 3D surface reconstruction of Terrestrial Laser Scanner data for forestry, *IEEE International Geoscience and Remote Sensing Symposium (IGARSS)*, 2010, pp. 4366–4369.
- [22] W. Ni, G. Sun, Z. Guo, Y. Pang, Characterization of soil surface roughness from terrestrial laser scanner data, *IEEE International Geoscience and Remote Sensing Symposium*, 2009, pp. II-428–II-431.
- [23] C. Perez-Gutiérrez, J. Martínez-Fernández, N. Sánchez, J. Álvarez-Mozos, Modeling of soil roughness using terrestrial laser scanner for soil moisture retrieval, *IEEE International Geoscience and Remote Sensing Symposium (IGARSS)*, 2007, pp. 1877–1880.
- [24] G. Vosselman, Advanced Point Cloud Processing, presented at the Photogrammetric week, Wichmann, 2009.
- [25] M. Rutzing, S. Oude Elberink, S. Pu, G. Vosselman, Automatic extraction of vertical walls from mobile and airborne laser scanning data, presented at the The International Archives of Photogrammetry, Remote Sensing and Spatial Information Sciences, Paris, 2009.
- [26] K. Hammoudi, F. Dornaika, N. Paparoditis, Extracting building footprints from 3D point cloud using terrestrial laser scanning at street level, presented at the ISPRS/CMRT09, Paris, 2009.
- [27] C. Brenner, Extraction of Features from Mobile Laser Scanning Data for Future Driver Assistance Systems, in: M. Sester, L. Bernard, V. Paelke (Eds.), *Advances in GIScience*, Springer Berlin Heidelberg, 2009, pp. 25–42.
- [28] M. Lehtomäki, A. Jaakkola, J. Hyypä, A. Kukko, H. Kaartinen, Detection of vertical pole-like objects in a road environment using vehicle-based laser scanning data, *Remote Sens.* 2 (2010) 641–664.
- [29] J. Ruyi, K. Reinhard, V. Tobl, W. Shigang, Lane detection and tracking using a new lane model and distance transform, *Mach. Vis. Appl.* 22 (2011) 721–737.
- [30] R. Labayrade, J. Douret, D. Aubert, A multi-model lane detector that handles road singularities, *IEEE Intelligent Transportation Systems Conference (ITSC '06)*, 2006, pp. 1143–1148.
- [31] J. Siegemund, D. Pfeiffer, U. Franke, W. Forstner, Curb reconstruction using Conditional Random Fields, *IEEE Intelligent Vehicles Symposium*, 2010, pp. 203–210.
- [32] K. ZuWhan, Robust lane detection and tracking in challenging scenarios, *IEEE Trans. Intell. Transp. Syst.* 9 (2008) 16–26.
- [33] G. Zhao, J. Yuan, Curb detection and tracking using 3D-LIDAR scanner, *IEEE International Conference on Image Processing (ICIP)*, 2012, pp. 437–440.
- [34] T. Weiss, K. Dietmayer, Automatic Detection of Traffic Infrastructure Objects for the Rapid Generation of Detailed Digital Maps using Laser Scanners, *IEEE Intelligent Vehicles Symposium*, 2007, pp. 1271–1277.
- [35] B. Yang, L. Fang, J. Li, Semi-automated extraction and delineation of 3D roads of street scene from mobile laser scanning point clouds, *ISPRS J. Photogramm. Remote Sens.* 79 (2013) 80–93.
- [36] A. Hervieu, B. Soheilian, Semi-automatic road/pavement modeling using mobile laser scanning, presented at the City Models, Roads and Traffic—CMRT13, Antalya, Turkey, 2013.
- [37] P. Kumar, C.P. McElhinney, P. Lewis, T. McCarthy, An automated algorithm for extracting road edges from terrestrial mobile LiDAR data, *ISPRS J. Photogramm. Remote Sens.* 85 (2013) 44–55.
- [38] VirtualGrid, Available: <http://vrmesh.com>, 2014.
- [39] N. Haala, C. Brenner, Extraction of buildings and trees in urban environments, *ISPRS J. Photogramm. Remote Sens.* 54 (1999) 130–137.
- [40] R.C. Gonzalez, R.E. Woods, *Digital Image Processing*, Pearson Education, 2011.
- [41] B. Rodríguez-Cuenca, J.A. Malpica, M.C. Alonso, Region-growing segmentation of multispectral high-resolution space images with open software, *Proceedings of IEEE International Geoscience and Remote Sensing Symposium (IGARSS)*, 2012, pp. 4311–4314.
- [42] I. Puente, H. González-Jorge, B. Riveiro, P. Arias, Accuracy verification of the Lynx Mobile Mapper system, *Opt. Laser Technol.* 45 (2013) 578–586.
- [43] C. Cabo, C. Ordóñez, S. García-Cortés, J. Martínez, An algorithm for automatic detection of pole-like street furniture objects from Mobile Laser Scanner point clouds, *ISPRS J. Photogramm. Remote Sens.* 87 (2014) 47–56.
- [44] C. Heipke, H. Mayer, C. Wiedemann, O. Jamet, Evaluation of automatic road extraction, *Int. Arch. Photogramm. Remote. Sens.* 32 (3-2W3) (1997) 47–56.
- [45] J. Hu, A. Razdan, J.C. Femiani, C. Ming, P. Wonka, Road network extraction and intersection detection from aerial images by tracking road footprints, *IEEE Trans. Geosci. Remote Sens.* 45 (2007) 4144–4157.
- [46] L. Zhou, G. Vosselman, Mapping curbstones in airborne and mobile laser scanning data, *Int. J. Appl. Earth Obs. Geoinf.* 18 (2012) 293–304.

CHAPTER 4

Post-classification processes

*Hoy veras, la luz que inunda todo
verás, por fin, el sol sobre nosotros
verás el cielo, grande azul y limpio
vas a ver donde se unen cielo y mar
con la vida en tus ojos.*

El valle de Arán, Carlos Núñez

The final quality of a classification process depends on the discriminating variables, the quality of the training fields in the supervised classification and the accuracy of the classification algorithm. All classification processes, however, share common aspects. Thus, when a classification procedure is applied to an image, the classified image usually leaves a small number of isolated, poorly classified, or unclassified pixels. This results in a noisy, salt-and-pepper appearance due to the inherent spectral variability encountered when applied on

a pixel-by-pixel basis [6]. In such cases, it is desirable to homogenize the classification by “smoothing,” that is, reassigning the pixels to another class.

One means of classification smoothing applying a majority filter. In such operations, a moving window is passed through every classified pixel. If the label of the pixel is not in the majority class of the window, its identity is changed to the majority class. If there is no majority class in the window, the identity of the center pixel is not changed. As the window progresses through the data set, the original class code is continually used, not the modified labels from the previous window position. (Eastman, 1995). Majority filters can also incorporate some form of class and/or spatial weighting function. Certain algorithms can preserve the boundaries between land cover regions and also involve a user-specified minimum area for any given land cover type that will be maintained in the smooth output [6].

4.1. Paper N°4: A spatial contextual post-classification method for preserving linear objects in multispectral imagery

4.1.1. Summary

Classification algorithms are useful for the segmentation and cartographic production from aerial and satellite multispectral images. Also, classification is commonly the first step in cartographic entities extraction from remotely sensed data. A pixel-by-pixel image classification usually produces high-level error as noise. Including spatial information in classification processes is useful for reducing salt-and-pepper effect in these procedures. The use of probabilistic label relaxation (PLR) method including second-order statistics has been advantageous in reducing the classification errors (references).

This article described a modified PLR method to extract linear structures, such as roads, sports facilities, and buildings. The modifications included adding contextual information and imposing directional information from aerial or

satellite images on the third-order probability statistics (PLR3) joint. The performance of the proposed method has been tested on synthetic and real images. Synthetic images with full and accurate ground truth facilitate complete numerical analysis of the accuracy and kappa coefficient of the different methods. Real aerial and satellite images can allow the potential of the proposed methods in real situations to be determined. The results show the suitability of using post-classification algorithms to improve image noise. The proposed PLR3 method is useful when it is important to retain lines or edges. It has been shown that the proposed method defines linear structures better than the Majority and classic PLR methods due to the inclusion of third-order statistics within the likelihood probabilistic calculation.

4.1.2. Quality Indicators

The current research has been published in the IEEE Transactions on Geoscience and Remote Sensing Journal, with an impact factor of 3.514 according to a 2014 JCR evaluation. This journal is indexed in different JCR categories, such as Geochemistry & Geophysics; Engineering, Electrical & Electronic; Remote Sensing; and Imaging Science & Photographic Technology. In all of them, it appears in the top quartile and is even situated in a very important position within the top quintile in the last three categories. The contribution of this article has been cited by other research works and has been referenced two times in the WOS and five in the SG. Partial results and details of this methodology have been published in other journal papers and conferences such as the 2011 Spanish Remote Sensing Association Conference [80].

All the contributions in this research field have enabled the development of knowledge in the area of fusion information, highly relevant in most intelligent systems, decision-making, and image processing.

A Spatial Contextual Postclassification Method for Preserving Linear Objects in Multispectral Imagery

Borja Rodríguez-Cuenca, *Student Member, IEEE*, Jose A. Malpica, and Maria C. Alonso

Abstract—Classification of remote sensing multispectral data is important for segmenting images and thematic mapping and is generally the first step in feature extraction. Per-pixel classification, based on spectral information alone, generally produces noisy classification results. The introduction of spatial information has been shown to be beneficial in removing most of this noise. Probabilistic label relaxation (PLR) has proved to be advantageous using second-order statistics; here, we present a modified contextual probabilistic relaxation method based on imposing directional information in the joint probability with third-order statistics. The proposed method was tested in synthetic images and real images; the results are compared with a “Majority” algorithm and the classical PLR method. The proposed third-order method gives the best results, both visually and numerically.

Index Terms—Classification smoothing, contextual classification, relaxation methods, remote sensing.

I. INTRODUCTION

CLASSIFICATION of multispectral image data based on spectral information is used in analyzing remotely sensed data. The objective of the classification process is to categorize all pixels in a satellite or aerial image into one of several land cover classes. This categorized data may then be used to produce thematic maps of the existing land cover present in an image. There are two main classification methods: supervised and unsupervised. In the former, samples of the information classes (land cover type) of interest in the image, called training sites, are identified [1]. From these training areas, statistics are first calculated and then used to classify each independent pixel of the entire image being examined. Decision rules are then applied; these can be nonparametric, such as minimum Euclidean distance, or parametric, such as Gaussian maximum likelihood (ML). In unsupervised classification, often referred to simply as cluster analysis, a computer algorithm partitions the image into self-defining spectral clusters. Supervised or unsupervised classification methods have generally used only information obtained from individual pixels; therefore, the final thematic maps tend to be somewhat noisy, in what is known as salt-and-pepper classified images [2], [3]. Pixels generally belong

to cover types that form a geographic region or cartographic entity; consequently, pixels that are close together are more strongly related than those that are spatially distant. A normal approach in identifying land cover classes is to complement the use of spectral information with spatial information obtained from neighboring pixels.

Improving per-pixel classification by incorporating both spatial and spectral information involves a two-stage process: First, a spatial filter is applied to achieve more homogeneous regions; second, a per-pixel classification algorithm is applied, as reported by Yildirim *et al.* [4]. These authors applied an ML algorithm to classify land cover and achieved an improvement over the extraction and classification of homogeneous object algorithm presented by Ketting and Landgrebe [5].

It is more common to apply the opposite procedure—postprocessing—rather than preprocessing, i.e., classifying by first using a per-pixel classification algorithm and then performing a postclassification operation. One of the simplest postprocessing operations is the application of a Majority filter [6], [7]. To conduct this operation, a moving window is passed over each pixel in the classified image. If the class assigned to the central pixel in the window is not the majority class of the window, the pixel’s class is changed to the majority class. If there is no majority class, the identity of the center pixel is not changed. As the window progresses through the image, the original class from the previous classified image is used, not the assigned class as modified from the previous window position [8]. Some authors have applied modifications to the Majority filter and achieved some improvement, such as [9], which used a Landsat Thematic Mapper image with an adaptive Majority filter, resulting in some reduction in classification errors.

In recent decades, several approaches have been adopted for incorporating contextual information into the classification of remote sensing fields, such as Markov random fields (MRFs) [10]–[14], knowledge-based methods or fuzzy methods [15]–[17], probabilistic label relaxation (PLR) [18], [19], and hybrids, combining other methods [20]. In this paper, the term *contextual information* will refer only to spatial information, even though this concept could also be extended to other types of miscellaneous information (ancillary data) associated with the current pixels, as proposed by some of the aforementioned studies.

In postprocessing methods, linear features are usually removed when trying to reduce the speckled appearance in a classified image, as found by Myeong *et al.* [21]. These authors observed this phenomenon when applying the Majority filter in postprocessing. In this paper, we develop a postprocessing approach that aims to preserve linear features.

This paper is organized as follows. Higher order statistics are described in Section II. The methodology applied with the

Manuscript received April 14, 2011; revised November 16, 2011; accepted April 1, 2012. Date of publication June 1, 2012; date of current version December 19, 2012. This work was supported in part by the Spanish Ministerio de Ciencia e Innovación under project CGL2010-15357 and in part by the University of Alcalá under project UAH 2011/EXP-031.

The authors are with the Department of Mathematics, University of Alcalá, 28871 Alcalá de Henares, Spain (e-mail: borja.rodriguezc@uah.es; josea.malpica@uah.es; mconcepcion.alonso@uah.es).

Color versions of one or more of the figures in this paper are available online at <http://ieeexplore.ieee.org>.

Digital Object Identifier 10.1109/TGRS.2012.2197756

proposed method is described in Section III. The results obtained using synthetic and real images are presented in Section IV. Finally, our conclusions are given in Section V.

II. HIGHER ORDER STATISTICS WITH PROBABILISTIC LABELING RELAXATION

Natural images exhibit statistical regularities that differentiate them from images in which pixels have been generated randomly; moreover, the human visual system appears to have evolved to exploit such statistical regularities. Many studies support the notion that our visual system presents an efficient means for coding the statistical structures found in nature [22], [23]. First-order statistics deal with single pixels and do not take into account relationships between neighboring pixels in an image. This first order implicates the histogram, mean, standard deviation, skew, and kurtosis of gray levels in an image. Second-order statistics examine relationships and regularities between pairs of pixels in an image. Examples include image gradients and power spectra, which are computed in Fourier space and are related to autocorrelation functions. Third-order statistics examine ternaries of pixels, as in the work of Gagalowicz and Ma [24], using co-occurrence matrices; these authors showed that such a third-order model was able to capture most of the information about macroscopic planar textures such as wool, sand, etc.

Studies on PLR focus on measuring second-order statistics or the covariation between the properties of paired pixels, such as their grayscale levels [19]. We show that it is practical to directly measure higher order statistics using the strategy of estimating the probability along different directions. Structural information about linear features can be retrieved through statistics of triples of pixel values (third-order statistics).

In the following equations, the procedure for supervised classification is considered from a statistical perspective. Let the classes be

$$\omega_i, \quad i = 1, \dots, C$$

where C is the total number of classes.

$$p_m \left(\frac{\omega_i}{\aleph_m} \right), \quad i = 1, \dots, C \quad (1)$$

is the probability of class ω_i occurring, given that pixel m and the neighborhood \aleph_m surrounding pixel m have been observed. In principle, a label is influenced by the real label of all other labels in the image, but in order to model the phenomenon of spatial context, we will here suppose that a label is influenced only by a few close neighbor pixels. We also suppose that this property of being influenced by only a small neighborhood is independent of the position in the image of the actual pixels. This is similar to the properties established in MRF [25].

Pixel m is assigned to class ω_i if

$$p_m \left(\frac{\omega_i}{\aleph_m} \right) \geq p_m \left(\frac{\omega_j}{\aleph_m} \right) \quad \forall i \neq j. \quad (2)$$

From Bayes' theorem, we have

$$p_m \left(\frac{\omega_i}{\aleph_m} \right) \propto p_{\omega_i}(m) \cdot p \left(\frac{\omega_i}{\aleph_m} \right) \quad (3)$$

where $p_{\omega_i}(m)$ is the class conditional probability for class ω_i given pixel m and $p(\omega_i/\aleph_m)$ is the prior probability of the ω_i class for neighborhood \aleph_m . This is a measure of how appropriate it is to assign pixel m to class ω_i , in view of the current neighborhood surrounding m , defined as \aleph_m .

Following Richards and Jia [26], the question is how to find a value for $p(\omega_i/\aleph_m)$. These authors have modeled this probability by both MRF and PLR with Dempster-Shafer; they found the latter to be better than the former. We will present a modification of the latter algorithm with a third-order statistic. Herein, the original PLR as applied by Richards and Jia [26] will be called PLR2 (as it utilizes second-order statistics), and our proposed method will be called PLR3.

Mahalanobis Classifier and Labeling Relaxation PLR2

The term $p(\omega_i/\aleph_m)$ in (3) is the initial estimate of the probability of each pixel's label for a neighborhood \aleph_m . These probabilities can be assigned from a previous classification based on pixel information alone. In our case, this was done using the Mahalanobis classifier. Per-pixel classification approaches, such as minimum Euclidean distance and ML, have been widely used in many remote sensing applications. The Mahalanobis classifier has been widely applied in the remote sensing community [19], [27]–[29]. It is a derivation of the ML discriminant function, specifically when the prior probabilities are considered to be equal [15]. The Mahalanobis distance is given by

$$(x - m_i)^t \sum^{-1} (x - m_i) \quad (4)$$

where m_i is the mean for class ω_i and \sum is the covariance matrix. Richards stated that "The maximum likelihood classifier can be regarded as a minimum distance measure that is direction sensitive and modified according to class." Simple minimum Euclidean distance classifiers have some limitations that can be overcome using a Mahalanobis metric. In particular, this can often address problems caused by poorly scaled or highly correlated features [30].

Label relaxation is an iterative heuristic technique that extracts contextual information from an image to reduce the ambiguity of predetermined labeling. Relaxation labeling utilizes two sources of information: an initial labeling for $p(\omega_i/\aleph_m)$ and information embedded in spatial context. Several of the early PLR algorithms were proposed in the late 1970s and 1980s. Among the most popular are probabilistic labeling relaxation [31] and the supervised extraction and classification of homogeneous objects developed by Landgrebe [32] and Richards *et al.* [33].

Following Richards [19]

$$p_m^k \left(\frac{\omega_i}{\aleph_m} \right) \quad (5)$$

is an estimate of the probability that, on the k th iteration, the label or class of the pixel m is ω_i . An iterative process was constructed in order to progressively modify the initial probability assigned to pixel m

$$p_m^{k+1} \left(\frac{\omega_i}{\aleph_m} \right) = \frac{p_m^k(\omega_i) \cdot Q_m^k(\omega_i)}{\sum_j p_m^k(\omega_j) \cdot Q_m^k(\omega_j)} \quad (6)$$

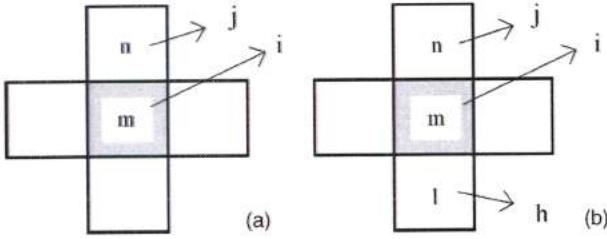


Fig. 1. (a) Second-order neighborhood for pixel m . (b) Third-order neighborhood for pixel m .

where $Q_m^k(\omega_i)$ is called the neighborhood function. Let \mathcal{N}_m be a neighborhood as in Fig. 1(a) [19]. With the new evidence obtained from Q , we modified this initial probability, which is known as the posterior probability.

The function $Q_m^k(\omega_i)$ can be defined as

$$Q_m^k(\omega_i) = \sum_n \sum_j p_{mn}(\omega_i | \omega_j) p_m^k(\omega_j) \quad (7)$$

where $p_{mn}(\omega_i | \omega_j)$ is the probability that pixel m belongs to class ω_i , given that n is from class ω_j .

Context With a Third-Order Statistic PLR3

In this paper, we extend PLR2 to a new label relaxation approach termed PLR3, in which we consider third-order statistics. Third-order statistics have been shown to be important in many other fields [22], [34], [35].

The matrix $p_{mn}(\omega_i | \omega_j)$ is constructed considering not just one neighboring pixel n but two neighbor pixels n and l , for the actual pixel m ; in this case, the conditional matrix will have the form $p_{mnl}(\omega_i | \omega_j, \omega_h)$. This is a conditional probability of seeing class ω_i for pixel m given the following configuration: Pixel n has class ω_j , and pixel l has class ω_h .

For example, if we consider that the two classes are in a vertical (V) disposition, as shown in Fig. 1(b), the neighborhood function will be given by

$$Q_m^k(\omega_i) = \sum_j \sum_h p_{mnl}(\omega_i | \omega_j, \omega_h) p_{nl}(\omega_j | \omega_h) p_l^k(\omega_h) \quad (8)$$

and the *a posteriori* probability will be given by the same expression as (6).

The algorithm described in this section was applied to a series of synthetic images and a real image. The methodology is explained in Section III, using the example of a synthetic image created with different directions.

III. METHOD

Two types of synthetic images (204×204 pixels) were used, one with horizontal (H) and V stripes and the other with diagonal stripes, as shown in Fig. 2. The images had four bands; the reason for choosing this number was because we also planned to use real images with four bands. Only two classes were considered for the experiments in an effort to simulate the extraction of a feature against a background, such as roads or other cartographic linear features. The synthetic image classes were produced with a random generator, and each band showed normal distributions: N1 [(40, 46, 46, 46), (10, 10, 10, 10)]

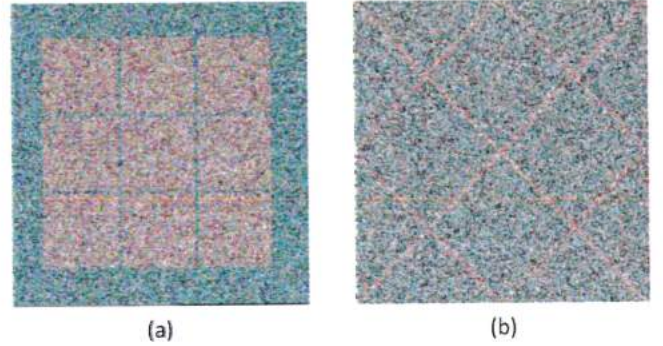


Fig. 2. Synthetic images (a) with H and V stripes and (b) with diagonal stripes.

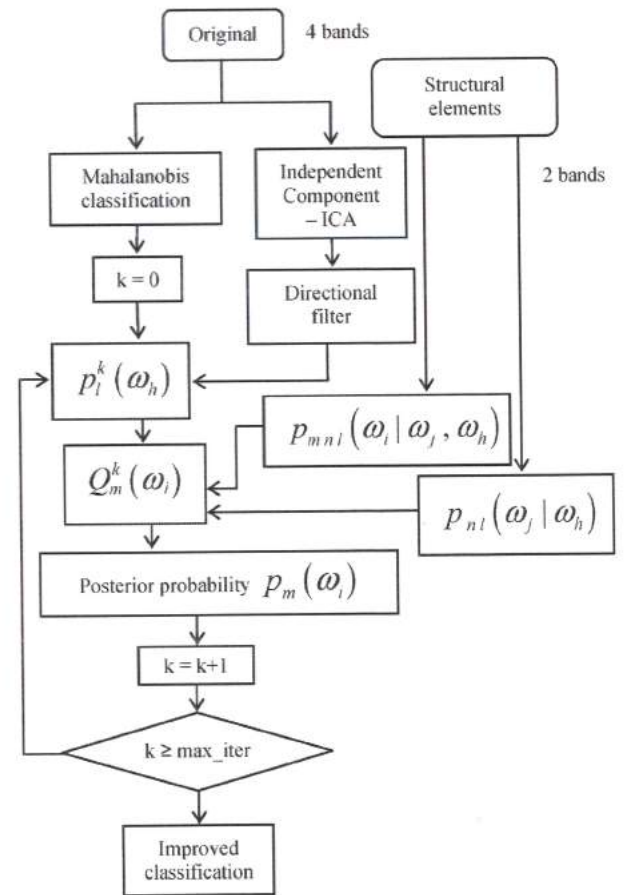


Fig. 3. Flowchart of the proposed method.

and N2 [(46, 46, 46, 40), (10, 10, 10, 10)] where the numbers represent different levels of gray for each band. Although only two classes were considered for the experiment, the method presented here would be valid for any number of classes.

Fig. 3 shows a flowchart of the proposed method. Entry of the algorithm is shown in the upper part. One of the inputs is the original image, which would be either a real or a synthetic image, as shown in Fig. 2(a) and (b).

The other input would be the structure to be detected in the original image. An example of this type of structure can be seen in Fig. 4. In Fig. 4(a), we look for H and V structures, and in Fig. 4(b), we look for principal (D1) and secondary (D2) diagonals.

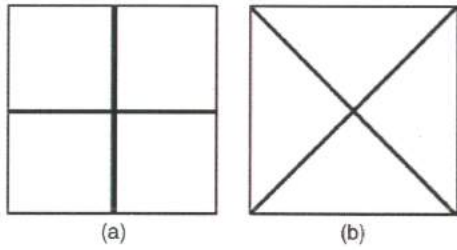


Fig. 4. Structural elements to be detected: (a) shows H and V structural elements, and (b) shows structural diagonals D1 and D2.

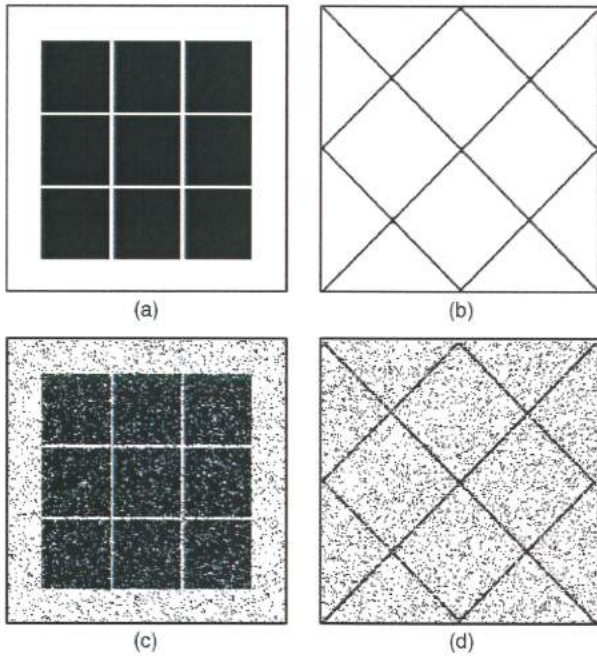


Fig. 5. (a) and (b) Ground truth. (c) and (d) Mahalanobis classification.

These structural elements are necessary to calculate the probabilities $p_{mn}(\omega_i|\omega_j)$ and $p_{mni}(\omega_i|\omega_j, \omega_h)$ and to determine the neighborhood function of (8). It also allows the proportions of the two classes to be determined depending on the directions, as shown in Fig. 4. For the PLR2 method, a pair of pixels is taken, as shown in Fig. 1(a), while in the PLR3 method, triples of pixels are considered, as shown in Fig. 1(b). These triples are examined only for linear structures in all directions (V, H, and D1 and D2), and so consequently, the method preserves such linear features in the postclassification process.

The next step in the procedure is supervised classification of the images shown in Fig. 2 using training fields. In our case, as stated in the previous section, a Mahalanobis classification distance was used in both images, using 10% of the ground-truth images as a training set [Fig. 5(a) and (b)]. The results of the classification are shown in Fig. 5(c) and (d).

In order to determine the direction in which the algorithm should be applied (H or V, or diagonal D1 or D2) in the current pixel, first, an independent component analysis (ICA) was carried out [36].

It is assumed that the reflectance of a pixel is a combination of the reflectances of endmember spectra in the area covered by that pixel; this mixture can be considered as the result of the linear combinations of these endmembers within the

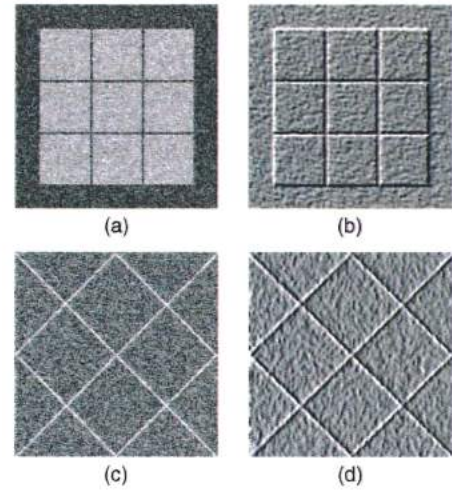


Fig. 6. (a) and (c) show the ICA H-V and D1-D2. (b) and (d) show the directional filter applied to the ICA analysis.

pixel [37]. Several authors have investigated the application of ICA methods to the analysis of remote sensing multispectral images [38]–[41]. ICA is defined as representing the pixel spectra by the linear combination of statistically independent components; since two classes are considered, two components were calculated for ICA. The features from the two classes behave to some extent like two different sources. For all cases of the synthetic and the real images, the first ICA band provided good differentiation between the features. Furthermore, a directional filter was used on the first band of the ICA to enhance identification of the adjacent pixel properties in all directions. The direction filter consisted of a 3×3 pixel window that studies the whole image, applying a higher weighting in a given direction (0° and 90° in the H and V and 45° and 315° in the D1 and D2). Fig. 6(a) and (c) shows the ICA images that contain edge information; Fig. 6(b) and (d) shows the directional filter applied to the ICA in order to enhance the directions.

The information from Fig. 6(b) and (d) is used to decide what values of $p_{mni}(\omega_i|\omega_j, \omega_h)$ and $p_{ni}(\omega_j|\omega_h)$ should be used for the H, V, D1, or D2 directions, in each pixel. In the actual pixel, the direction is obtained by exploring the neighborhood pixels shown in Fig. 6(b) and (d). This information is also utilized in calculating $p_i^k(\omega_h)$, which updates the posterior probability in each iteration k .

The classifications are evaluated using a confusion matrix: accuracy and kappa coefficient with its p-value and 95% confidence interval.

IV. RESULTS AND DISCUSSION

Fig. 7(a) shows the results of classifying the synthetic image shown in Fig. 2(a) by Mahalanobis distance, using 10% of the ground truth, shown in Fig. 5(a), as a training sample. Fig. 7(b)–(d) shows the postprocessing of the Mahalanobis classification. For Fig. 7(b), a Majority filter with a 3×3 window was applied, Fig. 7(c) was obtained with a PLR (PLR2), as explained by Richards and Jia [19], with three iterations, and in Fig. 7(d), the proposed PLR3 method was applied, also with three iterations. The key difference between PLR2 and PLR3 is that the former used the statistical distribution of pairs of

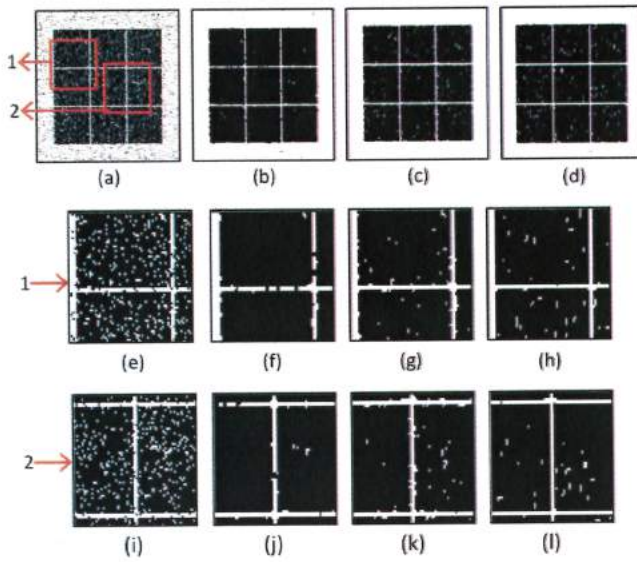


Fig. 7. Postprocessing of the (a) Mahalanobis classification with (b) Majority filter, (c) PLR2, and (d) PLR3 for the image with H and V structures. The details in (f)–(h) show the differences in the postprocessing algorithms. The white lines in (h), which correspond to PLR3, are better defined than the same lines in (f) (Majority) and (g) (PLR2). Similar results can be seen in the details of (j)–(l).

TABLE I

CONFUSION MATRICES FOR MAHALANOBIS, MAJORITY, PLR2, AND PLR3 FOR H AND V STRUCTURES FOR THE SYNTHETIC IMAGE IN FIG. 7

MAHALANOBIS				MAJORITY			
	Black	White	Total		Black	White	Total
Black	20573	1588	22161	Black	22623	156	22779
White	2228	14504	16732	White	178	15936	16114
Total	22801	16092	38893	Total	22801	16092	38893
(35077/38893) 90.19%				(38559/38893) 99.14%			
Kappa coefficient = 0.799, pvalue<0.001				Kappa coefficient = 0.982, pvalue<0.001			
CI 95% Kappa (0.793, 0.805)				CI 95% Kappa (0.980, 0.984)			

PLR2				PLR3			
	Black	White	Total		Black	White	Total
Black	22291	3	22294	Black	22363	31	22394
White	510	16089	16599	White	438	16061	16499
Total	22801	16092	38893	Total	22801	16092	38893
(38380/38893) 98.68%				(38424/38893) 98.79%			
Kappa coefficient = 0.973, pvalue<0.001				Kappa coefficient = 0.975, pvalue<0.001			
CI 95% Kappa (0.971, 0.975)				CI 95% Kappa (0.973, 0.977)			

pixels, while the latter used triples of pixels. It is observed that all three methods reduced the noise of the initial Mahalanobis classification, particularly the Majority filter in Fig. 7(b); however, PLR2 and PLR3 better delineate the linear entities, as can be seen in the details hereinafter, in Fig. 7(e)–(l). The images in Fig. 7(e) and (i) are details of the Mahalanobis classification shown in Fig. 7(a); in Fig. 7(f) and (j), corresponding to the Majority filter, black pixels invade white lines; in Fig. 7(g) and (k), corresponding to PLR2, white pixels occupy the black edges; Fig. 7(h) and (l), corresponding to PLR3, produces the best results in depicting the white lines.

To complement this visual analysis, we performed a numerical analysis in which the classification was evaluated using a confusion matrix of the full ground-truth data set [Fig. 5(a) and (b)]. Table I shows the results of the confusion matrices for Mahalanobis and the three postclassification methods.

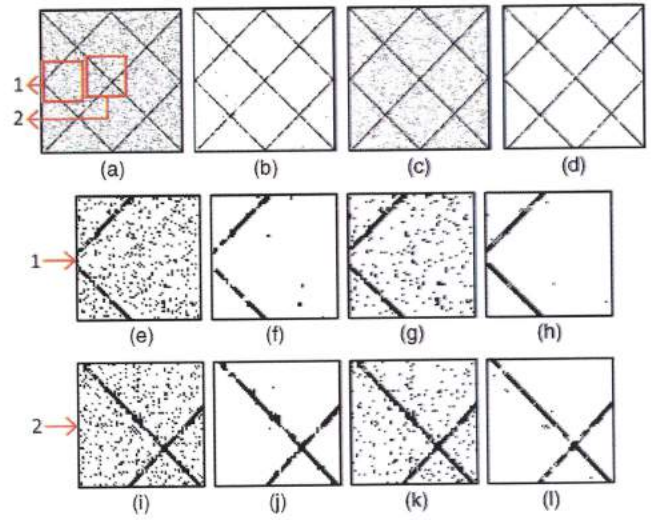


Fig. 8. Postprocessing of the (a) Mahalanobis classification with (b) Majority filter, (c) PLR2, and (d) PLR3 for the image with diagonals D1 and D2. Details in (e)–(l) show the differences in the postprocessing algorithms. (f) and (j) show two details of the Majority filter, (g) and (k) represent the results of the PLR2 algorithm, and (h) and (l) show the performance of the proposed algorithm PLR3.

TABLE II

CONFUSION MATRICES FOR MAHALANOBIS, MAJORITY, PLR2, AND PLR3 FOR D1 AND D2 STRUCTURES FOR SYNTHETIC IMAGE IN FIG. 8

MAHALANOBIS				MAJORITY			
	Black	White	Total		Black	White	Total
Black	1827	4628	6455	Black	1855	314	2169
White	280	31109	31389	White	252	35423	35675
Total	2107	35737	37844	Total	2107	35737	37844
(32936/37844) 87.03%				(37278/37844) 98.50%			
Kappa coefficient = 0.374, pvalue<0.001				Kappa coefficient = 0.860, pvalue<0.001			
CI 95% Kappa (0.360, 0.388)				CI 95% Kappa (0.848, 0.872)			

PLR2				PLR3			
	Black	White	Total		Black	White	Total
Black	1876	2554	4430	Black	1881	107	1988
White	231	33183	33414	White	226	35630	35856
Total	2107	35737	37844	Total	2107	35737	37844
(35059/37844) 92.64%				(37511/37844) 99.12%			
Kappa coefficient = 0.539, pvalue<0.001				Kappa coefficient = 0.914, pvalue<0.001			
CI 95% Kappa (0.523, 0.555)				CI 95% Kappa (0.904, 0.924)			

Note that the Majority method provides the best accuracy (99.14%) and kappa coefficient (0.982), with approximately 300 pixels misclassified; the PLR3 produced the second best accuracy (98.79% and kappa coefficient 0.9752) with almost 500 pixels incorrectly classified, but better defined linear features. Most of the decrease in PLR3 accuracy and kappa is because, for this case, the method, as well as the Majority method, does not clean noise; Majority reduced the noise but increased the misclassified pixels in the edges of linear structures. PLR2 was slightly less accurate (accuracy 98.68% and kappa 0.973) than the PLR3 and Majority algorithms.

For all methods, the p-value and a 95% confidence interval have been included. In all cases, the p-value was less than 0.001, indicating that the classifications obtained are significant. Although the confidence intervals for PLR2 and PLR3 have no empty intersection, which means that the difference

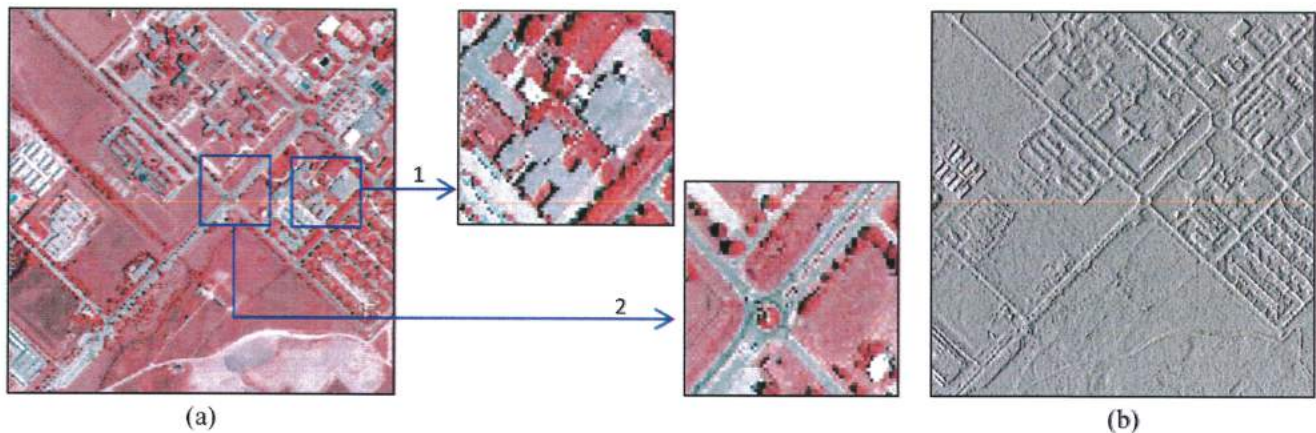


Fig. 9. (a) Aerial image of an area of Madrid with two details. Image (b) shows the first band of ICA with diagonal filters applied.

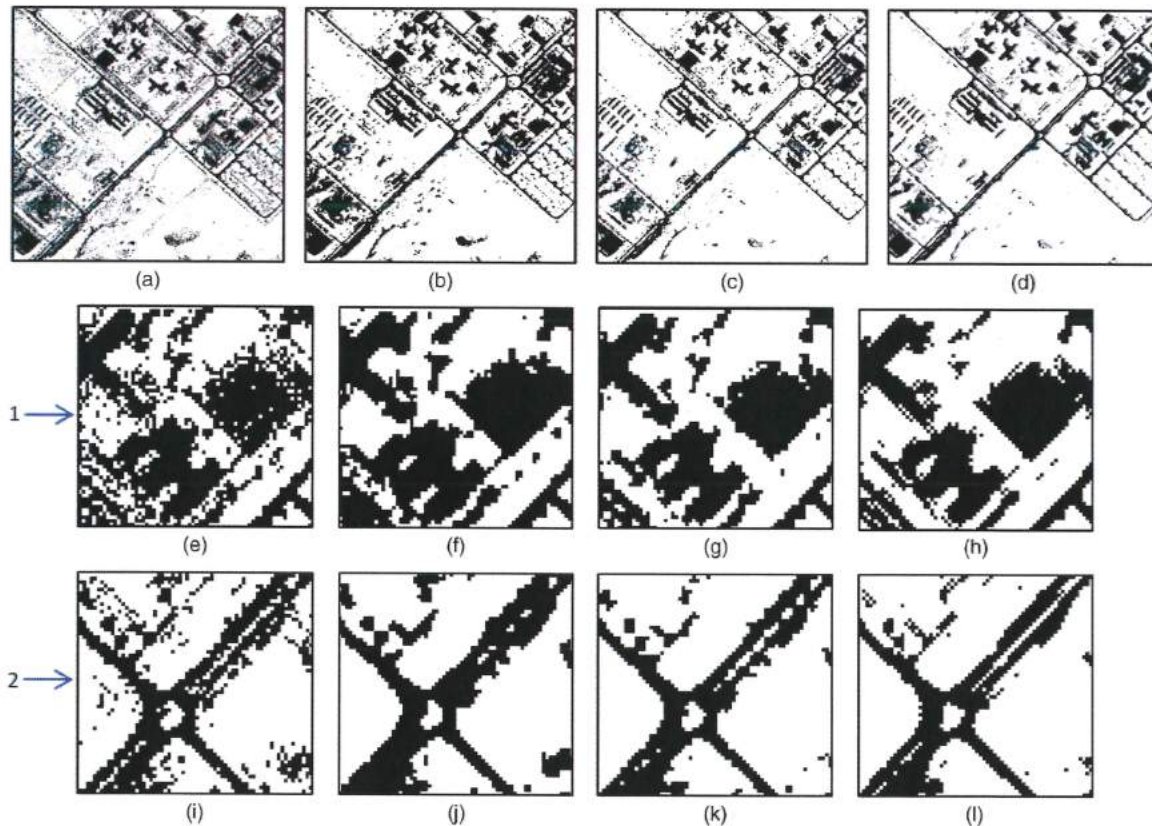


Fig. 10. Postprocessing of the (a) Mahalanobis classification with (b) Majority filter, (c) PLR2, and (d) PLR3 for the aerial image. Details in (e)–(l) show the differences in the postprocessing algorithms. (f) and (j) show two details of the Majority filter, (g) and (k) represent the results of the PLR2 algorithm, and (h) and (l) show the performance of the proposed algorithm.

between methods is statistically nonsignificant (as can be seen in Table I), the visual evaluation [Fig. 7(g) compared with Fig. 7(h) and Fig. 7(k) compared with Fig. 7(l)] shows that the edges are better represented by PLR3 than by PLR2.

We conducted a similar study for diagonal directions. The Mahalanobis classification and the three postclassification methods for Fig. 2(b) image with some details are shown in Fig. 8. Following the order of the aforementioned synthetic image, Fig. 8(a) corresponds to Mahalanobis classification, Fig. 8(b) corresponds to Majority filter, Fig. 8(c) corresponds to PLR2, and Fig. 8(d) corresponds to PLR3.

The worst performance of the three postclassification techniques in this case was the PLR2 method, which produced a lot of noise and poor determination of the linear features [Fig. 8(c)]. This is due to the shape of the neighborhood considered for PLR2, as this method studies the images in only H and V directions. The number of noisy pixels was similar in the Majority and PLR3 results; however, as with the previous synthetic image, PLR3 defined the linear features more accurately, as seen by comparing Fig. 8(b) and (d). Two details [Fig. 8(e)–(h) and (i)–(l)] have been provided to better see this idea. It can be observed that Fig. 8(h) and (l) are the

TABLE III
CONFUSION MATRICES FOR MAHALANOBIS, MAJORITY, PLR2, AND PLR3 FOR D1 AND D2 STRUCTURES FOR THE AERIAL IMAGE IN FIG. 9

MAHALANOBIS				MAJORITY			
	Black	White	Total		Black	White	Total
Black	689	280	969	Black	728	236	964
White	67	1612	1679	White	28	1656	1684
Total	756	1892	2648	Total	756	1892	2648
(2301/2648) 86.8958%				(2384/2648) 90.0302%			
Kappa coefficient = 0.704, pvalue<0.001				Kappa coefficient = 0.774, pvalue<0.001			
CI 95% Kappa (0.675, 0.733)				CI 95% Kappa (0.749, 0.799)			

PLR2				PLR3			
	Black	White	Total		Black	White	Total
Black	703	126	829	Black	726	141	867
White	53	1766	1819	White	30	1751	1781
Total	756	1892	2648	Total	756	1892	2648
(2469/2648) 93.2402%				(2477/2648) 93.5423%			
Kappa coefficient = 0.839, pvalue<0.001				Kappa coefficient = 0.848, pvalue<0.001			
CI 95% Kappa (0.815, 0.863)				CI 95% Kappa (0.826, 0.870)			

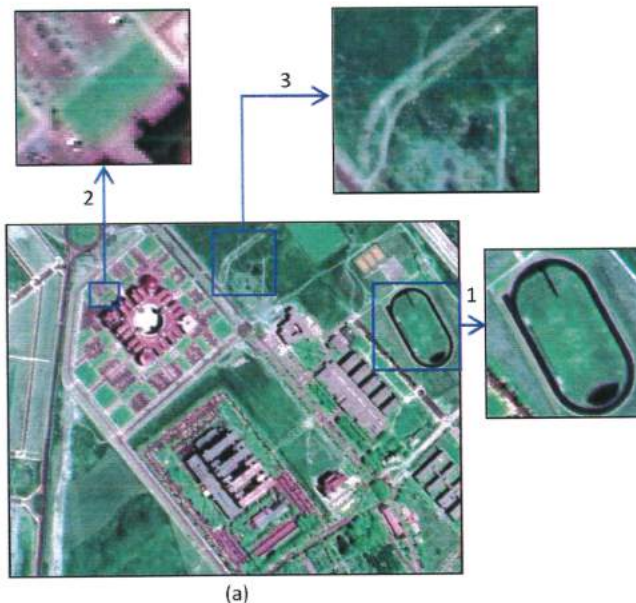


Fig. 11. Image (a) is a satellite image (Ikonos) of the Alcalá de Henares university campus (Madrid) with three details 1, 2, and 3. The bands for visualization with red, green, and blue are infrared, blue, and green, respectively.

best postprocessing classifications among the three methods, removing noise and preserving linear features, as confirmed by numerical analysis in Table II.

In this case, PLR3 provides the best accuracy (99.12%) and kappa (0.9140), while Majority provides an accuracy of 98.50% with a kappa of 0.860. As in Table I, PLR3 produced more noise in homogeneous regions than Majority but worked better at the edges. PLR3 and Majority present significant differences in the kappa coefficient because their confidence interval at the 95% level had an empty intersection.

Fig. 9 shows an aerial image (400×400 pixels) of Alcalá de Henares, Madrid, Spain, taken in summer 2010. This image was taken with a Leica ADS40 SH52 sensor, with a spatial resolution of 0.5 m and four spectral bands (red, green, blue, and near infrared). The two images on the right are the selected details. In this case, the diagonal neighborhood

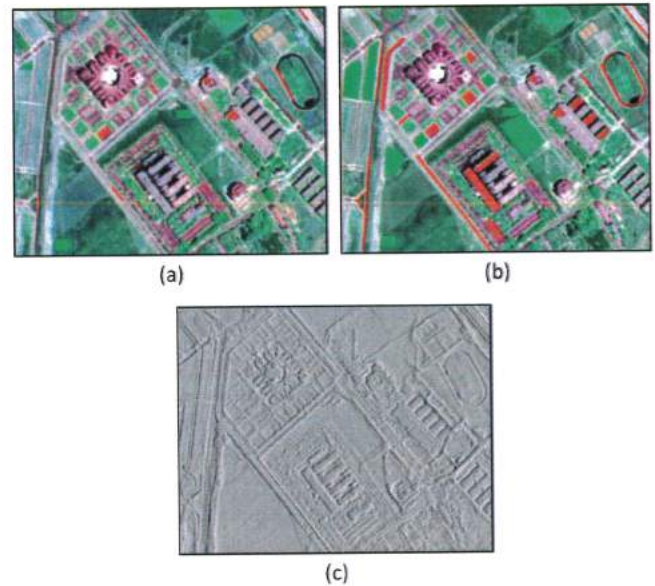


Fig. 12. Panels (a) and (b) show the training and evaluation sets, respectively, for Fig. 11 satellite image. Panel (c) shows the first band of ICA analysis with diagonal filters applied.

TABLE IV
CONFUSION MATRICES FOR MAHALANOBIS, MAJORITY, PLR2, AND PLR3 FOR D1 AND D2 STRUCTURES FOR IKONOS IMAGE IN FIG. 11

MAHALANOBIS				MAJORITY			
	Black	White	Total		Black	White	Total
Black	22900	116	23016	Black	23017	101	23118
White	1412	25209	26621	White	1295	25224	26519
Total	24312	25325	49637	Total	24312	25325	49637
(48109/49637) 96.9217%				(48241/49637) 97.1876%			
Kappa coefficient = 0.938, pvalue<0.001				Kappa coefficient = 0.944, pvalue<0.001			
CI 95% Kappa (0.934, 0.942)				CI 95% Kappa (0.942, 0.946)			

PLR2				PLR3			
	Black	White	Total		Black	White	Total
Black	22904	91	22995	Black	24010	534	24544
White	1408	25234	26642	White	302	24791	25093
Total	24312	25325	49637	Total	24312	25325	49637
(48138/49637) 96.9801%				(48801/49637) 98.3158%			
Kappa coefficient = 0.940, pvalue<0.001				Kappa coefficient = 0.970, pvalue<0.001			
CI 95% Kappa (0.936, 0.944)				CI 95% Kappa (0.968, 0.972)			

system was used because of the diagonal appearance of the man-made and natural features of the image. The result of applying the directional filter to the first component of the ICA is shown in Fig. 9(b), which shows how the linear structures are enhanced.

The classification and postprocessing are shown in Fig. 10; as with the synthetic images, the first row shows Mahalanobis (a), Majority (b), PLR2 (c), and PLR3 (d) applied to Fig. 9(a). It can be seen that the three postprocessing methods removed most of the noise from the Mahalanobis classification, but boundaries are represented very differently between the studied methods; at this level, it can also be seen that PLR3 best conserves the linear features. To appreciate this characteristic, we show the two details of Fig. 9(a): Number 1 shows a region with buildings in a diagonal disposition, and number 2 shows the diagonal intersection of two roads.

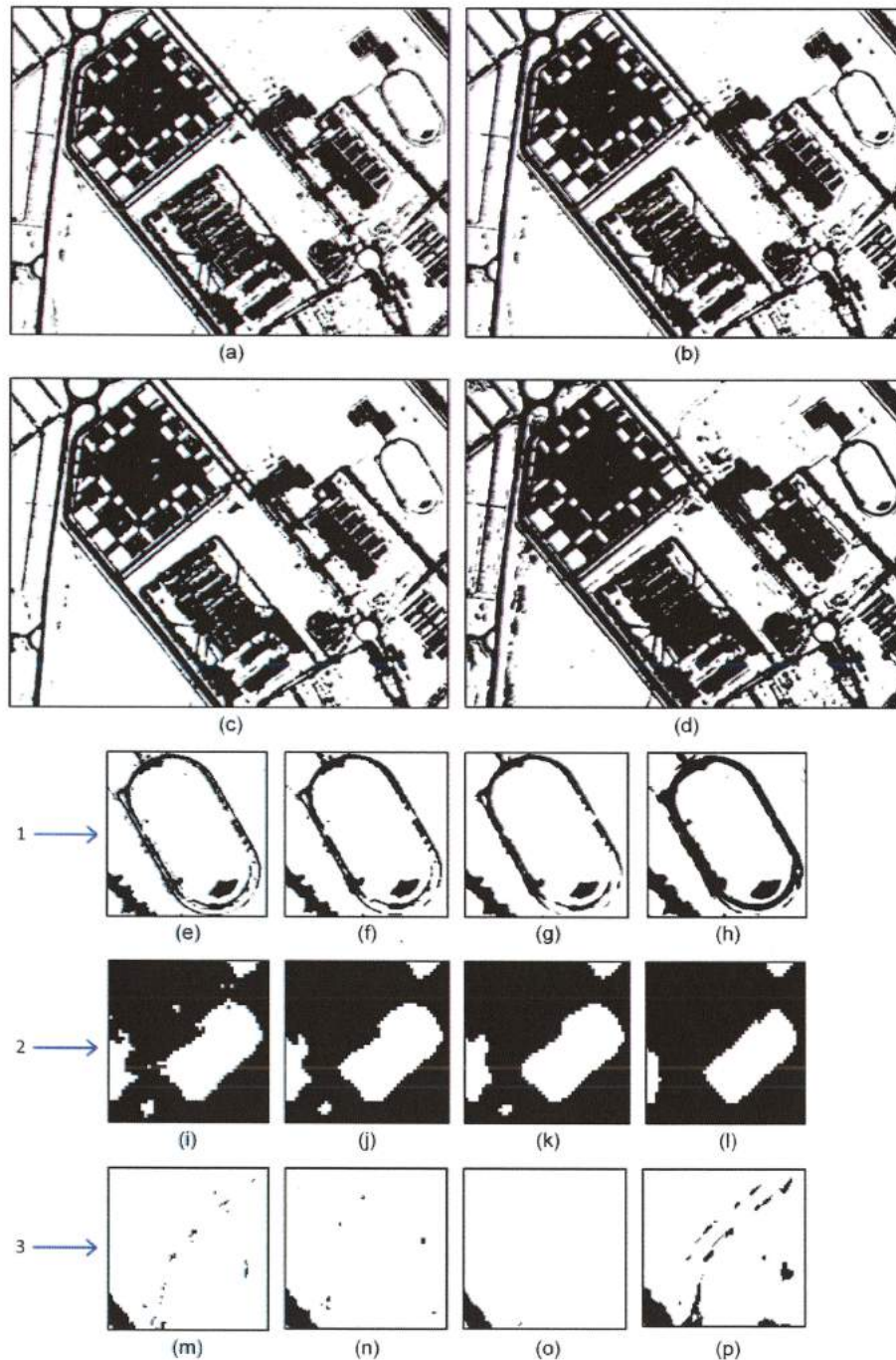


Fig. 13. Postprocessing of (a) the Mahalanobis classification with (b) Majority filter, (c) PLR2, and (d) PLR3 of the real image in Fig. 12. The other images show the results of the tested algorithms in three scenes of the image. First column [(e), (i), and (m)] shows the Mahalanobis classification, second column shows the Majority filter, third column shows the PLR2, and fourth column shows the proposed algorithm PLR3.

In the first detail, note how in Fig. 10(h), corresponding to PLR3, the large building at the center right is better delineated than in Fig. 10(e)–(g), corresponding to Mahalanobis, Majority, and PLR2, respectively. In the second detail, note how in Fig. 10(l), corresponding to PLR3, the median road is detected more clearly than in Fig. 10(i)–(k).

Apart from the visual evaluation, Table III shows the confusion matrices and p-values, which are superior for the PLR3 method although, for this case, the comparison between PLR3 and PLR2 is significant to the 95% level.

Fig. 11 shows another real image, which is this time a satellite image from the Ikonos sensor; this sensor takes images in four spectral bands with different spatial resolutions (1 m in the panchromatic mode and 4 m in the multispectral mode) from an average altitude of 681 km (revisit time is approximately three days). The image used here is a pansharpened image [42] of 1 m resolution and a size of 900×700 m, depicting part of Alcalá university campus, Madrid.

A training set was selected from Fig. 11(a), as shown in Fig. 12(a). In remote sensing classification with only two

classes, the most commonly chosen classes are man-made and natural areas. Training areas are shown in red for man-made areas and bright green for natural objects, which are mostly vegetation with some areas of bare soil. The training areas in Fig. 12(a) were extended to produce the evaluation set seen in Fig. 12(b), so different pixels are used for evaluation and training. Fig. 12(c) shows the image produced by applying the directional filter to the first ICA component from Fig. 11(a). The results of the classification are presented in Table IV. All three postprocessing methods have an accuracy and kappa coefficient superior to the initial classification by Mahalanobis distance, with the PLR3 method producing the best results. The high confidence interval and kappa value demonstrate that the PLR3 method is significantly superior to the Majority and PLR2 methods.

Mahalanobis classification of the image in Fig. 11(a) is shown in Fig. 13(a), demonstrating that most man-made areas were classified correctly. Fig. 13(b)–(d) shows the postclassification of Fig. 13(a) with Majority, PLR2, and PLR3, respectively. Note that the tennis courts and athletics track in the upper right part of Fig. 11(a) have synthetic surfaces, so they have been correctly assigned to the man-made class.

For a visual discussion of the results, three details have been selected from the classified satellite image to evaluate the goodness of the algorithm. The first detail [Fig. 11(a)-1] shows the athletics track. In Fig. 13(e), the results of the Mahalanobis classifications are shown; the Majority postprocessed image is shown in Fig. 13(f), showing some improvement such as reduced noise. Furthermore, Fig. 13(g)–(h) corresponds to PLR2 and PLR3, respectively, and shows further improvement over Majority, with reduced noise and more clearly delineated track.

The second detail [Fig. 11(a)-2] corresponds to a natural area, such as a lawn; the Mahalanobis classification of this element is shown in Fig. 13(i); the postclassification images with Majority, PLR2, and PLR3 are shown in Fig. 13(j)–(l), respectively. All three improve on the Mahalanobis classification, but the proposed PLR3 method is superior to the other methods in preserving linear structures. Finally, the third detail [Fig. 11(a)-3] corresponds to a major and a minor road; the Mahalanobis classification is shown in Fig. 13(m). The Majority [Fig. 13(n)] and PLR2 [Fig. 13(o)] blindly clean the noise, removing the minor road, while PLR3 preserved part of the diagonal linear structures, keeping and extending some of the lines delineating the minor road [Fig. 13(p)].

V. CONCLUSION

This paper has examined the use of a postclassification method to improve the supervised classification of linear structures. We compared the behavior of three methods: two pre-existing methods, Majority and PLR2, and a proposed PLR3 method, which extends PLR2 by studying groups of three pixels in the current pixel neighborhood rather than pairs.

In general contextual postclassification, it is important to remove the noise of an initial classification. Existing methods are useful in homogeneous regions, but when boundaries need to be enhanced, many problems occur with misclassified pixels at the edges of the classification regions. The goal of the proposed PLR3 method, in addition to removing classification

noise, is to correctly differentiate linear boundaries between classes.

The performance of the three methods was tested in four images: two synthetic images and two real images (an aerial and a satellite image). The use of synthetic images with full ground truth facilitated numerical analysis of the accuracy and kappa coefficient of the different methods. The use of real images was important to determine the potential of the proposed method for real situations.

The results showed that, in all cases, postclassification improved the accuracy of the initial classification by reducing image noise. The proposed PLR3 method defines linear structures better than the Majority and PLR2 methods, due to the inclusion of third-order statistics (in the sense of using triplets of neighborhood pixels) within the probabilistic likelihood calculation.

The proposed PLR3 method was used to extract linear features such as roads, sports tracks, buildings, etc., from remotely sensed aerial and satellite images; the results showed that the proposed method was a good candidate for a postclassifier. There is no single best postprocessing technique for all cases because results depend on the application at hand. Therefore, the method presented here is useful when it is important to retain lines or edges.

REFERENCES

- [1] T. Lillesand, R. Kiefer, and J. Chipman, *Remote Sensing and Image Interpretation*, 6th ed. New York: Wiley, 2008.
- [2] L. D. Robertson and D. King, "Comparison of pixel- and object-based classification in land cover change mapping," *Int. J. Remote Sens.*, vol. 32, no. 6, pp. 1505–1529, Mar. 2011.
- [3] H. R. Matinfar, F. Sarmadian, S. K. Alavi Panah, and R. J. Heck, "Comparisons of object-oriented and pixel-based classification of land use/land cover types based on Landsat 7, ETM+ spectral bands (case study: Arid region of Iran)," *Amer.-Eurasian J. Agriculture Environ. Sci.*, vol. 2, no. 4, pp. 448–456, 2007.
- [4] I. Yildirim, O. K. Ersoy, and B. Yazgan, "Improvement of classification accuracy in remote sensing using morphological filter," *Adv. Space Res.*, vol. 36, no. 5, pp. 1003–1006, 2005.
- [5] R. L. Ketting and D. A. Landgrebe, "Classification of multispectral image data by extraction and classification of homogeneous objects," *IEEE Trans. Geosci. Electron.*, vol. GE-14, no. 1, pp. 19–26, Jan. 1976.
- [6] B. Solaiman, R. K. Koffi, M. C. Mouchot, and A. Hillion, "An information fusion method for multispectral image classification postprocessing," *IEEE Trans. Geosci. Remote Sens.*, vol. 36, no. 2, pp. 395–406, Mar. 1998.
- [7] J. Stuckens, P. R. Coppin, and M. E. Bauer, "Integrating contextual information with per-pixel classification for improved land cover classification," *Remote Sens. Environ.*, vol. 71, no. 3, pp. 282–296, Mar. 2000.
- [8] J. R. Eastman, *IDRISI for Windows, User's Guide*. Worcester, MA: Clark Univ., 1995.
- [9] K. E. Kim, "Adaptive majority filtering for contextual classification of remote sensing data," *Int. J. Remote Sens.*, vol. 17, no. 5, pp. 1083–1087, 1996.
- [10] X. Jia and J. A. Richards, "Managing the spectral-spatial mix in context classification using Markov random fields," *IEEE Geosci. Remote Sens. Lett.*, vol. 5, no. 2, pp. 311–314, Apr. 2008.
- [11] A. H. S. Solberg, T. Taxt, and A. K. Jain, "A Markov random field model for classification of multisource satellite imagery," *IEEE Trans. Geosci. Remote Sens.*, vol. 34, no. 1, pp. 100–113, Jan. 1996.
- [12] A. H. S. Solberg, "Contextual data fusion applied to forest map revision," *IEEE Trans. Geosci. Remote Sens.*, vol. 37, no. 3, pp. 1234–1243, May 1999.
- [13] F. Melgani and S. B. Serpico, "A Markov random field approach to spatio-temporal contextual image classification," *IEEE Trans. Geosci. Remote Sens.*, vol. 41, no. 11, pp. 2478–2487, Nov. 2003.
- [14] D. Liu, M. Kelly, and P. Gong, "A spatial-temporal approach to monitoring forest disease spread using multi-temporal high spatial resolution imagery," *Remote Sens. Environ.*, vol. 101, no. 2, pp. 167–180, 2006.

- [15] F. Melgani, B. A. R. Al Hashemy, and S. M. R. Taha, "An explicit fuzzy supervised classification method for multispectral remote sensing images," *IEEE Trans. Geosci. Remote Sens.*, vol. 38, no. 1, pp. 287–295, Jan. 2000.
- [16] C. Benz Ursula, P. Hofmann, G. Willhauck, I. Lingenfelder, and M. Heynen, "Multi-resolution, object-oriented fuzzy analysis of remote sensing data for GIS-ready information," *ISPRS J. Photogramm. Remote Sens.*, vol. 58, no. 3/4, pp. 239–258, Jan. 2004.
- [17] S. W. Myint, P. Gober, A. Brazel, S. Grossman-Clarke, and Q. Weng, "Per-pixel vs. object-based classification of urban land cover extraction using high spatial resolution imagery," *Remote Sens. Environ.*, vol. 115, no. 5, pp. 1145–1161, 2011.
- [18] S. Geman and D. Geman, "Stochastic relaxation, Gibbs distributions and Bayesian restoration of images," *IEEE Trans. Pattern Anal. Mach. Intell.*, vol. PAMI-6, no. 6, pp. 721–741, Jun. 1984.
- [19] J. A. Richards and X. Jia, *Remote Sensing Digital Image Analysis*, 4th ed. New York: Springer-Verlag, 2006.
- [20] J. Stuckens, P. R. Coppin, and M. E. Bauer, "Integrating contextual information with per-pixel classification for improved land cover classification," *Remote Sens. Environ.*, vol. 71, no. 3, pp. 282–296, Mar. 2000.
- [21] S. Myeong, D. J. Nowak, P. F. Hopkins, and R. H. Brock, "Urban cover mapping using digital, high-spatial resolution aerial imagery," *Urban Ecosyst.*, vol. 5, no. 4, pp. 243–256, Dec. 2001.
- [22] D. J. Field, "Relations between the statistics of natural images and the response properties of cortical cells," *J. Opt. Soc. Amer.*, vol. 4, no. 12, pp. 2379–2394, Dec. 1987.
- [23] T. Pouli, D. Cunningham, and E. Reinhard, "Image statistics and their applications in computer graphics," in *Proc. STAR*, 2010, pp. 59–88.
- [24] A. Galalowitz and S. D. Ma, "Model driven synthesis of natural textures for 3-D scenes," *Comput. Graph.*, vol. 10, no. 2, pp. 161–170, 1986.
- [25] G. R. Cross and A. K. Jain, "Markov random field texture models," *IEEE Trans. Pattern Anal. Mach. Intell.*, vol. PAMI-5, no. 1, pp. 25–39, Jan. 1983.
- [26] J. A. Richards and X. Jia, "A Dempster-Shafer relaxation approach to context classification," *IEEE Trans. Geosci. Remote Sens.*, vol. 45, no. 5, pp. 1422–1431, May 2007.
- [27] G. J. McLachlan, "Mahalanobis distance," *Resonance*, vol. 4, no. 6, pp. 20–26, 1999.
- [28] M. Marghany and M. Hashim, "Comparison between Mahalanobis classification and neural network for oil spill detection using RADARSAT-1 SAR data," *Int. J. Phys. Sci.*, vol. 6, no. 3, pp. 566–576, Feb. 2011.
- [29] K. Perumal and R. Bhaskaran, "Supervised classification performance of multispectral images," *J. Comput.*, vol. 2, no. 2, pp. 124–129, Feb. 2010.
- [30] B. Rodríguez-Cuenca, *Clasificación de imágenes con aplicación del contexto*, Proyecto Fin de Carrera, Universidad de Alcalá, Spain, 2010.
- [31] S. Zucker and J. Mohammed, "Analysis of probabilistic relaxation labeling processes," in *Proc. IEEE Conf. Pattern Recog. Image Process.*, Chicago, IL, 1978, pp. 307–312.
- [32] D. A. Landgrebe, "The development of a spectral-spatial classifier for Earth observational data," *Pattern Recog.*, vol. 12, no. 3, pp. 165–175, 1980.
- [33] J. A. Richards, D. A. Landgrebe, and P. H. Swain, "A means for utilizing ancillary information in multispectral classification," *Remote Sens. Environ.*, vol. 12, no. 6, pp. 463–477, Dec. 1982.
- [34] A. Galalowitz, "A new method for texture field synthesis: Some applications to study of human vision," *IEEE Trans. Pattern Anal. Mach. Intell.*, vol. PAMI-3, no. 5, pp. 520–533, Sep. 1981.
- [35] A. Galalowicz, "Texture modeling applications," *Vis. Comput.*, vol. 3, no. 4, pp. 186–200, 1987.
- [36] A. Hyvärinen, J. Karhunen, and E. Oja, *Independent Component Analysis*. New York: Wiley, 2001.
- [37] C. I. Chang, S. S. Chiang, J. A. Smith, and I. W. Ginsberg, "Linear spectral random mixture analysis for hyperspectral imagery," *IEEE Trans. Geosci. Remote Sens.*, vol. 40, no. 2, pp. 375–392, Feb. 2002.
- [38] X. Zhang and C. H. Chen, "New independent component analysis method using high order statistics with application to remote sensing images," *Opt. Eng.*, vol. 41, no. 7, pp. 1717–1728, Jul. 2002.
- [39] H. Shahbazi, P. Kabiri, and M. Soryani, "Content based multispectral image retrieval using independent component analysis," in *Proc. Congr. Image Signal Process.*, 2008, pp. 485–489.
- [40] M. S. Karoui, Y. Deville, S. Hosseini, A. Ouamri, and D. Ducrot, "Improvement of remote sensing multispectral image classification by using independent component analysis," in *Proc. 1st WHISPERS*, 2009, pp. 1–4.
- [41] Q. Du, I. Kopriva, and H. Szu, "Independent-component analysis for hyperspectral remote sensing imagery classification," *Opt. Eng.*, vol. 45, no. 1, pp. 170081-1–170081-3, 2006.
- [42] J. A. Malpica, "Hue adjustment to IHS pan-sharpened IKONOS imagery for vegetation enhancement," *IEEE Int. J. Geosci. Remote Sens. Lett.*, vol. 4, no. 1, pp. 27–31, Jan. 2007.



Borja Rodríguez-Cuenca (S'12) was born in Gijón, Spain, in 1987. He received the B.S. degree in topography from the University of Oviedo, Oviedo, Spain, in 2008 and the M.S. degree in geodesy and cartography from the University of Alcalá, Alcalá de Henares, Spain, in 2010, where he is currently working toward the Ph.D. degree.



Jose A. Malpica received the M.S. and Ph.D. degrees in mathematics from Complutense University of Madrid, Madrid, Spain, in 1981 and 1992, respectively.

From 1998 to 2004, he was the Dean of the School of Cartography and Geodesy, University of Alcalá, Alcalá de Henares, Spain. He is currently an Associate Professor with the Department of Mathematics, University of Alcalá. Recently, he has also been actively involved in mathematics modeling for remote sensing phenomena, working in the Geodesy and Cartography Research Team of Alcalá. His current research interests are in multispectral and hyperspectral image analysis, neural network, and genetic algorithms with focus on feature extraction applications.



Maria C. Alonso received the B.S. and M.S. degrees in management science and statistics from Complutense University of Madrid, Madrid, Spain, in 1983 and 1985, respectively, and the Ph.D. degree in mathematics from the University of Alcalá, Alcalá de Henares, Madrid, Spain, in 2003.

She is currently an Associate Professor with the Department of Mathematics, University of Alcalá. She has performed statistics consulting for industry, and she has worked on many projects involving pattern recognition for satellite image analysis. For the last 15 years, she has been working in the Geodesy and Cartography Research Team of Alcalá.

CHAPTER 5

Conclusions and future work

*Someday we'll look back on this
and it will all seem funny.*

Bruce Springsteen

As can be seen in former chapters, for every single research carried out in this thesis there have been summarized its particular reached conclusions. Besides, in order to emphasize the main concluded novelties resolutions, in the current 5th Chapter entitled “Conclusions and future work” both general resolutions learned during the implementation of the whole thesis and those that have been achieved in the development of every piece of particular research are collected and synthesized.

- *C1: Segmentation, grouping and data structure pre-processing methods are useful to facilitate and speed up the subsequent/following procedures for the treatment and analysis of remote sensing data*

Geospatial data provided by remote sensing sensors, either in raster format or point cloud structure, are very dense, and processing can be costly in terms of computing time and computing. During the research presented in this thesis, it has been proven that optimizing the analysis and processing operations of geospatial data, requires proper structure to avoid unnecessary waiting time and computational efforts. The work presented in this thesis has discarded the application of algorithms at pixel/point level in big data due to the computational complexity that this entails. Aiming to optimize the methodologies to be applied to remotely sensed data it has been observed the convenience of using algorithms that group elements with common characteristics, moving from an individual level, either pixel or point, to a region or super pixel level.

In the pre-processing step of the method presented in “Semi-automatic detection of swimming pools from aerial high-resolution images and LIDAR data” [81], a region-growing segmentation of the aerial image is carried out, which allows working with groups of pixels with similar properties instead of working with isolated elements. An alternative to segmentation for those works in which 3D point clouds are involved is the creation of regions of interest, deleting those parts of the cloud that are not relevant to the current work. In the paper entitled “An approach to detect and delineate street curbs from MLS 3D point cloud data,” to ease and speed up the following procedures, the point cloud was projected onto 2D surfaces, similar to raster images. Another possibility to improve the management of the point cloud is the one presented in [73], in which the point cloud is organized in a pillar structure, which is more easily usable than the raw data.

- *C2: 3D ALS and MLS point clouds serve to complement the 2D information contained in aerial and satellite imagery, both in terms of z-coordinate and spatial resolution*

Aerial and satellite images provide high spatial and spectral resolution information, useful in disciplines including territorial analysis and urban policy making. Raster images, however, have important limitations due to their acquisition characteristics: aerial and satellite images register planimetric information but do not directly provide altimetric information. The lack of z-coordinate information may prevent proper identification of certain land covers such as building and trees.

3D information provided by airborne laser scanner sensors complements multi- and hyperspectral aerial raster imagery information. This thesis has proven the utility of merging ALS data with multispectral imagery to update ground cover databases. In the article entitled "Semi-automatic detection of swimming pools from high-resolution aerial images and LIDAR data" [81] the inclusion of LIDAR data in the land cover recognition procedure allowed the generation of a normalized digital surface model (nDSM), which facilitated the discrimination of natural vegetation cover and human constructions.

Furthermore, terrestrial point clouds, both TLS and MLS, allow work to be carried out in greater detail, which is hardly achievable from aerial geospatial information. TLS sensors also have the advantage that point cloud measurement is not affected by weather or lighting conditions. The papers on street curbs and pole-like objects both noted/demonstrated the ability of MLS sensors to effectively extract precise details of street furniture, trees, and roadsides.

- *C3: Desirability of the availability of a dataset and ground truth validation set to quantify the efficiency and robustness of novel and existing methodologies and make reliable comparisons in a common framework*

One of the main goals of remote sensing research is the development of robust algorithms capable of obtaining precise and accurate results in all conditions. During the development of the research presented in this thesis, it has been noted the difficulty of generating methodologies to provide acceptable accuracy

rates in any work area regardless of the sensor's characteristics. In the current literature, there are several methodologies and approaches for extracting and classifying land covers and urban furniture. Some authors have made important efforts to check the validity and robustness of their methods and to test their effectiveness in data measured by diverse sensors and representing a wide variety of possible coverage and urban settings. However, the fact of not having a common dataset where the various existing algorithms can be applied and validated makes the certification and comparison of different methodologies difficult. To validate their methods, authors must make their own ground truth, by visually exploring data and making field visits when the photo interpretation is uncertain. A common dataset and ground truth would save authors trying to validate their methods a great deal of time.

- *C4. It is necessary to develop a method for detecting and removing shadows in aerial and satellite images before any classification procedure in order to avoid land covers misallocation.*

The shadows cast by high elements such as buildings or trees modify the spectral response of land covers in multispectral images and hinder their proper extraction from geospatial data. To avoid this effect, geospatial data acquisition from aerial platforms is commonly carried out during the summer and in the middle hours of the day, when the sun is close to its zenith. However, despite this effort to minimize the presence of shadows on the scene, their existence on aerial and satellite images is inevitable and cause subsequent errors in classification procedures. Thus, to minimize and remove these errors, every method for extracting and classifying land covers should take the effect of shadows into account and propose a solution to eliminate these procedural errors. The article "Semi-automatic detection of swimming pools from aerial high-resolution images and LIDAR data" [81] used the method implemented by our research group (Alejandro Martinez de Agirre and Jose Antonio Malpica) in the paper entitled "Detection of shadows in high-resolution images using LIDAR technology" [82]. This method can estimate the existing shadows in an aerial

image from the sun's position and the aerial platform at the time of taking the image and enables the classification procedure to reclassify those regions mistakenly classified as shadowed areas.

- *C5. Fuzzy logic is a real alternative, in terms of accuracy and robustness, to supervised and unsupervised classification algorithms in the extraction and classification of ground covers*

Traditionally, image classification procedures have been carried out through supervised and unsupervised classification algorithms. The main drawback of these methods is the need of additional *a priori* information about the input data and characteristics of the considered classes. This thesis analyzed the performance of fuzzy logic in image classifications procedures. Specifically, the Dempster-Shafer evidence theory has been studied. Just like a traditional classifier, fuzzy logic is not an automatic procedure but a semi-automatic one because each decision index must be assigned masses of belonging to each of the considered categories depending on its value. Results provided by fuzzy logic have been compared with the ones obtained using Mahalanobis distance and SVM, one of the most precise supervised classification algorithms. Dempster-Shafer achieved better results than the Mahalanobis classifier and overall accuracy rates comparable to SVM, with a 99.86% in Dempster-Shafer and a 99.87% in SVM. Thus, it can be concluded that fuzzy logic is a real alternative to supervised and unsupervised algorithms in image classification procedures.

- *C6. ALS intensity pulse return as an efficient descriptor of certain land covers*

Multi- and hyperspectral images provide information on different wavelengths of the electromagnetic spectrum, which is useful information to generate descriptors for classification processes. Regarding laser scanner sensors, although they are not capable of recording spectral information, they can record the return intensity of the emitted laser pulses. This information is useful for extracting certain entities that have a characteristic behavior in this variable,

such as bodies of water, roads, or road signs. Laser return intensity values depend on the laser scanner's calibration and the way in which the measuring device encodes the results. Thus, despite its utility, it is difficult to automatize those procedures involving intensity return. In "Semi-automatic detection of swimming pools from high-resolution aerial images and LIDAR data" [81], LIDAR intensity has been used to discriminate paved surfaces, due to the low-intensity signal in these surfaces. It also noted the ability of LIDAR intensity returns to detect bodies of water, due to the short LIDAR reflectivity in those coverages.

- *C7. The importance of the neighborhood and geometric variables as descriptors in classification and entity extraction procedures in 3D point clouds.*

Traditionally, image classification algorithms use the spectral information contained in the different bands of multispectral images as category descriptors. Sometimes, context descriptors such as texture or roughness are used as descriptors. The computing of these variables is based on the study of every pixel of the image and its neighborhoods. Because laser scanner sensors just record geometric data without spectral information, analysts and researchers must develop decision indices different than those commonly used in multispectral imagery. Generally, these indices are based on geometric variables calculated for each point from all the points contained in a certain neighborhood (a neighborhood is a sphere centered on the studied point). It is important to establish the appropriate size of a neighborhood. A small neighborhood may not consider enough points necessary to calculate the geometric variables, and large vicinity can generate unaffordable processing times. A previous study is suitable to decide the proper size of the neighborhood based on the density of the cloud to achieve a useful extraction. In the work presented in "Automatic Detection and Classification of Pole-Like Objects in Urban Point Cloud Data Using an Anomaly Detection Algorithm" [73], an index has been developed that allows the extraction of horizontal and vertical surfaces, as well as the reconstruction

of the trajectory followed by the MLS. This index is calculated from two geometric features of the cloud, the roughness and the normal vector. This work included an analysis of the behavior of the developed geometric index with different neighborhood sizes. Thus, it is possible to determine the optimal size that allows a correct extraction with an acceptable processing time.

- *C8. It is important to properly plan the MLS data measurement in order to avoid unwanted occlusions in the cloud during the registration process and the need for development methods to estimate hidden items.*

MLS sensors are capable of recording the (x, y, z) coordinates of millions of points, thereby creating a 3D model. However, just as in aerial images with wooded areas that hinder the vision of the ground, in point clouds some regions are not represented in the 3D point cloud. This effect is due to occlusions produced by obstacles, both stationary and moving (cars, pedestrians, trees, or containers), which are interposed between the sensor and the reality being measured. These occlusions mean that some target elements could appear partially or wholly hidden in the cloud, which makes their proper detection impossible. It is important to take this issue into account at the time of planning fieldwork and take actions to minimize the occluded areas in the cloud. Some measures to consider are performing more than one scanning measurement in the studied area, installing several laser scanner sensors in the vehicle to record information from different perspectives, or carrying out the cloud's registration when car traffic and pedestrians are sparse. However, despite proper planning of data collection, the presence of certain occlusions in the point cloud is inevitable, such as those caused by fixed elements in the street. Therefore, it is desirable to develop extraction and classification methods smart enough to estimate what can happen in these hidden areas and what elements can exist in reality even without being present in the cloud. The work "An approach to detect and delineate street curbs from MLS 3D point cloud data" has developed a method to estimate the location of those existing curbs on the street that are

hidden by fixed and moving obstacles, such as containers or vehicles parked in the driveway.

- *C9. Post-classification procedures are necessary to remove noise and improve the results of classification methods*

In addition to false positive and false negative errors, image classification algorithms generally produce noise that reduces the quality of the final work. This noise is known as salt-and-pepper effect and is shown as isolated misclassified pixels in homogeneous regions. It is important to implement post-classification techniques to improve classification quality and eliminate those errors generated in the procedure as much as possible. Generally, post-classification procedures do not consider spectral properties but contextual information. The label and the context information (category of neighboring elements) for every picture element (pixel or regions) are studied. The algorithm decides, depending on context labeling, if the studied element preserves its category or if a new label is assigned to the studied entity. The work presented in the paper "A spatial contextual post-classification method for preserving linear objects in multispectral imagery" [83] developed a method to eliminate the noise generated in the classification process. Additionally, this method can define linear structures that have been lost during the classification process.

- *C10. Working with synthetic images in the algorithm design phase allows to refine the methodology prior to its application in real images/cases*

Aerial and satellite images represent large areas of land where there are elements of diverse nature and heterogeneous characteristics. It is necessary to create an accurate ground truth to evaluate the performance of image processing and analysis algorithms in this type of geospatial data. Generating a ground truth is not a trivial task and requires high economic and temporal effort. The quality of a generated ground truth depends on the quality of the geospatial reference data input and the expertise of the photo interpreter. In many cases, ground truth generation requires field visits to complete the geospatial

information, further increasing the economic and temporal cost of the procedure. The use of synthetic images whose size, distribution, and number of bands is perfectly controlled by the user is useful to analyze the theoretical behavior and post-classification sorting algorithms in user-controlled situations. In the work "A spatial contextual post-classification method for preserving linear objects in multispectral imagery," a series of synthetic images have been created to study and evaluate, under controlled conditions, the theoretical behavior of a developed post-classification algorithm.

- *C11. Anomaly detection algorithms, traditionally used in hyperspectral imagery, can be successfully used in the detection of elements of interest in 3D point clouds.*

Supervised classification processes carry out what is known as target detection. From input information used to train the classification algorithm, these algorithms perform a classification of those elements with certain distinct spectral and spatial characteristics of other considered categories. The need for training hinders the automation of such classifications.

Another way of extracting and classifying cartographic entities is known as anomaly detection. Sometimes the statistical behavior of some classes is different from the average behavior of all other categories of the set, placing the first classes in the tails of the statistical descriptors. Anomaly detection consists of finding those elements located in the distribution tails whose behavior differs from the rest. This form of extraction does not need initial training information, which is an advantage when automating classification processes. Generally, anomaly detection algorithms are used in hyperspectral imaging, but the article "Automatic detection and classification of pole-like objects in urban point cloud data use an anomaly detection algorithm" [73] has proven the usefulness of the RX anomaly detection algorithm to detect vertical street furniture in 3D point clouds.

Future Work: the following paragraphs briefly discuss the open lines of study remaining after the completion of this thesis work, and through which future research will be directed.

- *FW1. Optimization of developed methodologies in order to reduce waiting times, opening the door for the land covers extraction in large scale production processes.*

One of the weaknesses of processing and analysis methodologies of geospatial information are the long waiting times that require these processes, mainly due to the high volume of digital memory occupied by remotely sensed data. Future research will attempt to reduce the waiting times, optimizing the methodologies proposed for the extraction of urban elements for its possible use in large scale production processes and generating real-time results.

- *FW2. Study the possibility of including hyperspectral images and multitemporal information both in extraction and classification developed methods and their influence on the final accuracy.*

The ability to add geospatial information measured at different times in order to perform multi-temporal analysis will be studied. Thus, it would be possible to detect those land covers that have experienced changes over time. Similarly, the inclusion of hyperspectral imagery will be deemed. These images provide continuous information in the electromagnetic spectrum, which could be useful in detecting and classifying a larger number of urban entities and land covers.

- *FW3. Future research will attempt to merge multispectral data with MLS and TLS point clouds and consider the use of 3D point clouds obtained by photogrammetric methods.*

Aerial and satellite multi- and hyperspectral images contain spectral and contextual information that can perform classification procedures by using descriptor indexes such as NDVI. In point clouds recorded by a terrestrial laser scanner, both MLS and TLS, spectral information is not available. Geometric properties of the cloud, such as roughness or curvature, are calculated to carry

out processes of classification and entity extraction. It would be interesting to combine the 3D point cloud with the multispectral image information to obtain (x, y, z) coordinates for each point and information at different wavelengths of the electromagnetic spectrum. Some laser sensors take images at the same moment when the laser scanning is performed, allowing an RGB value to be assigned to each point of the cloud. Having information in other spectrum wavelengths, such as the middle and near-infrared, would facilitate the detection of land covers and urban furniture from point clouds.

In recent times, the use of point clouds obtained by photogrammetric methods (from several images taken from different points of view) has been imposed to those recorded by laser scanner sensors because photogrammetric point clouds provide 3D information with spatial accuracy similar to MLS and TLS clouds, but with a more economically efficient acquisition process. In addition, photogrammetric clouds include spectral information (usually in the RGB bands, which are those in which photogrammetric cameras take in information). In future works, the developed methodologies will be adapted to photogrammetric point clouds and new methodologies for these types of point clouds will be developed, whose multispectral information could be useful in pattern recognition tasks.

- *FW4. Inclusion of other descriptors in extraction and classification procedures, as the LIDAR intensity for traffic signs.*

In the course of the work presented in this thesis, it has been observed that the behavior of the LIDAR pulse intensity return is sensitive to the properties of the material on which the laser is reflected. LIDAR intensity has been used in the work titled "Semi-automatic detection of swimming pools from high-resolution aerial images and LIDAR data" [81] for extracting asphalt floors from ALS data, but it has been noted that this property has greater potential for detecting other features from 3D MLS point clouds, such as horizontal and vertical traffic signs. In future research, the LIDAR intensity will be included

as a descriptor of other urban features not considered in the current work. A small preview of this planned future work has been implemented and recently presented in the paper entitled “Extracción de señalización horizontal en entornos urbanos a partir de nubes de puntos tridimensionales” [75].

- *FW5. Feasibility study of the uses and capacities of LIDAR full waveform.*

In recent research works [84, 85] LIDAR full waveform is beginning to be used instead of the discrete LIDAR that had been used so far. This brand new LIDAR, capable of detecting 256 returns for each emitted pulse, captures vertical information substantially continuously along the pulse. The main drawback is that the size of the point cloud exponentially increases, which difficult the treatment of these data. But as positive part, they can provide useful information for extracting buildings or the study of plant mass that were not available until now. The feasibility of its use will be studied and, if it is positive, its use will be considered for inclusion in extraction and classification procedures.

Bibliography

*Dicebat Bernardus Carnotensis
nos esse quasi nanos, gigantium humeris incidentes,
ut possimus plura eis et remotiora videre,
non utique proprii visus acumine, aut eminentia corporis,
sed quia in altum subvenimur et extollimur magnitudine gigantea*

*Somos como enanos sobre los hombros de gigantes
podemos ver más, y más lejos que ellos,
no por la agudeza de nuestra vista, ni por la altura de nuestro cuerpo,
sino porque somos levantados por su gran altura.*

Bernardo de Chartres

Research papers and scientific books detailed in this section are referred to those citations included in this thesis work, with the exception of cites included in each paper.

- [1] S. C. Holland and D. A. Plane, "Methods of mapping migration flow patterns," *Southeastern Geographer*, vol. 41, pp. 89-104, 2001.
- [2] C. R. Sluter, C. B. M. Cruz, and P. M. L. de Menezes, *Cartography-Maps Connecting the World*: Springer, 2015.

- [3] S. Holmberg, "Geoinformatics for urban and regional planning," *Environment and Planning B*, vol. 21, pp. 5-5, 1994.
- [4] F. Joly, *La cartographie* vol. 34: Presses universitaires de France, 1976.
- [5] J. P. Snyder, *Map projections--A working manual* vol. 1395: US Government Printing Office, 1987.
- [6] T. M. Lillesand and R. W. Kiefer, "Remote Sensing and Image Interpretation. John Willey & Sons," *Inc, United States of America*, 1994.
- [7] R. A. Schowengerdt, *Remote sensing: models and methods for image processing*: Academic press, 2006.
- [8] J. R. Jensen, *Remote sensing of the environment: An earth resource perspective*: Pearson Education India, 2009.
- [9] S. L. Ustin, "Remote sensing of environment: State of the science and new directions," *Remote Sensing of Natural Resources Management and Environmental Monitoring*, 2004.
- [10] D. S. Wilkie and J. T. Finn, *Remote sensing imagery for natural resources monitoring: a guide for first-time users*: Columbia University Press, 1996.
- [11] J. R. Jensen and K. Lulla, "Introductory digital image processing: a remote sensing perspective," 1987.
- [12] R. C. Gonzalez and R. E. Woods, "Digital image processing," ed: Prentice Hall New Jersey, 2002.
- [13] P. Teillet, K. Staenz, and D. William, "Effects of spectral, spatial, and radiometric characteristics on remote sensing vegetation indices of forested regions," *Remote sensing of Environment*, vol. 61, pp. 139-149, 1997.
- [14] M. Labrador García, J. Évora Brondo, and M. Arbelo Pérez, "Satélites de Teledetección para la gestión del territorio," *La Laguna, Spain: Consejería de Agricultura, Ganadería, Pesca y Aguas del Gobierno de Canarias*, 2012.
- [15] J. Gao, "A comparative study on spatial and spectral resolutions of satellite data in mapping mangrove forests," *International Journal of Remote Sensing*, vol. 20, pp. 2823-2833, 1999.
- [16] Y. Du, P. M. Teillet, and J. Cihlar, "Radiometric normalization of multitemporal high-resolution satellite images with quality control for land cover change detection," *Remote sensing of Environment*, vol. 82, pp. 123-134, 2002.
- [17] L. G. Brown, "A survey of image registration techniques," *ACM computing surveys (CSUR)*, vol. 24, pp. 325-376, 1992.
- [18] G. V. Vosselman and H.-G. Maas, *Airborne and terrestrial laser scanning*: Whittles, 2010.

- [19] J. Shan and C. K. Toth, *Topographic laser ranging and scanning: principles and processing*. CRC press, 2008.
- [20] N. Haala and C. Brenner, "Extraction of buildings and trees in urban environments," *ISPRS Journal of Photogrammetry and Remote Sensing*, vol. 54, pp. 130-137, 1999.
- [21] A.-H. Granholm, H. Olsson, M. Nilsson, A. Allard, and J. Holmgren, "The potential of digital surface models based on aerial images for automated vegetation mapping," *International Journal of Remote Sensing*, vol. 36, pp. 1855-1870, 2015.
- [22] L. Waser, E. Baltsavias, K. Ecker, H. Eisenbeiss, E. Feldmeyer-Christe, C. Ginzler, M. Küchler, and L. Zhang, "Assessing changes of forest area and shrub encroachment in a mire ecosystem using digital surface models and CIR aerial images," *Remote sensing of Environment*, vol. 112, pp. 1956-1968, 2008.
- [23] Z. Li, C. Zhu, and C. Gold, *Digital terrain modeling: principles and methodology*. CRC press, 2004.
- [24] L. Gonçalves-Seco, D. Miranda, R. Crecente, and J. Farto, "Digital terrain model generation using airborne LiDAR in a forested area Galicia, Spain," in *Proceedings of 7th International symposium on spatial accuracy assessment in natural resources and environmental sciences*, 2006, pp. 169-180.
- [25] C. Briese and N. Pfeifer, "Airborne laser scanning and derivation of digital terrain models," in *Fifth Conference on Optical*, 2001.
- [26] E. Næsset, "Vertical Height Errors in Digital Terrain Models Derived from Airborne Laser Scanner Data in a Boreal-Alpine Ecotone in Norway," *Remote Sensing*, vol. 7, pp. 4702-4725, 2015.
- [27] J.-S. Bailly, G. Sofia, N. Chehata, P. Tarolli, and F. Levavasseur, "Farmland terrace slope detection from Pleiades digital elevation models," in *EGU General Assembly Conference Abstracts*, 2015, p. 10021.
- [28] S. P. García and M. M. Rodríguez, "A geospatial indicator for assessing urban panoramic views," *Computers, Environment and Urban Systems*, vol. 49, pp. 42-53, 2015.
- [29] S. Zazo, J.-L. Molina, and P. Rodríguez-Gonzálvez, "Analysis of flood modeling through innovative geomatic methods," *Journal of Hydrology*, vol. 524, pp. 522-537, 2015.
- [30] A. Günay, H. Arefi, and M. Hahn, "True Orthophoto production using Lidar data," in *Joint Workshop" Visualization and Exploration of Geospatial Data"*, *International Archives of Photogrammetry, Remote Sensing and Spatial Information Sciences*, 2007, p. 4.

- [31] A. Georgopoulos, M. Tsakiri, C. Ioannidis, and A. Kakli, "Large scale orthophotography using DTM from terrestrial laser scanning," *The International Archives of the Photogrammetry, Remote Sensing and Spatial Information Sciences*, vol. 35, pp. 467-472, 2004.
- [32] D. Morgan and E. Falkner, *Aerial mapping: methods and applications*: CRC Press, 2001.
- [33] W. Schickier and A. Thorpe, "Operational procedure for automatic true orthophoto generation," *International Archives of Photogrammetry and Remote Sensing*, vol. 32, pp. 527-532, 1998.
- [34] F. Amhar, J. Jansa, and C. Ries, "The generation of true orthophotos using a 3D building model in conjunction with a conventional DTM," *International Archives of Photogrammetry and Remote Sensing*, vol. 32, pp. 16-22, 1998.
- [35] C. Balletti, F. Guerra, A. Lingua, and F. Rinaudo, "True digital orthophoto of the San Marco Basilica in Venice," *International archives of Photogrammetry, Remote Sensing and Spatial Information Sciences*, vol. 34, pp. 43-48, 2003.
- [36] A. Arozarena, G. Villa, and N. Valcárcel, "The National Aerial Orthophoto Program in Spain (PNOA)," in *International Cartographic Conference. La Coruña, Spain*, 2005.
- [37] V. Maliene, V. Grigonis, V. Palevičius, and S. Griffiths, "Geographic information system: Old principles with new capabilities," *Urban Design International*, vol. 16, pp. 1-6, 2011.
- [38] O. Huisman and R. de By, "Principles of geographic information systems," *ITC Educational Textbook Series*, vol. 1, 2009.
- [39] F. J. Pierce and D. Clay, *GIS applications in agriculture*: CRC Press, 2007.
- [40] G. C. Sabou, "GIS Applications for an Effective Heritage Tourism Management in Romania," *International Journal of Economic Practices and Theories*, vol. 5, pp. 136-141, 2015.
- [41] B. Das and D. Kumar, "Recent Trends in GIS Applications," *Available at SSRN 2609707*, 2015.
- [42] F. Tanser and D. Le Sueur, "The application of geographical information systems to important public health problems in Africa," *International Journal of Health Geographics*, vol. 1, p. 9, 2015.
- [43] S. Madden, "From databases to big data," *IEEE Internet Computing*, pp. 4-6, 2012.
- [44] Y. Ma, H. Wu, L. Wang, B. Huang, R. Ranjan, A. Zomaya, and W. Jie, "Remote sensing big data computing: Challenges and opportunities," *Future Generation Computer Systems*, vol. 51, pp. 47-60, 2015.

- [45] M. Gianinetto and M. Scaioni, "Automated geometric correction of high-resolution pushbroom satellite data," *Photogrammetric Engineering & Remote Sensing*, vol. 74, pp. 107-116, 2008.
- [46] D. V. Fedorov, L. M. Fonseca, C. Kenney, and B. S. Manjunath, "Automatic registration and mosaicking system for remotely sensed imagery," in *International Symposium on Remote Sensing*, 2003, pp. 444-451.
- [47] T. M. Mitchell, "Machine learning. WCB," ed: McGraw-Hill Boston, MA:, 1997.
- [48] E. Mjolsness and D. DeCoste, "Machine learning for science: state of the art and future prospects," *Science*, vol. 293, pp. 2051-2055, 2001.
- [49] J. A. Richards and X. Jia, *Remote sensing digital image analysis* vol. 3: Springer, 1999.
- [50] R. O. Duda, P. E. Hart, and D. G. Stork, *Pattern classification*: John Wiley & Sons, 2012.
- [51] F. Melgani and L. Bruzzone, "Classification of hyperspectral remote sensing images with support vector machines," *IEEE Transactions on Geoscience and Remote Sensing* vol. 42, pp. 1778-1790, 2004.
- [52] P. M. Atkinson and A. Tatnall, "Introduction neural networks in remote sensing," *International Journal of Remote Sensing*, vol. 18, pp. 699-709, 1997.
- [53] G. H. Ball and D. J. Hall, "ISODATA, a novel method of data analysis and pattern classification," DTIC Document 1965.
- [54] J. MacQueen, "Some methods for classification and analysis of multivariate observations," in *Proceedings of the fifth Berkeley symposium on mathematical statistics and probability*, 1967, pp. 281-297.
- [55] C. Hooge, "Fuzzy logic Extends Pattern Recognition Beyond Neural Networks," *Vision Systems Design*, pp. 32-37, 1998.
- [56] L. A. Zadeh, "The role of fuzzy logic in the management of uncertainty in expert systems," *Fuzzy sets and systems*, vol. 11, pp. 197-198, 1983.
- [57] G. Klir and B. Yuan, *Fuzzy sets and fuzzy logic* vol. 4: Prentice Hall New Jersey, 1995.
- [58] V. Chandola, A. Banerjee, and V. Kumar, "Anomaly detection: A survey," *ACM computing surveys (CSUR)*, vol. 41, p. 15, 2009.
- [59] I. S. Reed and X. Yu, "Adaptive multiple-band CFAR detection of an optical pattern with unknown spectral distribution," *IEEE Transactions on Acoustics, Speech and Signal Processing* vol. 38, pp. 1760-1770, 1990.
- [60] D. Manolakis and G. Shaw, "Detection algorithms for hyperspectral imaging applications," *Signal Processing Magazine, IEEE*, vol. 19, pp. 29-43, 2002.
- [61] A. Meyer-Baese and V. J. Schmid, *Pattern Recognition and Signal Analysis in Medical Imaging*: Elsevier, 2014.

- [62] K. Varmuza, *Pattern recognition in chemistry* vol. 21: Springer Science & Business Media, 2012.
- [63] (24 November 2015). *City of Melbourne: Street Furniture Plan*. Available: https://www.melbourne.vic.gov.au/AboutCouncil/PlansandPublications/strategies/Documents/street_furniture_plan.PDF
- [64] (24 November 2015). *Toronto: Coordinated Street Furniture Program*. Available: <http://www.toronto.ca/legdocs/mmis/2015/pw/bgrd/backgroundfile-80110.pdf>
- [65] J. Aschbacher and M. P. Milagro-Pérez, "The European Earth monitoring (GMES) programme: Status and perspectives," *Remote sensing of Environment*, vol. 120, pp. 3-8, 2012.
- [66] M. Bossard, J. Feranec, and J. Otahel, "CORINE land cover technical guide: Addendum 2000," ed: European Environment Agency Copenhagen, 2000.
- [67] G. Büttner, J. Feranec, G. Jaffrain, L. Mari, G. Maucha, and T. Soukup, "The CORINE land cover 2000 project," *EARSeL eProceedings*, vol. 3, pp. 331-346, 2004.
- [68] G. Villa, A. Arozarena, I. del Bosque, N. Varcárcel, C. García, and M. Solís, "El Plan Nacional de Observación del Territorio en España," in *XI Congreso Nacional de Teledetección, Puerto de la Cruz*, 2005, pp. 21-23.
- [69] A. Arozarena, G. Villa, N. Valcárcel, E. Caballero, and A. Porcuna, "Sistema de información de ocupación del suelo en España (SIOSE) como proyecto integrado en el plan nacional de observación del territorio," in *Información espacial y nuevas tendencias en las tecnologías de la información geográfica (TIGs)*, 2007, pp. 295-308.
- [70] B. Rodríguez-Cuenca, J. A. Malpica, and M. C. Alonso, "Region-growing segmentation of multispectral high-resolution space images with open software," in *IEEE International Geoscience and Remote Sensing Symposium (IGARSS)*, 2012, pp. 4311-4314.
- [71] B. Rodríguez-Cuenca, M. Alonso-Rodríguez, E. Domenech-Tofiño, N. Valcárcel-Sanz, J. Delgado-Hernández, J. Peces-Morera, and A. Arozarena-Villar, "Procedure to detect impervious surfaces using satellite images and light detection and ranging (LIDAR) data," in *SPIE Remote Sensing*, 2014, pp. 924414-924414-9.
- [72] B. Rodríguez-Cuenca, M. C. Alonso, and A. Tamés-Noriega, "LULC database updating from VHR images and LIDAR data using evidence theory," in *2015 Conference of the International Fuzzy Systems Association and the European Society for Fuzzy Logic and Technology (IFSA-EUSFLAT-15)*, 2015.

- [73] B. Rodríguez-Cuenca, S. García-Cortés, C. Ordóñez, and M. C. Alonso, "Automatic Detection and Classification of Pole-Like Objects in Urban Point Cloud Data Using an Anomaly Detection Algorithm," *Remote Sensing*, vol. 7, pp. 12680-12703, 2015.
- [74] B. Rodríguez-Cuenca, S. García-Cortés, C. Ordóñez, and M. C. Alonso, "A study of the roughness and curvature in 3D point clouds to extract vertical and horizontal surfaces," in *Geoscience and Remote Sensing Symposium (IGARSS), 2015 IEEE International*, 2015, pp. 4602-4605.
- [75] B. Rodríguez-Cuenca, M. C. Alonso, S. García-Cortés, and C. Ordóñez, "Extracción de señalización horizontal en entornos urbanos a partir de nubes de puntos tridimensionales," presented at the XVI Congreso de la Asociación Española de Teledetección, Sevilla, Spain, 2015.
- [76] B. Rodríguez-Cuenca, S. García-Cortés, C. Ordóñez, and M. C. Alonso, "An approach to detect and delineate street curbs from MLS 3D point cloud data," *Automation in Construction*, vol. 51, pp. 103-112, 2015.
- [77] B. Rodríguez-Cuenca, M. Concepción Alonso-Rodríguez, S. García-Cortés, and C. Ordóñez, "Street curb recognition in 3d point cloud data using morphological operations," in *EGU General Assembly Conference Abstracts*, 2015, p. 813.
- [78] R. Argüelles-Fraga, C. Ordóñez, S. García-Cortés, and J. Roca-Pardiñas, "Measurement planning for circular cross-section tunnels using terrestrial laser scanning," *Automation in Construction*, vol. 31, pp. 1-9, 2013.
- [79] C. Cabo, C. Ordóñez, S. García-Cortés, and J. Martínez, "An algorithm for automatic detection of pole-like street furniture objects from Mobile Laser Scanner point clouds," *ISPRS Journal of Photogrammetry and Remote Sensing*, vol. 87, pp. 47-56, 2014.
- [80] B. Rodríguez-Cuenca and J. A. Malpica, "Clasificadores lineal y cuadrático con utilización del contexto espacial," presented at the XIV Congreso AET, Mieres, Asturias, 2011.
- [81] B. Rodríguez-Cuenca and M. C. Alonso, "Semi-automatic detection of swimming pools from aerial high-resolution images and LiDAR data," *Remote Sensing*, vol. 6, pp. 2628-2646, 2014.
- [82] A. M. de Agirre and J. A. Malpica, "Detecting shadows in a segmented Land Use Land Cover image with LIDAR data," in *IEEE International Geoscience and Remote Sensing Symposium (IGARSS)*, 2012, pp. 5458-5461.
- [83] B. Rodríguez-Cuenca, J. Malpica, and M. C. Alonso, "A spatial contextual postclassification method for preserving linear objects in multispectral imagery," *Geoscience and Remote Sensing, IEEE Transactions on*, vol. 51, pp. 174-183, 2013.

- [84] C. Mallet and F. Bretar, "Full-waveform topographic lidar: State-of-the-art," *ISPRS Journal of Photogrammetry and Remote Sensing*, vol. 64, pp. 1-16, 2009.
- [85] M. Słota, "Full-waveform data for building roof step edge localization," *ISPRS Journal of Photogrammetry and Remote Sensing*, vol. 106, pp. 129-144, 2015.

Acknowledgments

This work has been possible thanks to:

The economic support provided by the following projects:

- Detección de cambios cartográficos a partir de información georreferenciada bitemporal. Entidad Financiadora: Ministerio de Ciencia e Innovación, 01/10/2010 a 30/09/2013. Referencia del proyecto: CGL2010-15357
- Estudio de metodologías operativas de detección automática de cambios basada en la definición de objetos y determinación del suelo sellado. Entidad financiadora: Centro Nacional de Información Geográfica, 30/7/2012 a 31/12/2012. Referencia del proyecto: 2012/00274/001.
- Detección de anomalías y blancos en imágenes hiperespectrales (DABIH). Entidad financiadora: Ministerio de Defensa, 22/12/2011 a 30/11/2013. Referencia del proyecto: 2011/00274/001.
- Análisis de detección automática de cambios en bases de datos de ocupación del suelo. Entidad financiadora: Instituto Geográfico Nacional, 20/09/2010 a 19/09/2011. Referencia del proyecto: 2010/00242/001.

The research programs funded by the following institutions:

- Universidad de Alcalá, Ayudas de iniciación en la actividad investigadora
- Ministerio de Ciencia e Innovación, Programa de Ayudas predoctorales para la Formación del Personal Investigador (programa FPI)

And the datasets provided by the following data providers:

- Instituto Geográfico Nacional and Centro Nacional de Información Geográfica, for providing aerial ortophotos and Aerial Laser Scanner (LIDAR) data
- Topcon Inc., Riegl
- University of Vigo

Personal acknowledgments

The best is yet to come.

Frank Sinatra

Cuando uno se mete en un charco tan grande como el que realizar una tesis doctoral supone, la línea de meta se ve tan lejana que parece que nunca va a llegar. No se sabe ni por dónde empezar a escribir ni qué forma darle a esta criatura. Pero de repente, un día, llegan las prisas para completar el depósito y poner el punto y final a esta enriquecedora y productiva etapa. Y llega el momento de agradecer y recordar a todas aquellas personas e instituciones que en estos 4 años, de una u otra forma, han hecho que este pequeño barco llegue a su puerto.

En lo que al ámbito universitario se refiere, creo que es obligado comenzar agradeciendo a mis directores y codirectores su tutela, su ayuda y sus consejos en la realización de este trabajo. Sin hacer discriminaciones ni menosprecios, es inevitable recordar y agradecer en primer lugar al que es el padre y motor de este trabajo, José Antonio Malpica. Sin tu apoyo, fe, tesón, conocimientos y ejemplo, todo esto habría sido una mera utopía. Fuiste tú quien me dio la oportunidad de introducirme en el apasionante mundo de la investigación y me enseñaste que el éxito sólo tiene una fórmula muy sencilla y fácil de recordar: trabajo, trabajo y trabajo. Aún hoy, tres años después, se echan de menos tus pasos por el pasillo y tus inagotables ganas de trabajar.

Gracias a Conchita por haber tomado las riendas del grupo de investigación y haber sacado fuerzas de flaqueza para tirar para adelante en los momentos más

difíciles. También por tu claridad y por los conocimientos que me has transmitido, tanto en el aspecto docente como en el investigador. Trabajar contigo ha resultado muy enriquecedor, tanto en el aspecto estadístico como en el personal.

Gracias a Silverio y a Tino, por vuestra predisposición, vuestras ganas de trabajar, las innumerables revisiones y por haber creído que todo este trabajo tendría un final feliz. Gracias a la Universidad de Alcalá y a su personal, que ha permitido que esta experiencia saliera adelante.

Gracias a Emmanuel Baltsavias, a Hayko Riemenschneider, a Luc van Gool y al ETH de Zurich por permitirme trabajar en sus grupos de investigación, una experiencia muy enriquecedora y fructífera, tanto en lo profesional como en lo personal.

Por supuesto, gracias a los miembros del grupo de ecogeofísicos, por la buena sintonía entre grupos tan heterogéneos y por los ratos de dispersión en forma de comidas, cafés o cañas, igual de necesarios que las horas ante libros y ordenadores. En especial, gracias a Judith, por tus revisiones, tus traducciones, tus dotes para las artes gráficas y tu capacidad multitarea que nunca deja de sorprender. Y gracias a Antonio por tu paciencia, tus consejos y tu manera de ver la vida.

También quiero recordar y rendir un pequeño homenaje a todas aquellas personas fuera del ámbito universitario que, quizá sin saberlo, han puesto su granito de arena en este trabajo.

Gracias a mis padres, Jorge y Cris, por su incansable fe en mí, por celebrar mis éxitos más que si fueran sus propias victorias y por ayudarme a levantarme a cada tropiezo. También por tener claro que una buena educación es el mejor legado que se puede transmitir a un hijo y por inculcarme la cultura del esfuerzo como única forma de alcanzar el éxito. Gracias a mi familia, en especial a mis abuelos, por seguir dando guerra, a mi tío Miguel, por compartir el sufrimiento rojiblanco aún con cientos de kilómetros de distancia, y a mi tía Isa, por seguir con nosotros después del susto que la vida nos dio.

Gracias a Sara, compañera de aventuras y viaje, por tu infinita paciencia, tus constantes ánimos, tu contagiosa sonrisa y por aguantarme todo este tiempo, tanto en las alegrías como cuando pintaron bastos. Espero que nos queden muchas fronteras que atravesar y muchas puestas de sol que fotografiar.

I also would like to thank Erwin for treated me like a son when I was in Switzerland and for being the perfect tourist host, showing me the incredible sightseeing and amazing secrets that your country hides.

Gracias a mis amigos *de toda la vida*, los Nacho, Diego, Chus, Jairo, Jorge, David, Antonio o Javi, que aunque aún os preguntéis a qué me dedico exactamente, habéis ayudado a aportar la dosis de realidad necesaria para mantener la cordura necesaria para acabar la tesis. A mis compañeros de piso de Ribera 4, Antonio, Cris y Héctor, que habéis logrado ser como mi pequeña familia en Alcalá. Gracias a Agustín, por tu capacidad para liarne con cualquier historia que tenga relación con lo geoespacial y por aportar estresantes aunque necesarias porciones de caos en mi tranquilidad.

Gracias a los conjuntos y asociaciones que me permiten continuar disfrutando de la música. Al conjunto teDeum, por ser una válvula de escape a la rutina de las pantallas y ordenadores. En especial a Antonio, por tu capacidad de gestión y de transmitirnos tu amor por la música y por las cosas bien hechas. Gracias a todos y cada uno de los componentes de la Banda de Gaites Villa de Xixón, por todos los buenos momentos que pasamos en escenarios y pasacalles a uno y otro lado del Atlántico. Gracias Jose Luis, por haberme dado la oportunidad de formar parte de esta gran familia y por ser un ejemplo de lucha en defensa de la verdad y la justicia.

De nuevo, gracias a todos los que habéis hecho que este camino fuera más sencillo de recorrer, y pido disculpas a los que, con las prisas, haya olvidado mencionar. Y esto no es un punto y final, sino un punto y aparte. Seguiré buscando nuevos retos y metas, pero con vuestra compañía, todo será mucho más fácil. Porque lo mejor, siempre está por llegar.

Curriculum

*Y es que es tan alucinante
que hace días que no duermo
por si acaso al despertarme
veo que todo ha sido un sueño.*

Platero y tú

Articles in refereed publications

In Scientific Journals:

- 1 – **Rodríguez-Cuenca, B.**, García-Cortés, S., Ordóñez, C., and Alonso, M.C. (2015). Automatic detection and classification of pole-like objects in urban point cloud data using an anomaly detection algorithm. *Remote Sensing*, 7(10), 12680-12703; doi: 10.3390/rs71012680
- 2 – **Rodríguez-Cuenca, B.**, García-Cortés, S., Ordóñez, C., and Alonso, M. C. (2015). *An approach to detect and delineate street curbs from MLS 3D point cloud data.* Automation in Construction, vol. 51, pp. 103-112, doi: 10.1016/j.autcon.2014.12.009
- 3 – **Rodríguez-Cuenca, B.**, and Alonso, M. C. (2014). *Semi-automatic detection of swimming pools from aerial high-resolution images and LIDAR data.* Remote Sensing, 6(4), pp. 2628-2646, doi:10.3390/rs6042628

- 4 – **Rodríguez-Cuenca, B.**, Malpica, J. A., and Alonso, M. C. (2013). *A spatial contextual postclassification method for preserving linear objects in multispectral imagery*. IEEE Transactions on Geoscience and Remote Sensing, 51(1), pp. 174-183, doi: 10.1109/TGRS.2012.2197756

In Conference Proceedings:

- 1 – **Rodríguez-Cuenca, B.**, Alonso, María C., García-Cortés, S. and Ordóñez, C. (2015). *Extracción de señalización horizontal en entornos urbanos a partir de nubes de puntos tridimensionales*, Libro de actas del XVI Congreso de la Asociación Española de Teledetección, ISBN: 978-84-608-1726-0, pp. 411-414
- 2 – Tamés-Noriega, A., **Rodríguez-Cuenca, B.** and Alonso, M.C. (2015). *Lógica difusa en la extracción de coberturas del terreno*, Libro de actas del XVI Congreso de la Asociación Española de Teledetección, ISBN: 978-84-608-1726-0, pp.435-438
- 3 – **Rodríguez-Cuenca, B.**, Alonso, María C., García-Cortés, S. and Ordóñez, C. (2015). *A study of the roughness and curvature in 3D point clouds to extract vertical and horizontal surfaces*, Geoscience and Remote Sensing Symposium (IGARSS), 2015 IEEE International, DOI: 10.1109/IGARSS.2015.7326853
- 4 – Tamés-Noriega, A., **Rodríguez-Cuenca, B.** and Alonso, M.C. (2015). *Automatic extraction of buildings and trees using fuzzy K-means classification on high-resolution satellite imagery and LIDAR data*, Geoscience and Remote Sensing Symposium (IGARSS), 2015 IEEE International, DOI: 10.1109/IGARSS.2015.7325833
- 5 – **Rodríguez-Cuenca, B.**, Alonso, M.C. and Tamés-Noriega, A. (2015). *LULC database updating from VHR images and LIDAR data using evidence theory*, Proceedings of the conference IFSA EUSFLAT 2015, pp. 987-993. ISSN 1951-6851
- 6 – **Rodríguez-Cuenca, B.**, Alonso-Rodríguez, M. C., Domenech-Tofiño, E., Valcárcel-Sanz, N., Delgado-Hernández, J., Peces-Morera, J., and Arozarena-Villar, A. (2014). *Procedure to detect impervious surfaces using satellite images and light detection and ranging (LIDAR) data*. In SPIE Remote Sensing, International Society for Optics and Photonics, vol. 9244, doi: 10.1117/12.2067259
- 7 – Alonso M.C., Carda P., Gomez Pardo J.C., González Matesanz, F.J., Martínez de Agirre A., Mena Berrios J., **Rodríguez-Cuenca B.**, Sánchez Oliveros C., Simón E. and del Val A. (2013). *Detección de anomalías y blancos en imágenes hiperespectrales*, pp. 523 – 531, ISBN: 978-84-7402-399-2

- 8 – **Rodríguez-Cuenca, B.**, Martínez de Agirre, A., Alonso, M.C. and del Val, A. (2013). *Road extraction method at the pixel and object level using high resolution images and LIDAR data with evidence theory*, in Proceedings of ESA Living Planet Symposium, ISSN 2072-4292
- 9 – Martínez de Agirre A., **Rodríguez-Cuenca B.**, Alonso M.C. and del Val A. (2013). *Method for object-based anomaly detection in hyperspectral images*, in Proceedings of ESA Living Planet Symposium, ISSN 2072-4292
- 10 – **Rodríguez-Cuenca, B.**, Malpica, J. A., and Alonso, M. C. (2012). *Region-growing segmentation of multispectral high-resolution space images with open software*. In IEEE International Geoscience and Remote Sensing Symposium (IGARSS), pp. 4311-4314, doi: 10.1109/IGARSS.2012.6351714
- 11 – **Rodríguez-Cuenca, B.** and Malpica, J.A. (2011). *Clasificadores lineal y cuadrático con utilización del contexto espacial*, XIV Congreso AET 2011, pp. 553-556, ISSN: AS - 3588
- 12 – Malpica, J. A., Alonso, M.C. and **Rodríguez-Cuenca, B.** (2011). *Some techniques for anomaly detection in hyperspectral imageries*, ISBN 1-57083-095-9

Book chapters:

- 1 – Domenech, E., Mallet, C., Arozarena, A., Ruiz, L.A., Hermosilla, T., Recio, J., Gil, J.L, Malpica, J.A., Alonso, M.C., Martínez de Agirre, A. and **Rodríguez-Cuenca, B.** (2014). *Change detection in high-resolution land use/land cover geodatabases (at object level)*. Official Publication European Spatial Data Research, N°64, pp. 10-63

Non-refereed articles

- 1 – **Rodríguez-Cuenca, B.**, Alonso, M.C., García-Cortés, S. and Ordóñez, C. (2015). *Reconocimiento de patrones en nubes de puntos*, V jornadas de Jóvenes Investigadores de la Universidad de Alcalá, Alcalá de Henares, Spain, ISBN:
- 2 – **Rodríguez-Cuenca, B.** (2012). *Detección de coberturas del suelo a partir de imágenes aéreas de alta resolución*, IV Jornadas de Jóvenes Investigadores de la Universidad de Alcalá, Alcalá de Henares, ISBN: 978-84-15834-15-1
- 3 – **Rodríguez-Cuenca, B.** and Malpica Velasco, J.A. (2012). *Detección de piscinas en imágenes de alta resolución*, X Congreso Topcart, Madrid, Spain.

- 4 – Martínez de Agirre, A., **Rodríguez-Cuenca, B.** and Malpica, J. A. (2012). *Accuracy of a DTM obtained from LIDAR data*. VII Asamblea Hispano Portuguesa de Geodesia y Geofísica, San Sebastián, País Vasco, ISBN 978-84-941323-1-5

Contributions to meetings

- 1 – **Rodríguez-Cuenca, B.**, Alonso, María C., García-Cortés, S. and Ordóñez, C. (2015). *Extracción de señalización horizontal en entornos urbanos a partir de nubes de puntos tridimensionales*, XVI Congreso AET 2015, Sevilla, Spain. Talk.
- 2 – Tamés-Noriega, A., **Rodríguez-Cuenca, B.** and Alonso, María C. (2015). *Lógica difusa en la extracción de coberturas del terreno*, XVI Congreso AET 2015, Sevilla, Spain. Poster.
- 3 – **Rodríguez-Cuenca, B.**, García-Cortés, S., Ordóñez, C. and Alonso, M.C. (2015). *A study of the roughness and curvature in 3D point clouds to extract vertical and horizontal surfaces*, IEEE IGARSS Annual Symposium, Milán, Italy. Poster.
- 4 – Tamés-Noriega, A., **Rodríguez-Cuenca, B.** and Alonso, M.C. (2015). *Automatic extraction of buildings and trees using fuzzy K-means classification on high-resolution satellite imagery and LIDAR data*, IEEE IGARSS Annual Symposium, Milán, Italy. Poster.
- 5 – **Rodríguez-Cuenca, B.**, Alonso, M.C. and Tamés-Noriega, A. (2015). *LULC database updating from VHR images and LIDAR data using evidence theory*, IFSA EUSFLAT 2015, Gijón, Asturias, Spain. Talk.
- 6 – **Rodríguez-Cuenca, B.**, Alonso-Rodríguez, M.C., García-Cortés, S. and Ordóñez, C. (2015). *Street curb recognition in 3d point cloud data using morphological operations*. European Geosciences Union (EGU), Vienna, Austria. Talk.
- 7 – **Rodríguez-Cuenca, B.**, Alonso, M.C., García-Cortés, S. and Ordóñez, C. (2014). *Reconocimiento de patrones en nubes de puntos*, V jornadas de Jóvenes Investigadores de la Universidad de Alcalá, Alcalá de Henares, Spain. Talk.
- 8 – **Rodríguez-Cuenca, B.**, Alonso-Rodríguez, M. C., Domenech-Tofiño, E., Valcárcel-Sanz, N., Delgado-Hernández, J., Peces-Morera, J., and Arozarena-Villar, A. (2014). *Procedure to detect impervious surfaces using satellite images and light detection and ranging (LIDAR) data*, SPIE 9244, Image and Signal Processing for Remote Sensing XX, Amsterdam, Netherlands. Talk.
- 9 – Alonso M.C., Carda P., Gómez Pardo J.C., González Matesanz, F.J., Martínez de Agirre A., Mena Berrios J., **Rodríguez-Cuenca B.**, Sánchez Oliveros C., Simón E. and del Val A. (2013). *Detección de anomalías y blancos en imágenes*

- hiperespectrales*, Congreso Nacional de I+D en Seguridad y Defensa, Madrid, Spain. Talk.
- 10 – Martínez de Agirre, A., **Rodríguez-Cuenca, B.**, Alonso, M.C. and del Val, A. (2013). Method for object-based anomaly detection in hyperspectral images, ESA Living Planet Symposium, Edinburgh, Scotland. Poster.
 - 11 – **Rodríguez-Cuenca, B.**, Martínez de Agirre, A., Alonso, M.C. and del Val, A. (2013). *Road extraction method at the pixel and object level using high resolution images and LIDAR data with evidence theory*, ESA Living Planet Symposium, Edinburgh, Scotland. Poster.
 - 12 – **Rodríguez-Cuenca, B.**, (2012). *Detección de coberturas del suelo a partir de imágenes aéreas de alta resolución*, IV jornadas de Jóvenes Investigadores de la Universidad de Alcalá, Alcalá de Henares. Talk.
 - 13 – **Rodríguez-Cuenca, B.** and Malpica Velasco, J.A. (2012). *Detección de piscinas en imágenes de alta resolución*, X Congreso Topcart, Madrid. Talk.
 - 14 – **Rodríguez-Cuenca, B.**, Malpica, J.A. and Alonso, M.C. (2012). *Region-growing segmentation of multispectral high-resolution space images with open software*, IEEE IGARSS Annual Symposium, Munich, Germany. Poster
 - 15 – Martínez de Agirre, A., **Rodríguez-Cuenca, B.** and Malpica, J. A. (2012). *Accuracy of a DTM obtained from LIDAR data*. VII Asamblea Hispano Portuguesa de Geodesia y Geofísica, San Sebastián, País Vasco. Talk.
 - 16 – **Rodríguez-Cuenca, B.** and Malpica, J.A. (2011). *Clasificadores lineal y cuadrático con utilización del contexto espacial*, XIV Congreso AET 2011, Mieres del Camino, Asturias. Poster.
 - 17 – Malpica, J. A., Alonso M.C. and **Rodríguez-Cuenca, B.** (2011). *Some techniques for anomaly detection in hyperspectral imageries*, ASPRS 2011 Annual Conference, Milwaukee, USA. Talk.

Other contributions

Organizing and teaching the course “Detección de Anomalías y Blancos en Imágenes Hiperespectrales”, Instituto Tecnológico de la Marañosa, 25 hours, November 2013.

Organizing and teaching the course “Procesamiento y Análisis de Imagen Satélite y Aérea”, Cursos de Verano Universidad de Alcalá, 25 horas, July 2014.

Talk “Clasificación de imágenes: de la fotografía aérea al mapa”, ciclo de divulgación “Jóvenes Científicos”, XIV Semana de la Ciencia, November 2014, Madrid.

Organization of the conference “V Jornadas de Jóvenes Investigadores de la Universidad de Alcalá”, November 2014.

Short stays

Department of Photogrammetry and Remote Sensing, ETH Zurich, October-November 2013. Supervisor: Professor Emmanuel Baltsavias

Institute for Visual Computing (IVC), Computer Vision and Geometry Lab, ETH Zurich, May-June 2014. Supervisor: Professor Hayko Riemenschneider

Degrees

B.S. degree in Technical Topography Engineer

B.S. degree in Geodesy and Cartography Engineer

M.Sc. in Climate, Energy and Environmental Risk